
Broad resonances in ^{12}C and ^{20}Ne

Kasper Lind Laursen

Department of Physics and Astronomy
Aarhus University, Denmark

**Dissertation for the Degree
of Doctor of Philosophy**

December 2014

Kasper Lind Laursen
Department of Physics and Astronomy
Aarhus University
Ny Munkegade, Bldg. 1520
8000 Århus C
Denmark
E-mail: klj06@phys.au.dk

1st edition, December 2014

This dissertation has been submitted to the Faculty of Science at Aarhus University, Denmark, in partial fulfillment of the requirements for the PhD degree in physics. The work presented has been performed in the period from February 2011 to December 2014 under the supervision of Hans O. U. Fynbo and Karsten Riisager. The experimental work was out carried at local facilities at Aarhus University. The analysis work was performed at the Department of Physics and Astronomy in Aarhus. The IGISOL group at the University of Jyväskylä, Finland, is acknowledged for its hospitality in February/March 2013.

Contents

Table of Contents	iii
Outline	vii
Acknowledgments	ix
List of Publications	xi
Dansk resumé	xiii
Summary in english	xv
I ^{12}C	1
1 Introduction	3
1.1 The birth of nuclear physics	3
1.2 Nuclear models	4
1.2.1 The α -cluster model	5
1.3 ^{12}C structure	7
1.3.1 Cluster description	8
1.3.2 Ab initio approaches	10
1.4 Astrophysics	10
1.5 Experimental studies: search for 2_2^+	15
2 Break-up of ^{12}C	19
2.1 Break-up models	19
2.1.1 Kinematics	21
2.1.2 Angular correlations	24
2.1.3 Dalitz plot	25
2.2 Complete kinematics	28
2.2.1 Decay amplitude	29
3 Motivation	33
3.1 $p + ^{11}\text{B}$ studies	33
3.2 16.11 MeV resonance	35
3.2.1 Our Motivation	35
3.3 γ -delayed α -emission	36

3.3.1	γ -decay	36
3.3.2	Our idea: γ -delayed α -emission	39
4	Experiment	45
4.1	Apparatus	45
4.1.1	Detectors	46
4.1.2	Data acquisition	46
4.1.3	Detection threshold	49
4.1.4	Target foils	50
4.1.5	Calibration source	51
4.2	Geometry definition	51
4.3	Experiment runs	52
4.4	Calibration of the experimental setup	53
4.4.1	Geometry	53
4.4.2	Energy loss calculations	56
4.4.3	Non-ionizing energy losses and the pulse height defect	58
4.4.4	Energy calibration	58
4.4.5	Growth on target foil	63
5	Data reduction and analysis	67
5.1	Basic steps	67
5.1.1	TDC cut	67
5.1.2	Energy calibration	69
5.1.3	Front-back matching	70
5.1.4	Energy loss corrections and center-of-mass transformation	72
5.2	^{12}C analysis	73
5.2.1	multiplicity-three	73
5.2.2	multiplicity-two	76
5.3	Decay channel	77
5.4	Simulation	78
5.4.1	Decay process	78
5.4.2	Experimental effects	79
5.4.3	Analysis of the simulated data	80
6	Results and discussion	81
6.1	Break-up of the 16.11 MeV state	81
6.1.1	Measured energy distributions	81
6.1.2	Acceptances	84
6.1.3	Simulation of break-up models	85
6.1.4	Efficiencies	90

6.1.5	Summary and discussion: 3- α break-up of the 16.11 MeV state	92
6.2	γ -decays	93
6.2.1	Efficiency calculations	94
6.2.2	γ -widths and reduced matrix elements	97
6.2.3	Summary and discussion: γ -decay of the 16.11 MeV state	98
6.3	Conclusion	101
II	^{20}Ne	103
7	Introduction	105
7.1	^{20}Ne structure	105
7.2	Astrophysics: $^{16}\text{O}(\alpha, \gamma)^{20}\text{Ne}$	106
7.3	β -decay	108
7.3.1	Fermi and Gamow-Teller decays	109
7.3.2	Matrix elements and ft values	110
7.3.3	β -delayed particle emission	110
7.4	β -decay of ^{20}Na	111
7.5	Present experiment	111
7.6	Data	112
8	R-matrix theory	115
8.1	Basic theory: Inner and outer region	116
8.2	Application to β -delayed particle emission	117
8.3	Physical parameters	118
8.3.1	Level matrix: Alternative form	119
8.3.2	β -decay matrix elements	119
9	Analysis	121
9.1	Energy calibration	121
9.2	Recoil broadening	121
9.2.1	Recoil correction	123
9.3	Response of the detection system	124
9.3.1	Parametrisation of response function	125
9.3.2	Response fitting	126
9.3.3	Generating response matrix	127
9.4	Fitting procedure	128
10	Results and discussion	131
10.1	Results	131
10.2	Discussion	132

10.2.1 IAS properties	134
10.3 Conclusion	136
A Solving for the collision matrix	137
Bibliography	141
List of Figures	155
List of Tables	163

Outline

The dissertation is divided into two parts. The first part deals with the $p + {}^{11}\text{B}$ experiment performed at the 400 keV Van de Graaff accelerator at Aarhus University from May to September in 2011. The second part describes the analysis of the β -delayed α -particle spectrum acquired during an experiment at the IGISOL facility at the University of Jyväskylä in 2008.

The aim of the $p + {}^{11}\text{B}$ experiment was to study the excitation spectrum of ${}^{12}\text{C}$. One of the questions in nuclear physics that has been, and still is, discussed most, concerns the detailed structure of ${}^{12}\text{C}$ in the excitation region above the threshold for emitting three α -particles. This work aims to shed new light on nuclear properties in this energy region using a new experimental technique that utilizes γ -decays from the state populated in the $p + {}^{11}\text{B}$ reaction. Detecting the α -particles that are emitted in the decay process of the ${}^{12}\text{C}$ resonances provides spectroscopic information.

The ${}^{12}\text{C}$ part is divided into six chapters. Chapter 1 gives a brief introduction to the field of nuclear physics with special attention to models describing ${}^{12}\text{C}$ and its astrophysical importance. Chapter 2 serves as a tool kit describing many of the relevant concepts necessary for studying the $3\text{-}\alpha$ break-up of ${}^{12}\text{C}$. Chapter 3 motivates our study by first reviewing earlier studies of the same reaction used in this thesis and finally describing the idea and potential of our experimental approach. The experiment is described in Chapter 4. The setup is introduced and various calibration issues are discussed. Chapter 5 treats the analysis of the acquired data and briefly explains the procedure used for simulating the break-up data. Finally, Chapter 6 presents the results obtained. The chapter is divided into two overall sections, the first discussing the break-up of the directly populated resonance at 16.11 MeV, while the second part presents γ -decay results.

The experiment at the IGISOL facility was aimed at an accurate determination of the ${}^8\text{B}$ decay spectrum. For calibration purposes the β -decay of ${}^{20}\text{Na}$ was used. The data acquired from the calibration runs on ${}^{20}\text{Na}$ proved interesting in itself. The high level of statistics acquired makes it possible to do a more thorough analysis of the excitation spectrum above the ${}^{16}\text{O} + \alpha$ threshold than done earlier. Our understanding of this spectrum is important both in relation to the nuclear cluster structure of ${}^{20}\text{Ne}$ and the astrophysical [${}^{16}\text{O} + \alpha \rightarrow {}^{20}\text{Ne}$] reaction rate.

The ${}^{20}\text{Ne}$ part is divided into four chapters. Chapter 7 discusses the background for studying ${}^{20}\text{Ne}$ and introduces concepts relevant for analyzing the β -delayed spectrum. The experiment is described very briefly and the data are presented. Chapter

8 reviews the concepts of R -matrix theory and gives the formulas relevant for the analysis. Chapter 9 presents the analysis and finally, Chapter 10 discusses the results obtained.

Acknowledgments

Doing research in natural science has been a dream of mine for almost as long as I can remember. Stories about shining stars captured my imagination of physics and astronomy as a child and moving up to the start of my university years, this dream had not grown smaller. I owe it to my supervisors, Hans Fynbo and Karsten Riisager, for granting me the opportunity to pursue my dream. I thank them for guidance during my PhD years and for their ability to explain problematic concepts, big or small in nature. Current as well as former group members also deserve appreciation: Solveig Hyldegaard, Jacob Johansen, Gunvor Koldste, Morten Lund, Jonas Refsgaard and Michael Munck. A special thanks to Alan Howard for good team work at our experiment setup and for proof reading this dissertation, and to Oliver Kirsebom, for providing exceptional programme packages, especially the simulation code.

Torben Hyltoft and Henrik Bechtold from the IFA workshop deserve a special appreciation due to their help with several construction projects.

I also thank the IGISOL group at the University of Jyväskylä, Finland, for hosting me during my exchange stay at their facility.

The company of my many office partners during last four year has made the long hours in front of the computer a bit more exciting. In this respect I want to thank Oleksandr Marchukov and Arten Volosniev, although I am still a bit disappointed I did not make it to the front cover of Artem's thesis. A profound thanks goes to my good friends Søren Andersen and Tobias Basse, both for sharing offices with me and for putting quite some color into the student life. I also thank Søren for proofreading.

My family has supported me immensely during my studies and deserve my biggest gratitude, especially for helping out with practicalities in the last few months - some would say years! Finally, to two special members of my family, Sofie and Lisbeth, I owe this work to you. Without your incredible support, Lisbeth, this work would not have been possible.

*Kasper Lind Laursen
Aarhus, December 2014*

List of Publications

- I. **K. L. Laursen**, O. S. Kirsebom, H. O. U. Fynbo, A. Jokinen, M. Madurga, K. Riisager, A. Saastamoinen, O. Tengblad and J. Äystö, *High-statistics measurement of β -delayed α spectrum of ^{20}Na* . Eur. Phys. J. A, **49**, 79 (2013).
- II. **K. L. Laursen**, H. O. U. Fynbo, A. M. Howard and O. S. Kirsebom, *Complete kinematics study of the $p + ^{11}\text{B} \rightarrow ^{12}\text{C}$ reaction*. IOP Conference Series, In press.
- III. H. O. U. Fynbo, **K. L. Laursen**, K. Riisager, *Complete kinematics study of the $^{11}\text{B}+p \rightarrow 3\alpha$ reaction*. Journal of Physics: Conference Series **381** (2012) 012116.
- IV. C. Aa. Diget. H. O. U. Fynbo, **K. L. Laursen**, K. O. Madsbol, L. Jørgensen, O. S. Kirsebom and K. Riisager, *Complete kinematics measurement of the $^{11}(p, \gamma)3\alpha$ reaction*. Progress of theoretical Physics. Supplement. **196**, 394-399 (2012).
- V. M. Alcorta, H. O. U. Fynbo, M. Alberts, S. Almaraz-Calderon, P. F. Bertone, P. F. F. Carnelli, M. P. Carpenter, C. J. Chiara, B. DiGiovine, J. P. Greene, C. R. Hoffman, R. V. F. Janssens, T. Lauritsen, **K. L. Laursen**, S. T. Marley, C. Nair, O. Nussair, K. E. Rehm, D. Seweryniak, C. Ugalde and S. Zhu *β -decay measurements of ^{12}B with Gammasphere*. E P J Web of Conferences. **66**, 4.

Dansk resumé

Hvordan er livet opstået? Dette spørgsmål er nok et af de mest interessante af slagsen som vi mennesker kan stille hinanden. Svaret skal findes på både stor og lille skala. Vi starter i det store billede. I minutterne efter Big Bang, processen hvori universet blev skabt, blev ur-suppen af grundstoffer skabt som hovedsageligt består af de to letteste grundstoffer, Hydrogen og Helium. De tungere grundstoffer, grundstoffer som kulstof og ilt som vi ved er essentielle for livet som vi kender det på Jorden, blev ikke skabt pga. det faktum at ingen atomkerner med 5 eller 8 kernepartikler (nukleoner) er stabile. Så hvordan blev livets byggesten skabt? Kulstof bærer løsningen i sig. Under de rette betingelser i stjerners centre kan tre Helium kerner (kaldet alfapartikler) fusionere og danne kulstof isotopen med 12 nukleoner, kulstof-12.

Forståelsen af dette kræver at vi bevæger os ned på lille skala. En bestemt konfiguration af nukleonerne i kulstof skaber en tilstand, kaldet Hoyle tilstanden, som pga. sin energi lige præcis tillader dannelsen af kulstof. Den præcise kernefysiske struktur af Hoyle tilstanden har været genstand for utallige teoretiske og eksperimentelle studier siden 1950'erne, og debatteres stadig.

I vores arbejde forsøger vi at opnå viden om Hoyle tilstanden ved specifikt at lede efter dens excitationer. Vi har udviklet en eksperimentel teknik hvor kulstof-12 skabes i en højt exciteret tilstand, som ved at udsende gamma-stråling populerer tilstande i et energiområde af kulstof-12 som kan bidrage med vigtig information om Hoyle tilstanden. Tilstandene som vi studerer udsender 3 helium kerner når de henfalder, og ved at måle deres retning og energi med halvleder baserede detektorer kan vi studere og udtrække information fra energi spektret i kulstof-12.

Resultaterne fra eksperimentet viser at vores nye teknik virker, og at vi er i stand til at identificere gamma-henfald til det interessante energi område. Vi ser både henfald til kendte og ukendte tilstande, hvor især de sidste kan vise sig at være af stor vigtighed. Derudover bidrager vores studie også med den hidtil mest præcise forståelse af alfahenfaldet af en højt exciteret tilstand i kulstof-12.

At kulstof skabes skyldes altså Hoyle tilstanden og dens egenskaber. Kulstof kan også fusionere med endnu en heliumkerne og danne ilt som så igen kan fusionere og skabe neon. Sandsynligheden for det sidste skridt er dog meget lille fordi der ikke findes en tilstand i neon-20 kernen ækvivalent til Hoyle tilstanden. I et separat eksperiment er energi spektret in neon-20 studeret. Vores undersøgelser resulterer i ny viden om strukturen in neon-20 kernen.

Summary in english

How did life evolve? This question is probably one of the most intriguing questions that we as humans can ask each other. The answer is found both at large and small scales. Starting in the small picture: in the minutes after Big Bang, the process in which the universe was created, the primordial abundance of elements was formed. Mainly hydrogen and helium were created. Heavier nuclei as carbon and oxygen, both of crucial importance for organic life as we know it, were not created due to the fact that no stable nuclei with 5 or 8 nucleons exist. How were the building blocks for life then created? The answer resides in carbon. Three helium nuclei (called alpha-particles) can under the right circumstances fuse into the carbon isotope with 12 nucleons, carbon-12.

The understanding of this is given at small scale. A certain configuration of the nucleons in carbon-12 gives rise to a specific state, called the Hoyle state, which due to its exact energy facilitates the production of carbon. The precise nuclear structure of the Hoyle state has been the subject of numerous studies since the 1950's, but is still highly debated.

We try in our work to gain knowledge about the Hoyle state by searching for its excitations. We have developed an experimental technique in which carbon-12 is formed at a highly excited level, which by emission of gamma-rays populate an energy region that can provide important knowledge about the Hoyle state. The states we investigate decay by emission of three alpha-particles, and by detecting their direction and energy with semi-conductor based detectors, we are able to study and extract information from the energy spectrum of carbon-12.

Our results prove that the new experimental technique works and that we are capable of identifying gamma-decays to the region of interest. Both decays to known and unknown states are observed, where the latter ones can prove particularly important. Furthermore, our study gives the to date most precise understanding of the alpha-decay of the higher lying state in carbon-12.

Carbon can also fuse with a helium core, producing oxygen, which in the next step can form neon. However, this last step is highly improbable since no equivalent state to the Hoyle state is found in the neon-20 nucleus. We have studied the energy spectrum of neon-20 in a separate experiment. Our results give new information about the structure of the neon-20 nucleus.

Part I

^{12}C

Introduction

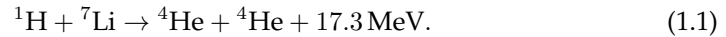
This chapter will introduce the field of nuclear physics through a small historical journey. The most important concepts of nuclear physics, relevant for this thesis, are introduced followed by an introduction to the physical system under scrutiny: ^{12}C .

1.1 The birth of nuclear physics

The search for the fundamental nature of matter had its beginning in time of the greek philosophers. Democritus (460-370 B.C.) speculated that everything is composed of *atoms*, which were thought to be the invisible and indivisible basic constituents of all matter. This idea remained a speculation for more than 2000 years, before investigators in the early nineteenth century applied experimental science to the problem of understanding the basic building blocks of matter. Soon after, the atom was discovered and once the chemists had worked out the rules governing the combination of different kinds of atoms and classified them systematically in the periodic table, the next natural step was to study the fundamental properties of the individual atoms, giving birth to what we call atomic physics. Studies of atomic physics led, in 1896, to the discovery of radioactivity by Becquerel and subsequently new radioactive elements were discovered. These discoveries, together with the discovery of the electron in 1897 by Thomson, indicated that the atom had substructures, suggesting that it is not the indivisible *atom* speculated by Democritus. In fact, Rutherford, who had used the newly discovered radiations to probe atomic sub-structure, proposed the existence of the atomic nucleus in 1911 [Rut11]. Rutherford pictured the atom as having a very small and dense nucleus, consisting of heavy positively charged particles (later named *protons* by Rutherford) with electrons embedded. The electrons were necessary in order to give the atom its neutral character, but with the discovery of the neutron by Chadwick in 1932 it became clear that electrons were not embedded in the nucleus. In stead, a nucleus consisting of A heavy particles, called the *nucleons*, is composed of Z positively charged protons and $A - Z$ neutrons. The field of nuclear physics was born.

Following these events the field of nuclear physics developed explosively. The historical development is due to huge strides in three mutually interacting areas,

namely the experimental apparatus and techniques, the results of the measurements made with them and our theoretical understanding of these results. For an excellent example of the interplay between these areas one can take the invention of the Cockcroft-Walton generator [Coc32a]. Cockcroft and Walton used their newly invented generator to produce the first artificial nuclear disintegrations by bombarding protons at a few hundreds keV onto a lithium target [Coc32b]. They were in fact measuring the reaction



The fact that disintegrations occurred at proton energies lower than the Coulomb barrier, which is around 1 MeV for the ${}^1\text{H} + {}^7\text{Li}$ reaction, confirmed Gamow's theory of barrier penetration, which applied quantum mechanics to the nucleus and showed how the large difference in α -decay half lives can be explained by tunneling through the Coulomb barrier. The pioneering work of Cockcroft and Dalton, which earned them the Nobel prize in 1951, triggered a rapid process in which many nuclear reactions were studied.

1.2 Nuclear models

Today nuclear physics is applied in many different areas, areas that stretch as far and differently as to medicine and weapons. The many different fields, which still are divided into more specific branches, make it difficult to specify one overall goal for the study of nuclear physics. Generally speaking, nuclear research at a fundamental level aims at an understanding of how and why different nucleon configurations give rise to a large diversity in observed properties across the nuclear chart. Answering these questions requires knowledge of how the nucleons move in the nucleus and how they interact with each other. Essentially we need to know the total wave function of the nucleus, but even if this was possible it would be far too complicated to be useful for all but the lightest nuclei. Instead we make use of models, which are characterized in terms of similarities between the nucleus and more simple physical systems that are well understood.

Early on two very different approaches were developed in order to explain observed nuclear properties. Either one can picture the nucleons as moving independently of each other, or one can take the complete opposite stance where the nucleons are considered to be strongly interacting. The first way of describing nuclear structure is formulated in the independent particle model (IPM) where the nucleon-nucleon potential is replaced by one overall potential. We call this a mean-field theory. In the IPM, the fermionic nucleons are filled into energy levels, with specific orbital momentum and spin, according to the *auf-bau* principle as known from atomic physics. The

liquid drop model, first introduced in 1935 by Weizsäcker [Wei35], takes the other approach with strongly interacting nucleons. This model is focussed on the bulk properties of the nucleus, describing correlated motion of nucleons such as rotations and vibrations. The liquid drop model predicts nuclear properties to vary smoothly as a function of the number of nucleons. In the late 1940s, however, it became apparent that this is not the case. Several nuclear properties showed discontinuous behaviour, such as breaks in the two-neutron separation energies in isotopic sequences or in deviations from the semi-empirical mass-formula (based on the liquid drop model). The peculiar thing about these discontinuities were that they appeared at the same values of N and Z . These numbers are known as magic numbers, and were first explained in the shell model [Hax49, May49], an independent particle model including a strong spin-orbit coupling. The explanation of the magic numbers marks one of the most important developments in the theoretical understanding of nuclear structure and boosted the mean field description of nuclei.

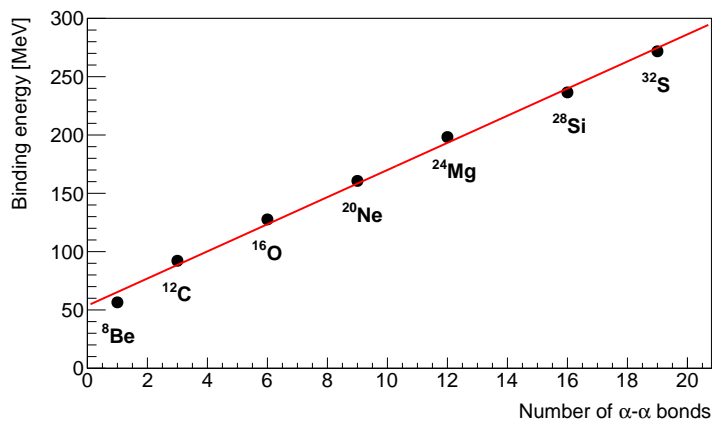


Figure 1.1: Binding energy plotted against the number of α - α bonds in light even-even nuclei. The number of bonds is counted as done by Hafstad and Teller [Haf38].

1.2.1 The α -cluster model

It is remarkable that different properties of nuclei can be described by two models that are so different in type as the collective and the independent particle models. One of the earliest nuclear models, the α -particle model, unifies the single particle and collective aspects of nuclear structure. The idea of α -particles as stable subunits of atomic nuclei was initiated by the discovery of α -decay. The α -particle has one of the highest binding energies per nucleon amongst light nuclei, making it a very robust entity, and in combination with its rather inert nature, due to its high lying first

excited state, it seems justified to consider nuclei as composed of α -particles. The binding energies per nucleon of light even-even nuclei are particularly large, and an examination of these systems by Hafstad and Teller [Haf38] in 1938 showed a linear relationship between the binding energy and the number of α - α bonds. This relationship, shown in Figure 1.1 for even-even nuclei from ${}^8\text{Be}$ up to ${}^{32}\text{S}$, indicated a fixed α - α interaction energy and the presence of α -clustering in the ground states of these nuclei. For most nuclei this picture is an oversimplification since the cluster structure is *washed* out in the compact ground states. One can picture the α clusters as overlapping substantially in the ground states, at which point the fermionic substructure becomes subject to the Pauli-exclusion principle, essentially destroying the bosonic degrees of freedom characterized by separated α -particles. However, ideas about bonds between α -particles in the ground states of light nuclei and geometric cluster arrangements, as pictured in Figure 1.2, survived until the 1960's.

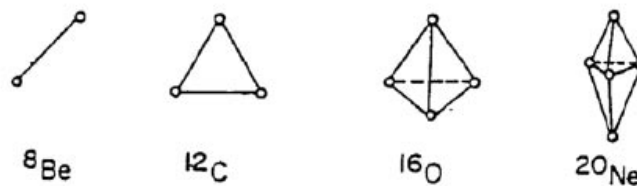


Figure 1.2: Geometric arrangement of light even-even nuclei predicted by D. M. Brink [Bri67]. The number of possible α - α bonds as predicted in [Haf38] is reflected in the arrangements.

Some 30-years after the work of Hafstad and Teller a new idea developed. Ikeda and co-workers proposed a picture in which cluster states emerge as the internal energy of the nucleus is increased [Ike68]. This property of nuclear systems is essentially explained by the fact that it becomes energetically allowed for a nucleus to undergo a structural change into clusters when the energy resembles that of the asymptotically separated clusters. In other words, cluster states *can* evolve when the corresponding cluster threshold is reached. Indeed the ${}^8\text{Be}$ ground state, which is unstable by 91.8 keV with respect to α -particle emission, is found to display significant α -cluster structure. Moving to the ${}^{12}\text{C}$ system, cluster structures are expected near the $\alpha+{}^8\text{Be}$ threshold (7.37 MeV) and in fact a state exist at 7.65 MeV. This state is called the Hoyle state, named after Fred Hoyle who proposed its existence due its astrophysical significance (see Section 1.4), and is believed to have a well developed 3- α structure in accordance with the Ikeda picture.

Obviously the classical and geometric picture of nuclear structure, as shown in Figure 1.2, is inadequate in describing the nucleus as a quantum mechanical system. In the Alpha Cluster Model (ACM), developed by Brink in the 1960's, the nucleus

is described quantum mechanically as a $N\alpha$ system. This model has been applied to many light cluster systems, e.g. by Brink [Bri67] who interpreted the resulting structures as pictured in Figure 1.2. The assumption of preformed α -particles limits the Alpha Cluster Model, preventing it from describing other systems containing different types of clusters and shell-model like states. Microscopic cluster models in which all the nucleons are treated as being active, provides a broader descriptions of nuclear structure. Such models have the capability of describing both cluster- and shell-model-type states, and will be discussed in the next section in the context of the physical system studied in this work: ^{12}C .

1.3 ^{12}C structure

Carbon can in more than one respect be regarded as a "building block" of life. From a chemical perspective compounds made of carbon form the basis of all organic life on Earth. The existence of this crucial atom is attributed to the nuclear properties its most abundant isotope, ^{12}C , playing a crucial role in the formation of heavier elements in the interior of stars. As will be shown in Section 1.4, this importance is attributed to the existence of the Hoyle resonance at 7.65 MeV, a $[J^\pi = 0^+, T = 0]$ resonance that shows a large degree of cluster structure. Also from a nuclear structure point-of-view does ^{12}C attracts attention. The theoretical description of its structure poses an extreme challenge that pushes modern many-body calculation to the limit.

Given the significant importance of the Hoyle state it is a long-sought goal of microscopic models to calculate its energy and structure, but its pronounced cluster structure makes this task difficult. We can gain instructive insight to this problem by considering the shell model scheme as pictured in Figure 1.3. A single nucleon excitation from the closed shell structure results in a new configuration with spin and parity determined by the coupling of the vacancy- and excitation-orbital spin and parities. Exciting a nucleon from the $1p_{3/2}$ orbital to the three lowest unoccupied orbitals gives these couplings:

$$\begin{aligned} (1p_{3/2} \rightarrow 1p_{1/2}) : \quad & 3/2^- \otimes 1/2^- \rightarrow 1^+, 2^+ \\ (1p_{3/2} \rightarrow 1d_{5/2}) : \quad & 3/2^- \otimes 5/2^+ \rightarrow 1^-, 2^-, 3^-, 4^- \end{aligned} \quad (1.2)$$

$$(1p_{3/2} \rightarrow 2s_{1/2}) : \quad 3/2^- \otimes 1/2^+ \rightarrow 1^-, 2^- \quad (1.3)$$

Looking at the level scheme of ^{12}C , shown in Figure 1.4, some states are seen which do not fit with any of the coupling possibilities, one of these being the 0^+ Hoyle state. This example illustrates that the Hoyle state cannot be generated in terms of single

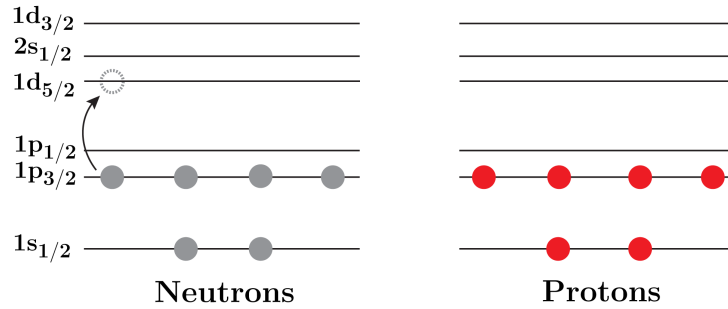


Figure 1.3: Simple shell model picture of ^{12}C . An example is shown where a neutron is excited from the $1p_{3/2}$ orbital to the $1d_{5/2}$ orbital, resulting in a state with spin and parity of 1^- , 2^- , 3^- or 4^- .

nucleon excitations, which is due to the difficulty in describing collective motion in a pure single-particle picture. More advanced shell model calculations also fail in reproducing the Hoyle state [Coh65, Nav00], a fact which has been argued to reflect its $3\text{-}\alpha$ structure. It should though be noted that ^8Be , a highly clustered nucleus, is well described in shell model calculations.

1.3.1 Cluster description

Cluster models successfully reproduce collective states in ^{12}C which shell model calculations fail to describe. Many models that treat ^{12}C as three α -particles are successful in describing the properties of the Hoyle state. The potential model in [Fed96] introduces a method that solves the quantum mechanical three-body Coulomb problem in the continuum, reproducing quite accurately the energy and width of the 0_2^+ Hoyle state. Other successful models like the Generator Coordinate Model (GCM) [Des87], Resonating Group Model (RGM) [Kam81] and the Bose Einstein Condensate (BEC) model [Fun06] are microscopic in character. The word *Microscopic* relates to the fact that these models all treat the α -particles as composed of individual nucleons, and although they are designed to describe α -particles, the total wave function is antisymmetrized, which means that for compact states the wave function respects the internal fermionic degrees of freedom. The fact that the Hoyle state is considerably larger than the ground state [Ogl13] may provide conditions under which the antisymmetrization plays a negligible role. Under such circumstances it may become possible for the system to be described by three bosons, an idea that have inspired the BEC model. This model is particularly interesting since it constitutes a new form

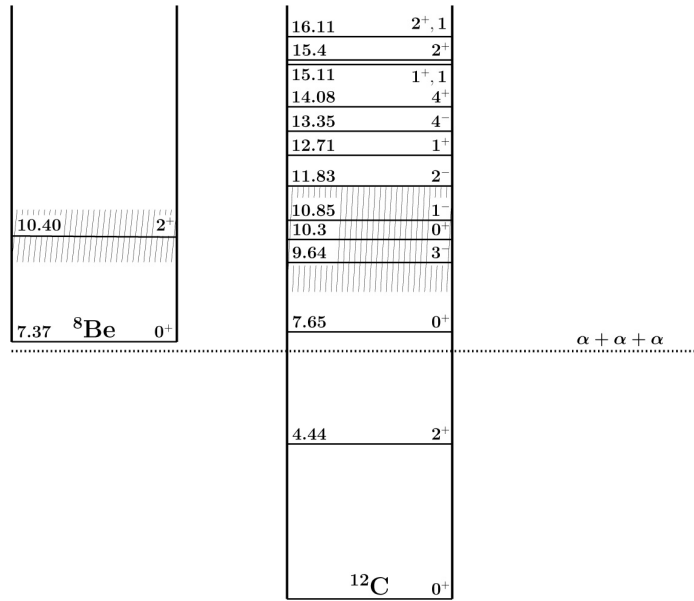


Figure 1.4: Level scheme of ^{12}C including known states up to 16 MeV.

of nuclear matter in which the bosonic constituents all are allowed to occupy the lowest energy orbital. The so-called Anti-symmetrized Molecular Dynamics (AMD) model is capable of combining shell model and cluster structures, essentially because it does not assume the preformation of α -clusters. Calculations with a variant of this model, the Fermionic Molecular Dynamics (FMD) model, have shown a 70% overlap with the BEC wavefunction for the Hoyle state [Che07], indicating to some extent a condensate picture for this state.

A few years after the proposed existence and observation of the Hoyle state, Morinaga conjectured a linear arrangement of α -particles in this state [Mor56]. As an immediate consequence Morinaga proposed that 2^+ and 4^+ states should appear around 9.7 MeV and 14.2 MeV, respectively, as collective excitations upon the deformed Hoyle state. Building a rotational band of excited states upon the Hoyle state, we will expect the energies of these state to follow the spectrum given by the quantum mechanical rotor:

$$E(J) = \frac{\hbar^2 J(J+1)}{2I}, \quad (1.4)$$

where J is the spin and I is the moment of inertia. The location of these states is therefore directly sensitive to the structure of the Hoyle state through its moment of inertia. Models treating the Hoyle state as a linear chain place the 2_2^+ state at ~ 8.4 MeV above the ground state [Mer92], whereas the BEC [Fun03] and FMD [Che07] models

predicts its existence at excitation energies of ~ 9 MeV and ~ 10 MeV respectively. Pin pointing the locating of the 2_2^+ and 4_2^+ states experimentally will therefore provide crucial input to theoretical calculations describing the structure of the Hoyle state.

1.3.2 *Ab initio* approaches

Perhaps the most ambitious type of model are the *ab initio* models, which are build from first principles. In these models nuclei are described as systems of nucleons interacting by fundamental interactions, where the only approximations made are of mathematical character. This approach requires huge computational power and poses an extreme challenge even for the simplest nuclei. The process of solving the problem is considerably worsened by the fact that the details of the fundamental interactions are ill-known. At present the underlying theory of the nuclear force, quantum chromodynamics, cannot be applied in the non-perturbative regime of nuclear physics which means that a quantitative descriptions of the nucleon-nucleon potentials is derived from scattering experiments.

An example of an *ab initio* approach that circumvents this problem is the lattice effective field theory. The method is based on Chiral Effective Field Theory, a framework in which the interactions between the nucleons is described as an expansion in powers of the nucleon momenta and the pion mass. The interaction calculations are carried out on a lattice, discretizing time and space, in order to numerically calculate properties of the system in hand. Recent calculations using this technique reproduce remarkably well the binding energies of the ^{12}C ground state, the Hoyle state and its 2^+ excitation. The structure for the ground state is found to resemble that of a triangle configuration of three α -particles, while for Hoyle state and its 2^+ excitation the structures looks like a bent arm. Future calculations performing calculations on a finer lattice grid will provide deeper insight to the properties ^{12}C states.

1.4 Astrophysics

Astrophysics and nuclear physics combine into an interdisciplinary branch of physics which deals with questions that, both literally and figuratively speaking, are big. Nuclear astrophysics plays a vital role in helping us understand the energy generation of stars and the origin of the elements from which life is build. Although not known at the time, Einstein's famous mass-energy relation gave basis for understanding the energy production in stars. This connection was realized by Eddington in 1920 after Aston in the same year had discovered that the helium atom has a mass that is slightly lower than that of four hydrogen atoms. He immediately argued that the energy pro-

duction of the sun is a result of hydrogen being converted into helium. This was the first step in the process of understanding *nucleosynthesis*, the process that creates new atomic nuclei from pre-existing nuclei.

In the late 1930s Critchfield and Bethe worked out the pp-chain and CNO reaction cycle that power the Sun and other similar main-sequence stars [Bet38, Bet39]. These reaction chains only turn hydrogen into helium, and the question about the formation of heavier elements, which undeniably exist in the universe, naturally arose. The lack of stable isotopes of mass 5 and 8 makes the next nucleosynthetic step more challenging to grasp. Bethe argued that the stellar core temperature is too low for the process of three α -particles fusing into ^{12}C , to become accessible [Bet39]. The understanding of the mechanism involved for creating heavier nuclei than helium had to wait to the post-war years, where the 3- α process was worked out. This process motivates a large part of the present work. Before this process is described in more detail a few concepts relevant for thermonuclear fusion will be introduced.

Reaction rates

Stellar evolution models, including its hydrostatic and explosive burning phases, is needed in order to describe the observed elemental abundances in the solar system. For these models to work accurately, knowledge of several nuclear reaction rates at the astrophysical relevant energies is needed. One immediate problem in this respect is that the reaction cross sections cannot be measured directly since they generally are very small. This is due to the relatively low reactant energy compared to the Coulomb barrier. In fact, the interplay between the thermal energies inside a star and the probability for tunneling through the Coulomb barrier, defines quite sharply the reaction energies relevant for the astrophysical case in question.

The reaction rate between nuclei of type 1 and 2 can be written in terms of the number density of one of them, the flux of the other type and the reaction cross section:

$$r_{12} = N_1 N_2 v \sigma(v), \quad (1.5)$$

where $N_i (i = 1, 2)$ is the number densities, v is the relative velocity between the two colliding nuclei and $\sigma(v)$ is the cross section. For the formula 1.5 to be useful in stellar environments we need to average the relative velocity by the Maxwell-Boltzmann distribution¹,

$$\begin{aligned} r_{12} &= 4\pi \frac{N_1 N_2}{1 + \delta_{1,2}} \left(\frac{\mu}{2\pi k_B T} \right)^{3/2} \int_0^\infty v^3 \sigma(v) e^{-\frac{\mu v^2}{2k_B T}} dv, \\ &= \frac{N_1 N_2}{1 + \delta_{1,2}} \langle \sigma v \rangle, \end{aligned} \quad (1.6)$$

¹Here we use that if the incident velocities are Maxwellian, then the same applies to the relative velocity.

where μ is the reduced mass, $\delta_{1,2}$ is the Kronecker delta and T the temperature. The quantity $\langle \sigma v \rangle$ is the Maxwellian averaged cross section. Normally we parametrize the cross section in terms of the so-called *S-factor* by factoring out the $\frac{1}{E}$ dependence and the strong penetrability factor (Gamow factor)

$$\sigma(E) = S(E) \frac{e^{-2\pi\eta(E)}}{E}, \quad (1.7)$$

where $\eta(E) = \frac{Z_1 Z_2 e^2}{\sqrt{2}\hbar} \left(\frac{\mu}{E}\right)^{1/2}$ is the Sommerfeld parameter. Substituting this expression into the reaction rate Eq. 1.6 we get

$$r_{12} = \left(\frac{8}{\pi\mu}\right)^{1/2} \frac{N_1 N_2}{1 + \delta_{1,2}} (k_B T)^{-3/2} \int_0^\infty S(E) e^{-(2\pi\eta + \frac{E}{k_B T})} dE. \quad (1.8)$$

The *S-factor* contains all intrinsic properties of the nuclear reaction since the $\frac{1}{E}$ and $e^{-2\pi\eta(E)}$ factors describe the known energy dependencies. The *S-factor* is often found to be nearly constant when no resonances appear, and it is usually determined at the astrophysical energy by extrapolation from measured values at higher energies. Eq. 1.8 shows that the reaction rate peaks in an energy region given by the product of penetrability factor $e^{-2\pi\eta(E)}$ and the Maxwell-Boltzmann factor $e^{-\frac{E}{k_B T}}$. This region is called the *Gamow-peak* and the size of the *S-factor* in this region determines how quickly a reaction proceeds. The location of the Gamow peak E_G is

$$E_G = \left(\pi Z_1 Z_2 e^2 k_B T \sqrt{\frac{\mu}{2}}\right)^{2/3}, \quad (1.9)$$

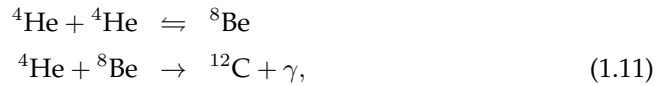
and its width can be approximated as

$$\Delta = 4\sqrt{\frac{E_G k_B T}{3}}. \quad (1.10)$$

Nuclear resonance levels inside the Gamow window can enhance the the reaction rate, resulting in *resonant* reactions, while *non-resonant* reactions occur when only tails of resonances are inside this window.

3- α reaction

In 1951 Öpik recognized [Ö51] that stars in the red giant phase produce the elevated temperatures needed by Bethe [Bet39]. Salpeter showed that the temperature is high enough for a small, but significant equilibrium concentration of the unstable ${}^8\text{Be}$ ($\tau \sim 10^{-16}\text{s}$) to build up. Salpeter proposed the formation of ${}^{12}\text{C}$ to proceed as a two step process



where a γ -decay to a bound state in ^{12}C is the final step. The reaction rate is related to the properties of a single resonance located inside the Gamow window as²

$$\langle\sigma v\rangle \propto \frac{\Gamma_\alpha \Gamma_{\text{rad}}}{\Gamma} e^{E_R/k_B T}, \quad (1.12)$$

where E_R is the resonance energy, Γ and Γ_α are the total and α -particle widths, while Γ_{rad} is the total radiative width consisting of the γ -decay and pair-decay widths.

For each of the two reaction steps the corresponding Gamow window is shown in Figure 1.5 for a temperature of 0.2×10^9 K, which is a typical Red Giant core temperature. The arrows indicate the positions of the resonances through which the reactions dominantly proceeds, namely the ^8Be ground state at 91.8 keV (above the 2α threshold) and the so-called Hoyle state at 287.6 keV (above the 3α threshold). These resonances are located close to the peak of the Gamow window facilitating resonant carbon production. The Hoyle state is the only contributor to the 3α reaction rate at hydrostatic burning conditions in Red Giant stars.

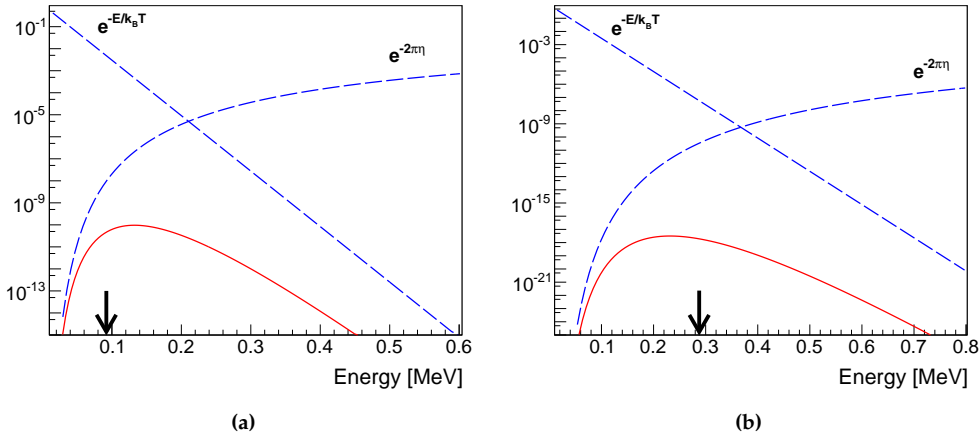


Figure 1.5: Figures showing the Maxwell-Boltzmann factor ($e^{-E/k_B T}$) and the Gamow factor ($e^{-2\pi\eta}$) for a temperature of 0.2 GK in case of the $^4\text{He} + ^4\text{He}$ reaction (a) and the $^4\text{He} + ^8\text{Be}$ reaction (b). Both these factors enter the integrand in Eq. 1.8 and their product, the red solid line, determines the energies at which thermonuclear processes occur. The arrow in (a) indicates the position of the ^8Be ground state while in (b) it indicates the position of the Hoyle state. The ordinate is in arbitrary units.

The Hoyle state is named after F. Hoyle, who predicted its existence in order to account for the absolute abundance of ^{12}C and the relative abundance of ^{12}C and ^{16}O [Hoy53,Hoy54]. Based on reaction rate calculations, Hoyle argued that a $J^\pi = 0^+$

²This proportionality comes about by describing the cross section in 1.5 by a Breit-Wigner distribution.

resonance at an excitation energy of 7.68 MeV was needed. Shortly after his prediction, a group at Caltech found experimental evidence [Dun53] for a state at an energy very close what suggested by Hoyle, and a few years later a new measurement [Coo57] pin-pointed its energy to 7.653 ± 0.008 MeV and assigned 0^+ as its spin and parity.

Figure 1.6 shows the reaction rate from [Fyn05] relative to the NACRE (Nuclear Astrophysics Compilation of Reaction Rates) compilation [Ang99]. The NACRE compilation assumes, at a purely theoretical level, the existence of Morinaga's 2^+ resonance at an excitation energy of 9.12 MeV with an α -decay width of 560 keV and a γ -decay width of 200 meV. The reaction rate from [Fyn05], which is adopted in a more recent compilation of reaction rates [Cyb10], does not assume any 2^+ contribution and includes the interference between the Hoyle state and the broad 0^+ state at 10.3 MeV. See Section 1.5 for a discussion of the experimental evidence for the 2^+ state.

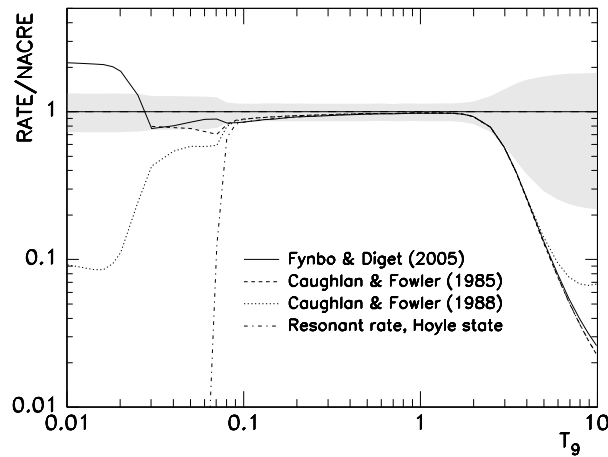


Figure 1.6: $3\text{-}\alpha$ reaction rate from [Fyn05] relative to the NACRE rate (logarithmic ratio on the ordinate). The Fynbo result is also shown when only including the Hoyle state in the rate calculations.

At higher temperatures ($T > 10^9$ K) there is a significant deviation between the rates, which is due to the inclusion of the 2^+ state in [Ang99], whereas they agree well in the temperature range 10^8 K – 10^9 K, in which the reaction rate is fully determined by the properties of the Hoyle state resonance. The uncertainty on the reaction rate in the 10^8 K – 10^9 K regime is mainly given by the uncertainty on the radiative width of the Hoyle state, which currently is $\simeq 12\%$ [Che10]. Experimentally this width can

be accessed by

$$\Gamma_{\text{rad}} = \frac{\Gamma_{\gamma} + \Gamma_{e^+e^-}}{\Gamma} \frac{\Gamma}{\Gamma_{e^+e^-}} \Gamma_{e^+e^-}, \quad (1.13)$$

but performing measurement of $\frac{\Gamma}{\Gamma_{e^+e^-}}$ and $\Gamma_{e^+e^-}$ are extremely challenging due to their small size (at the order of 10^{-6} and 10^{-5} eV).

The $3\text{-}\alpha$ reaction plays an important role for the synthesis of heavier elements at various astrophysical sites. In combination with the $^{12}\text{C}(\alpha, \gamma)^{16}\text{O}$ reaction it controls the produced amounts of carbon and oxygen at the end of hydrostatic helium burning ($T = 10^8 \text{ K} - 10^9 \text{ K}$), having important consequences for late stellar evolution. The iron core mass prior to the collapse that leads to a type II Supernova is for example directly dependent on the C/O ratio [Aus99], and simulations of these supernovae require the $3\text{-}\alpha$ reaction rate to be known within 10%.

The production of heavy elements during explosive nucleosynthesis ($T > 10^9 \text{ K}$) is also sensitive to the $3\text{-}\alpha$ reaction rate. The $3\text{-}\alpha$ reaction rate is for example shown to be important for the production ^{44}Ti in core collapse super novae [The98, Tur10]. γ -lines associated with the decay of ^{44}Ti can be measured by γ -ray telescopes, making it an isotope of high astrophysical significance since these γ -ray measurements provide a sensitive diagnostic of the explosion. As an interesting note, the observed elemental abundances in the solar system has even been used to adjust the $3\text{-}\alpha$ reaction rate [Aus14]. This way of restricting the $3\text{-}\alpha$ reaction rate is in a way a continuation of F. Hoyle's line work, in which constraints on the $3\text{-}\alpha$ reaction rate are inferred from observations.

1.5 Experimental studies: search for 2_2^+

The interest in the Hoyle state due to its importance in astrophysics and in cluster phenomena [Fyn11, Fre12a] has triggered several experimental campaigns searching for a possible 2^+ excitation. As noted above, the observation of such a state and its properties will give insight to the cluster nature of the Hoyle state. Ever since the state was conjectured by Morinaga in 1956 [Mor56] numerous experiments have failed to observe it. The difficulty in identifying the 2_2^+ state, if it exist, stems from the fact that it is difficult to resolve broad 2^+ strength in the expected excitation region around 10 MeV. This energy region of the ^{12}C spectrum, well above the $3\text{-}\alpha$ threshold (see Figure 1.4), is dominated by several broad resonances as e.g. the 0^+ at 10.3 MeV with at width of 3 MeV and the 315 keV wide 1^- states 10.84 MeV [AS90]. Several different experimental probes, each tuned for maximum sensitivity to 2^+ strength, have therefore been used in order to circumvent this problem. The most recent experiments, some of which observe a 2^+ resonance in the 10 MeV region, will be described here.

Inelastic scattering

By scattering 386 MeV α -particles inelastically of a ^{12}C target, Itoh and collaborators first observed evidence for a 2^+ state near 10 MeV in 2004 by using a multipole decomposition analysis technique [Ito04]. By examining the α -spectrum at a forward angle where the $L = 2$ component is favored over the $L = 0$ component in the differential cross section, corresponding to the excitation of 2^+ and 0^+ states, respectively, they found evidence for a 2^+ state. Their results were, however, complicated by the presence of the 3^- state at 9.64 MeV. In [Ito11] a new analysis of the $^{12}\text{C}(\alpha, \alpha')$ data was performed by the same group explaining the $L = 2$ strength as a 2^+ state at 9.84(6) MeV and 1.01(15) MeV broad. This state is a prime candidate for the 2^+ excitation of the Hoyle state [Fyn11].

In a similar inelastic scattering experiment, using 66 MeV and 200 MeV protons, evidence for a 2^+ state at 9.61(1) MeV with a width of 0.6(1) MeV was found [Fre09]. The observation of the 2^+ state was complicated by the 3^- state and the broad 0^+ and 1^- states, but performing an R -matrix line shape analysis the 2^+ strength was found submerged beneath these states. An experiment using $^{12}\text{C}(p, p')$ at $E_p = 25$ MeV [Zim11] reported result consistent with [Fre09]. A re-examination of the α [Ito04, Ito11] and proton [Fre09] scattering data resulted in consistent results placing the 2^+ state at 9.75(15) MeV with a width of 0.75(15) MeV [Fre12b].

$^{10/11}\text{B}(^3\text{He}, p/d)^{12}\text{C}$

The $^{11}\text{B}(^3\text{He}, d)^{12}\text{C}$ reaction was used in 1971 to investigate the ^{12}C excitation spectrum [Rey71]. The observation of a resonance at 11.16 MeV, displaying 2^+ nature, was reported and this resonance was for many years the only candidate for the first excited state of the Hoyle state. Its position is, however, well above the energy expected from cluster calculations. Inspired by the results from the inelastic scattering experiments the $^{11}\text{B}(^3\text{He}, d)^{12}\text{C}$ experiment was recently repeated using a high-resolution magnetic spectrometer [Smi12]. Their results excluded the existence of the 11.16 MeV state and were consistent with a 2^+ state at 9.7 MeV. The same reaction and the $^{10}\text{B}(^3\text{He}, d)^{12}\text{C}$ reaction has been used with a detection setup consisting of double sided silicon detectors [Alc12]. This setup facilitates the determination of the ^{12}C excitation energy both from the proton/deuteron and the complete kinematical detection (see Section 2.2) of the α -particles emitted in the ^{12}C break-up. No evidence for new 2^+ states were found in this experiment.

β -decay

Probing ^{12}C resonances using the β -decay of ^{12}N and ^{12}B introduces quantum mechanical selectivity. Allowed Gamow-Teller transitions from the [$J^\pi = 1^+, T = 1$]

ground states of ^{12}N and ^{12}B can populate ^{12}C resonances with 0^+ , 1^+ and 2^+ and $T = 0$. In relation to the 2_2^+ search these selection rules have the immediate advantage that transitions to the problematic 3^- level are suppressed.

The combined analysis of two experiments detecting the β -delayed α -particles from ^{12}B [Dig05] and ^{12}N decay [Fyn02] in complete kinematics illustrated the importance of interference in the ^{12}C spectrum [Dig05, Fyn05]. The structure of the excitation spectrum at 10 MeV could be described in an R -matrix model due to the interference between the Hoyle state ghost³ and the broad 0^+ state at 10.0 MeV. In fact their measurements did not find evidence for a 2^+ state near 10 MeV and located the 0^+ above 11 MeV. New experiments on the decay of ^{12}N and ^{12}B provided improved statistics and reported $E_{2_2^+} = 11.1(3)$ MeV and $\Gamma_{2_2^+} = 1.4(4)$ MeV [Hyl10b]. These findings deviate significantly from the inelastic scattering results and illustrate the complex problem of understanding the ^{12}C spectrum. The deviating results open up the question as to whether the observed 2^+ states are the same.

γ -excitation/decay

Using electromagnetic transitions in ^{12}C can, in a way similar to β -decays, introduce selectivity. Recently, a group working with a high intensity γ -ray source (at the HI γ S facility at Triangle Universities Nuclear Laboratory), conducted an experiment where ^{12}C was photodisintegrated. Measuring the produced α -particles using an optical time projection chamber, allowing complete angular distributions, they identified the 2_2^+ state at 10.03(11) MeV, with a total width of 0.80(13) MeV [Zim13b]. These values have subsequently been adjusted to $E_{2_2^+} = 10.13_{-0.05}^{+0.06}$ MeV and $\Gamma = 2.08_{-0.26}^{+0.33}$ MeV [Zim13a]. The major advantage of this approach comes from the electromagnetic transition rules preventing 0^+ population since the $[0^+(\text{ground state}) \rightarrow 0^+]$ transition is prohibited.

The selectivity can even be turned tunable by exploiting γ -decays to the region of interest in ^{12}C . By populating a higher lying resonance with well-chosen spin-parity one can achieve the desired selectivity. One drawback of this approach is the relatively small γ -branching ratios. The γ -delayed α -break-up of the $[J^\pi = 1^+, T = 0]$ and $[J^\pi = 1^+, T = 1]$ states at 12.71 MeV and 15.11 MeV, respectively, has been observed in a proof-of-principle study [Kir09].

The γ -decay approach is utilized in this work where the $[J^\pi = 2^+, T = 1]$ state at 16.11 MeV is populated with the aim of observing decays to the region around 10 MeV. Through this method new information on the highly debated 2_2^+ may be extracted providing a better structural understanding of the Hoyle state.

³A *ghost* is a structure arising from a single resonance level located close to a threshold [Bar62].

Break-up of ^{12}C

Resonances in ^{12}C , located above the $3\text{-}\alpha$ threshold, can decay by emission of α -particles and this decay mode is for most of them the dominating one. In the experiment presented in this work we obtain spectroscopic information on ^{12}C by detecting these α -particles. This chapter introduces some of the concepts relevant for the description and measurement of the $3\text{-}\alpha$ break-up. This includes the kinematics involved in the decay process and more detailed aspects such as angular correlations.

2.1 Break-up models

A decay scheme for ^{12}C is shown in Figure 2.1 where the decay process is pictured as proceeding through the unbound ^8Be nucleus. This way of picturing the break-up falls into one of two extreme models, namely the sequential model [Bal74]. The democratic model [Kor90] is its counterpart. In the sequential model the break-up proceeds as two dynamically independent two body break-ups, with the unstable ^8Be as the intermediate step. The dynamical independence, meaning that the intermediate two-body resonance does not feel the Coulomb repulsion from the first α -particle when breaking up, requires the intermediate resonance to be long-lived. The only correlations that can arise between the two decays will be those due to conservation of angular momentum and parity.

In the democratic model the break-up is instead assumed to go directly into the 3-particle final state. In this model no long-lived intermediate states are involved in the break-up and the $\alpha\text{-}\alpha$ interaction is assumed to play an insignificant role in the breakup. The decay amplitude is calculated by expanding in hyperspherical harmonics functions retaining only the lowest-order term permitted by symmetries. The hyperspherical harmonics are eigenfunctions of the grand angular momentum operator of the three-body system, characterized by the hypermomentum K . Since we are dealing with three identical spin-zero particles both models must symmetrize the final state amplitude according to Bose symmetry.

For low lying ^{12}C resonances the only decay routes possible are those proceeding through the narrow ^8Be ground state ($\Gamma = 5.6\text{ eV}$) or the broad first excited state ($\Gamma = 1.5\text{ MeV}$). One expects decays via the ground state to be well described by the

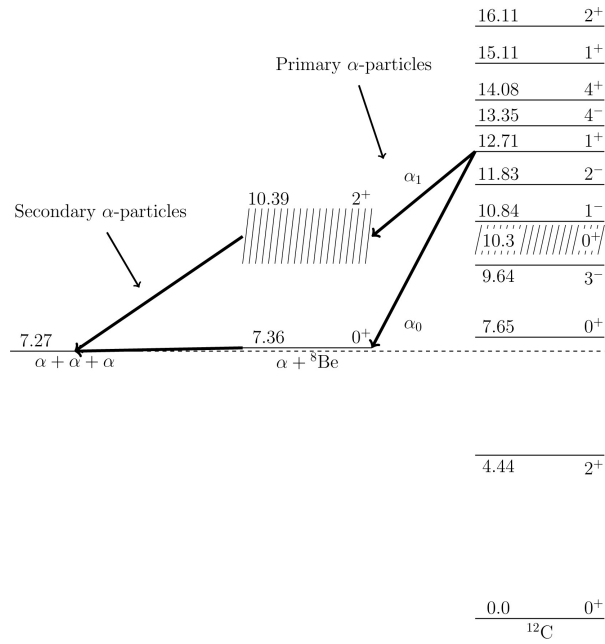


Figure 2.1: Schematic diagram of the ^{12}C decay scheme.

sequential model whereas the assumption of dynamical independence is less clear for the much shorter lived first excited state.

As an example we will look at the decay of the Hoyle state. Since this state can only decay via ${}^8\text{Be}(\text{gs})$ it is expected to decay sequentially, and this assumption goes into the calculation of the thermo-nuclear 3α reaction rate. Some controversy exist as to whether this is consistent with observations, but most experimental data indicate a sequential decay mode. Upper limits on the direct decay branch has been established in recent years. Using the ${}^{11}\text{B}({}^3\text{He}, d\alpha\alpha\alpha)$ reaction a limit of 5×10^{-3} (at a 95% confidence level) was established [Kir12] and more recently a limit of 0.2% (at a 95% confidence level) was deduced from an experiment using the ${}^{12}\text{C}({}^{12}\text{C}, 3\alpha){}^{12}\text{C}$ reaction [Ito14], which conflicts with a claimed measurement of a non-sequential branch of $(9.1 \pm 1.4) \times 10^{-3}$ [Ran13]. For a different example we take the 1^+ state at 12.71 MeV to which γ -decays are observed in this study. This state can only decay via the first excited state in ${}^8\text{Be}$ due to parity conservation. Dynamical independence seems a bad assumption in this case since the typical distance travelled by the first emitted α -particle in the time $\frac{\hbar}{E}$ is around 5 fm. This implies a clearly non-negligible Coulomb energy of 1 MeV between the first emitted α -particle and the ${}^8\text{Be}$ recoil at the time of the second break-up. The break-up of the 1^+ state is nevertheless shown to be best described with a sequential model but dynamical correlations are also seen [Fyn03].

2.1.1 Kinematics

It is worthwhile to discuss the kinematics involved in the ^{12}C break-up. This will help us interpret the measured energy spectra later on.

Staying in the sequential picture, we define Q_1 as the energy available in the first break-up step, i.e. $Q_1 = E_{^{12}\text{C}}^{\text{exc.}} - E_{^8\text{Be}}$, where $E_{^{12}\text{C}}^{\text{exc.}}$ is the excitation energy of the decaying resonance and $E_{^8\text{Be}}$ is the energy of the intermediate ^8Be level relative to the ^{12}C ground state. Q_2 is the energy available in the second step and is given as $Q_2 = E_{^8\text{Be}} - E_{3\alpha}$, where $E_{3\alpha}$ is the energy of three α -particles relative to the ^{12}C ground state. The total available energy Q is then given as $Q_1 + Q_2$. The α -particle that is emitted first is called a *primary* α -particle while those from ^8Be are called *secondary*. Their energies in the ^{12}C reference frame, when doing a non-relativistic calculation, are given as

$$E_1 = \frac{2}{3}Q_1 \quad (2.1)$$

$$E_2 = \frac{1}{6}Q_1 + \frac{1}{2}Q_2 + \cos\theta' \sqrt{\frac{Q_1 Q_2}{3}} \quad (2.2)$$

$$E_3 = \frac{1}{6}Q_1 + \frac{1}{2}Q_2 - \cos\theta' \sqrt{\frac{Q_1 Q_2}{3}}. \quad (2.3)$$

In Figure 2.2 the numbering of the energies are explained together with the angle θ' which gives the angle of emission of a secondary α -particle relative to the opposite direction of the primary α -particle as measured in the ^8Be frame. The angle between the two secondary α -particles in the ^{12}C frame ($\theta_{2,3}$ - also defined in Figure 2.2) is given as

$$\cos\theta_{2,3} = \frac{Q_1/3 - Q_2}{\sqrt{(Q_1/3 + Q_2)^2 - \frac{4}{3}Q_1 Q_2 \cos\theta'}}. \quad (2.4)$$

Primary α -particles populating the narrow ground state in ^8Be , labelled α_0 , will be sharply distributed in energy, whereas those that proceed through the 2^+ first excited state ($\Gamma = 1.5$ MeV), labelled α_1 , are broadly distributed at lower energies. The secondary α -particles will inherently be broadly distributed owing to the recoil motion of the ^8Be nucleus with those originating from $^8\text{Be}(2^+)$ additionally broadened.

For a discussion of detection acceptances it is convenient to have the energies in Eq. 2.3 and $\theta_{2,3}$ evaluated in the laboratory frame, which for reactions is different from the ^{12}C rest frame. For the following discussion this is done by doing a Galilean transformation of the particle velocities, assuming ^{12}C is populated at an excitation energy of 16.11 MeV in the $p + ^{11}\text{B}$ reaction ($E_p = 162$ keV):

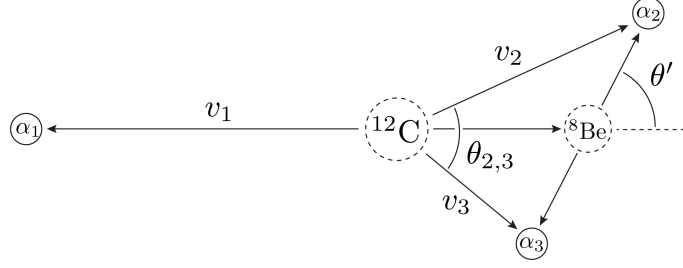


Figure 2.2: The 3- α break-up. θ' is the angle between the secondary α -particle and the first emitted α -particle as seen from the ^8Be frame. $\theta_{2,3}$ is the angle between the secondary emitted α -particles seen from the ^{12}C frame.

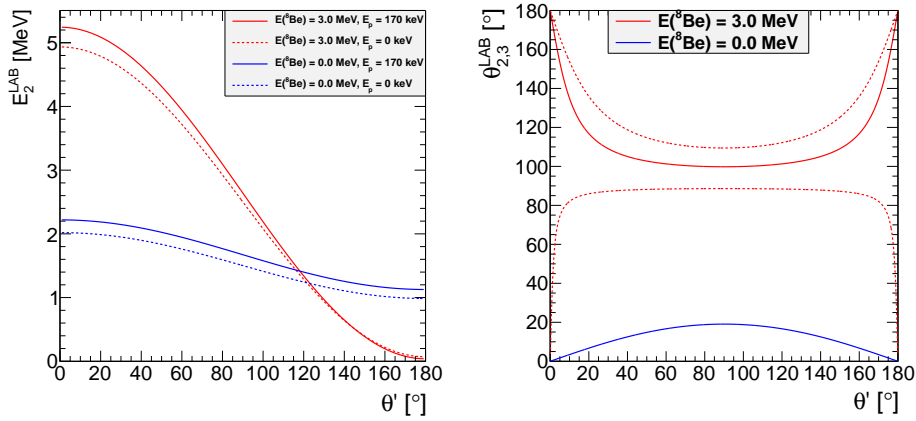
$$\mathbf{v}_1^{\text{LAB}} = \mathbf{v}_{\text{cm}} - \begin{pmatrix} \cos \theta_{\alpha, ^8\text{Be}} \\ \sin \theta_{\alpha, ^8\text{Be}} \end{pmatrix} \mathbf{v}_1 \quad (2.5)$$

$$\mathbf{v}_{2,3}^{\text{LAB}} = \mathbf{v}_{\text{cm}} + \begin{pmatrix} \cos \theta_{\alpha, ^8\text{Be}} \\ \sin \theta_{\alpha, ^8\text{Be}} \end{pmatrix} \mathbf{v}_{^8\text{Be}} + \begin{pmatrix} \cos \theta' - \sin \theta \\ \sin \theta' \cos \theta' \end{pmatrix} \mathbf{v}'_{2,3}. \quad (2.6)$$

Here $\theta_{\alpha, ^8\text{Be}}$ is defined as the the angle between the beam axis (i.e. the motion axis of the center-of-mass) and the ^8Be direction as seen from the ^{12}C frame.

In the present experiment we aim to detect all three α -particles. For such an experiment two points are worth emphasizing. Firstly, the measured energy for one of the secondary α -particles can become quite low due to the ^8Be recoil motion. E_2 or E_3 will in fact become zero if $Q_1 = 3Q_2$ for $\theta' = 0^\circ$ or $\theta' = 180^\circ$ respectively. This behavior can complicate the experiment due to difficulties in detecting particles of low energy. In the present experiment our detection thresholds are located around a few 100 keV (see Section 4.1.3). For fixed $Q_1 + Q_2$, i.e. fixed ^{12}C excitation energy, the energies will depend on the ^8Be excitation energy, θ' and to a smaller degree on $\theta_{\alpha, ^8\text{Be}}$. The dependence of E_2^{LAB} on θ' when choosing $\theta_{\alpha, ^8\text{Be}} = 0^\circ$ and $E_{\text{proton}} = 170$ keV is shown in Figure 2.3a for the $^8\text{Be}(\text{gs})$ and $^8\text{Be}(3\text{ MeV})$ channels. The limiting case where the beam energy is zero is also shown. We note that, especially for the ^8Be channel, there is a strong dependence on the break-up angle. The effect of a having non-zero $\theta_{\alpha, ^8\text{Be}}$ is visualized in Figure 2.4c and 2.4d where it is seen to be largest for the ground state channel due to the small Q_2 .

The second thing, which is important to keep in mind, is the size of the relative emission angles. These will affect the triple coincidence detection efficiency. For decays going to the ground state of ^8Be the energy of the secondary α -particles will come primarily from the ^8Be recoil motion resulting in near co-linearity between the primary and secondary α -particles. To which extent this is the case is shown in Figure



(a) Laboratory α -particle energy as function of the break-up angle in the ^8Be system. Curves are shown both for $^8\text{Be}(\text{gs})$ and $^8\text{Be}(3 \text{ MeV})$ and the effect of center-of-mass motion is illustrated by comparing situations with proton energies of 0 keV and 170 keV.

(b) Curves showing the laboratory break-up angle $\theta_{2,3}^{\text{LAB}}$ as function of the break-up angle in the ^8Be system. The $^8\text{Be}(3 \text{ MeV})$ curve is flanked by two dotted curves which correspond to $^8\text{Be}(3 \text{ MeV} - \Gamma/2)$ and $^8\text{Be}(3 \text{ MeV} + \Gamma/2)$

Figure 2.3: Plots showing the variation in secondary α -particle energy (a) and break-up angle between the secondary α -particles (b) as function of break-up angle in the ^8Be system. The initial ^{12}C energy is 16.1058 MeV and $\theta_{\alpha, ^8\text{Be}}$ is chosen to 0° .

2.3b where $\theta_{2,3}^{\text{LAB}}$ peaks around 20° for $\theta_{\alpha, ^8\text{Be}} = 0^\circ$. The situation is quite different for the ^8Be first excited channel. This break-up channel is represented by the solid red curve in Figure 2.3b which shows that the two secondary α -particles are emitted in obtuse angles relative to each other for all θ' . The dotted line above corresponds to a ^8Be energy raised from 3.0 MeV by the half width of the first excited state, while the lower lying dotted line corresponds to lowering by the same energy in which case the secondary α 's can be emitted in the same direction. These examples are calculated for $\theta_{\alpha, ^8\text{Be}} = 0^\circ$. The dependence on both θ' and $\theta_{\alpha, ^8\text{Be}} = 0^\circ$ is seen in Figures 2.4a and 2.4b which clearly show that $\theta_{2,3}$ depends very little on $\theta_{\alpha, ^8\text{Be}}$.

For a ^{12}C break-up at 16.11 MeV we now have an overview of the energies and relative break-up angles to be expected purely from kinematical considerations. This knowledge is useful for the interpretation of the measured energy spectra and important when designing the experiment (see Chapter 4).

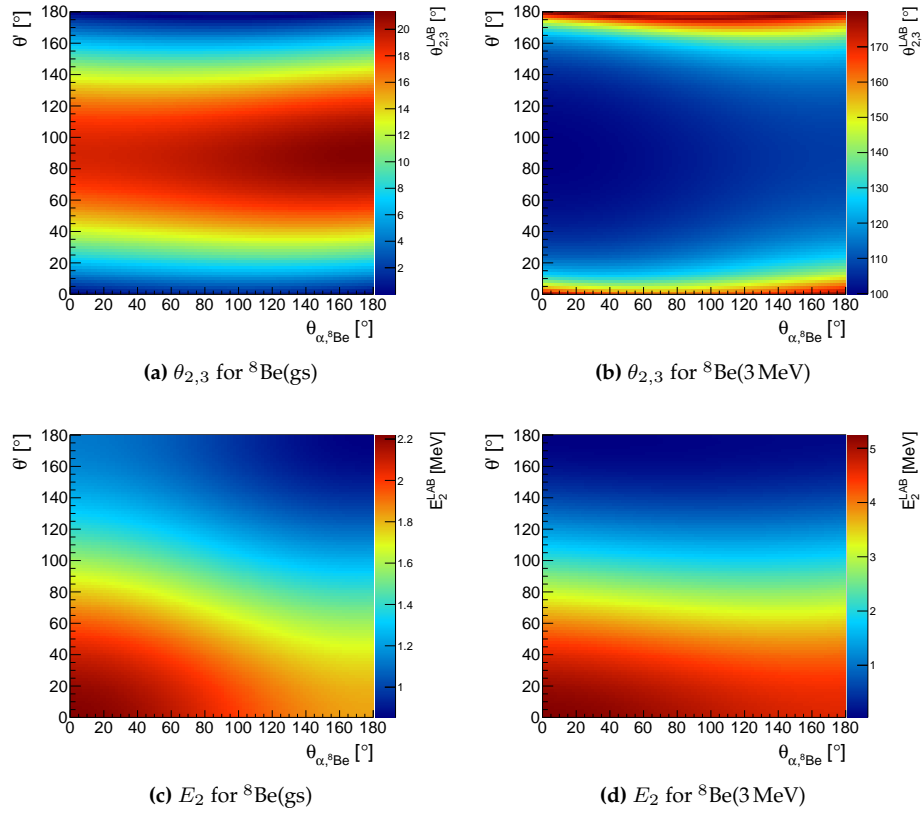


Figure 2.4: Plots showing the dependence both on θ' and $\theta_{\alpha, ^8\text{Be}}$ for the break-up angle between the secondary α -particles (panels **a** and **b**) and the energy for one of the secondary α -particles (panels **c** and **d**). Both quantities are measured in the laboratory reference frame. Panels **a** and **c** refer to break-up's proceeding through $^8\text{Be}(\text{gs})$ while Panels **b** and **d** refer to the excited state channel.

2.1.2 Angular correlations

The previous section told us how the α -particles can be distributed based on kinematical calculations alone. Correlations in the emission angles between the primary and secondary α -particles give rise to anisotropic angular distributions. This has the consequence that some regions on the kinematical curves in Figure 2.3a and 2.3b will be favored compared to others.

The existence of angular correlation in a double cascade (i.e. two break-up steps) can be understood from a few simple arguments: If we observe only one of the radiations (the primary and secondary α -particles in the present case) and assume an

unpolarized initial state the angular distribution will be isotropic. Each magnetic sub-level emits anisotropically but since they are populated equally no direction in space is singled out. However, when observing two subsequent radiations, the emission of one with respect to the other will not be isotropic. The observation of the first radiation singles out a direction in space and the sub-levels of the intermediate state are populated according to different transition probabilities. The radiation emitted from the intermediate state is then distributed anisotropically with respect to the direction of the first radiation.

A general formalism for understanding angular correlation is discussed in [Bie53]. The formalism for *direction-direction correlation* is applied in this work and a brief overview is given here. We consider an initial state of spin j_1 which decays by emission of a spin-0 particle to an intermediate state of spin j which subsequently decays to a final state of spin j_2 by emission of another spin-0 particle. Our spin-0 particle is an α -particle. We denote the orbital angular momentum associated with the first and second emission as l_1 and l_2 respectively. The angle between the second emission and the first as measured in the rest frame of the intermediate state is given as β . This angle corresponds to $180^\circ - \theta'$ (see Figure 2.2). The correlation function - the function that determines how to weight the kinematical curves - is given as

$$W(\beta) = \sum_{\nu} b_{\nu}(l_1) b_{\nu}(l_2) A_{\nu}(l_1 l_2 j_1 j_2 j) P_{\nu}(\cos \beta), \quad (2.7)$$

where the summing runs over all even ν from 0 to $\min\{2l_1, 2l_2, 2j\}$. The function $b_{\nu}(l)$ is defined as

$$b_{\nu}(l) = \frac{2l(l+1)}{2l(l+1) - \nu(\nu+1)}, \quad (2.8)$$

and $A(\nu) = F_{\nu}(l_1 j_1 j) F_{\nu}(l_2 j_2 j)$ where the F_{ν} 's are found in [Bie53]. As an example let us calculate $W(\beta)$ for the case where our initially populated 2^+ level decays via the first excited state in ^8Be . We have $j_1 = 2$, $j_2 = 0$ and $j = 2$ while $l_1 = \{0 \vee 2 \vee 4\}$ and $l_2 = 2$. For this example we choose $l_1 = 2$, which, as will be shown later, best describes the break-up data. We get

$$\begin{aligned} W(\beta) &= 1 - 0.1531 (3 \cos^2 \beta - 1) + 0.0918 (35 \cos^4(\beta) - 30 \cos^2(\beta) + 3) \\ &\approx 1.12 + 0.80 \sin^2(2\beta). \end{aligned} \quad (2.9)$$

This angular correlation function will favor θ' angles around 45° and 135° , which means that specific secondary α energies will be favored according to Figure 2.3a.

2.1.3 Dalitz plot

A Dalitz plot provides a useful way of representing the phase space by the minimum number of observable quantities in a three body break-up. It was originally devel-

oped to represent the three-body decay of K mesons into π mesons [Dal53] and today the Dalitz plot technique is used widely in particle and nuclear physics.

The measurement of two energies in a three-body break-up gives complete kinematical information (see Section 2.2) and this pair of energies are represented on the coordinate axes in a Dalitz plot. A key feature of the Dalitz plot is the constant phase space volume over the plot. Pure phase space decays will therefore be distributed uniformly over the plot meaning that any structures in the density of the plot are due to either symmetries or dynamical effects in the break-up. The Dalitz plot will exhibit certain forbidden regions depending on the spin and parity of the decaying resonance [Zem64, Fyn09]. For states with ill determined properties some spin-parities can be ruled out based on the measured Dalitz plot distribution and the spin and parity can in some cases be determined, see [Kir10] for an example. The dynamical effects are those of most interest in this work and the usefulness of Dalitz plots in this respect will be commented on later.

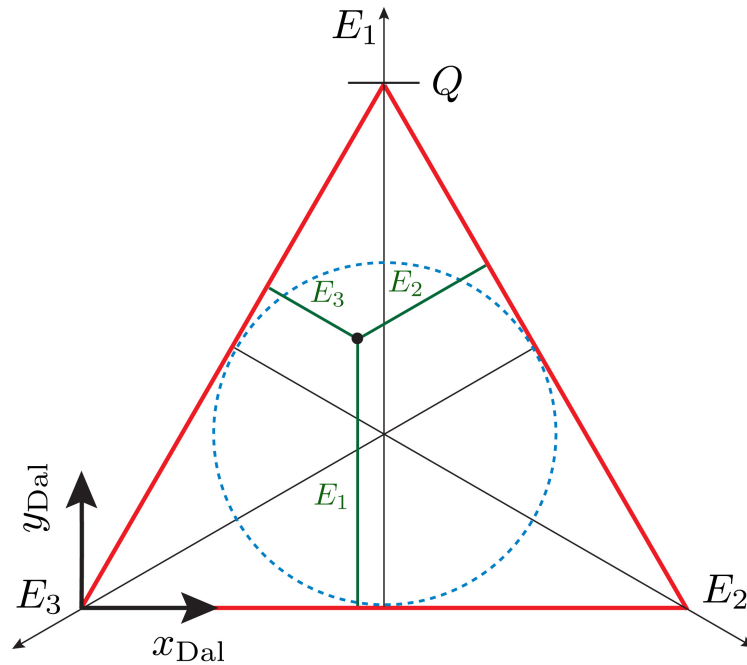


Figure 2.5: Definition of the Dalitz plot. The triangle defines the phase space region allowed by energy conservation while the circle illustrates the region allowed by momentum conservation for a fully non-relativistic case.

The Dalitz plot can be visualized as an equilateral triangle where the distances to the sides give the energies of the three particles, see Figure 2.5. As the sum of

these distances equals the height of an equilateral triangle we know that this height is Q . Energy conservation therefore requires events to be located inside the triangle. The dotted blue circle has radius $Q/3$ and marks the region allowed by momentum conservation. The Dalitz coordinates $x_{\text{Dal}} = \frac{1}{\sqrt{3}}(2E_2 + E_1)$ and $y_{\text{Dal}} = E_1$ are as already stated given in terms of only two of the measured energies. From here on the presented Dalitz plots are centered around the point in phase space where the three α -particles have the same energy and we normalize the energies E_i to the decay energy $\varepsilon_i = E_i/Q$. In this case, after some simple trigonometric manipulations, the Dalitz coordinates are given as

$$x_{\text{Dal}} = \frac{1}{\sqrt{3}}(2\varepsilon_2 - \varepsilon_1 - 1) \quad (2.10)$$

$$y_{\text{Dal}} = \varepsilon_1 - \frac{1}{3}. \quad (2.11)$$

The Dalitz plot exhibits sixfold symmetry due to the three particles being identical and the fact that the energies can be ordered in six different ways.

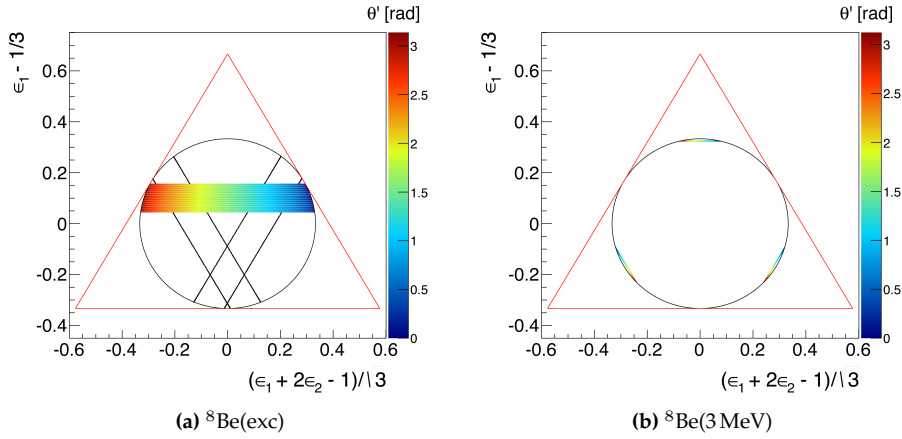


Figure 2.6: Dalitz plots for the break-up of the 16.11 MeV state. Clear structures appear as a consequence of the sequential decay through the ${}^8\text{Be}$ ground state (b) and first excited state (a). The plots are constructed only by considering the kinematics in the break-up and assuming a symmetric level profile for the first excited state with $\Gamma = 1.5$ MeV. The color scale, most easily seen in (a), shows how the break-up angle θ' depends on the position in the Dalitz plot.

The use of Dalitz plots will prove very helpful in the present work for understanding the experimental detection acceptance and as a tool for analyzing the break-up mechanism. Based only on the kinematics involved in the break-up, as described in Section 2.1.1, we construct Dalitz plots for the 16.11 MeV break-up through the ${}^8\text{Be}(\text{gs})$ and ${}^8\text{Be}(1.\text{exc.})$ channels. These plots are shown in Figure 2.6 where clear structures are visible due to the sequential character of the decay. The resonance pro-

file of the $^8\text{Be}(1. \text{ exc.})$ state is pictured as a being uniform with a width of 1.5 MeV. More detailed aspects concerning the real resonance profile and interference effects (see 2.2.1), which determine the variation perpendicular to the Dalitz plot bands, are not included. Besides giving a rough idea about the expected distribution, the figure also reveals how angular correlations will influence the distribution. If we consider the angular correlation function in Eq. 2.9 and the horizontal band in 2.6a, where the color scale shows the break-up angle θ' , we see that intensity minima are expected at the ends of the band and in the center.

For comparison of different Dalitz plot distributions the construction of one dimensional projections are helpful. Figure 2.7 shows three different choices for coordinates to project on, namely the ρ , ξ and η coordinates which are defined as

$$\begin{aligned} (3\rho)^2 &= (3\varepsilon_i - 1)^2 + 3(\varepsilon_i + 2\varepsilon_j - 1)^2 \\ 2\sqrt{3}\xi &= 1 - 2(\varepsilon_i - \varepsilon_j) \\ 2\sqrt{3}\eta &= 3 - 2(\varepsilon_i - 2\varepsilon_j). \end{aligned}$$

The Dalitz plot exhibit sixfold symmetry and by choosing $\varepsilon_1 > \varepsilon_2 > \varepsilon_3$ collapses the plot into the slice shown Figure 2.7. These projection will be used in this work for comparison between measured and theoretical Dalitz plot distributions.

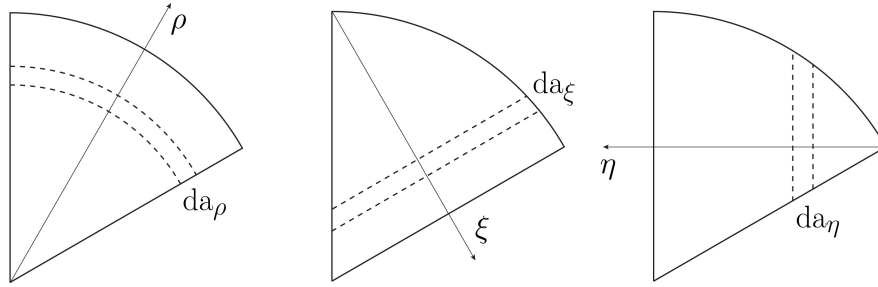


Figure 2.7: Geometrical visualization of the projected coordinates ρ , ξ and η in the Dalitz plot.

2.2 Complete kinematics

One often refers to measurements where the decay fragments are measured in *complete kinematics*. This means that a complete description of the decay is possible in terms of the kinematical variables, or put differently - it is possible to obtain the Dalitz plot distribution for all decay events.

Imposing conservation of energy and momentum for a general reaction of the

type $p_a + p_b \rightarrow p_1 + p_2 + \dots + p_n$ implies that

$$E_a + E_b = \sum_{i=1}^n E_i \quad \text{and} \quad \mathbf{p}_a + \mathbf{p}_b = \sum_{i=1}^n \mathbf{p}_i, \quad (2.12)$$

where $E_i = m_i^2 + \mathbf{p}_i^2$ ($i = a, b, 1, \dots, n$) are the relativistic energies. The n momentum vectors in the final state have to satisfy the conditions in Eq. 2.12 which define the $3n - 4$ dimensional phase space [Byc73]. For the $3-\alpha$ break-up we then have to measure 5 scalar variables in order to obtain full kinematical information.

The setup used for this experiment (see chapter 4) allows us to detect the α -particles emitted from the decaying ^{12}C resonances. Detecting a particle gives its energy and direction which means that we need to detect two or three of the α -particles in order to obtain complete kinematics. If we detect all three particles, in what we call a multiplicity-three event, the full information is immediately available and the initial ^{12}C excitation energy is found by adding the center-of-mass energies. For multiplicity-two events the energy of the undetected α -particle is found from momentum conservation.

2.2.1 Decay amplitude

The $3-\alpha$ break-up amplitude is fully determined by the relative energy of the two secondary α -particles ($E_{2,3}$) and the break-up angle θ' . Here the break-up amplitude is understood as the probability of populating a specific point in the phase space defined by the momenta of the three particles - or equivalently as a point in the Dalitz plot. The $E_{2,3}$ dependence for this amplitude relies on the resonance profile of the intermediate ^8Be level. For an isolated level this profile is given in the R -matrix formalism [Lan58a] as

$$\rho(E) = \frac{1}{\pi} \frac{\frac{1}{2}\Gamma_2}{(E_{2,3} - E_\lambda + \Delta E)^2 + \Gamma_2^2/4}, \quad (2.13)$$

where

$$\Gamma_2 = 2P_{l_2}(E_{2,3})\gamma_{\lambda_2}^2, \quad \Delta E = [S_{l_2}(E_{2,3}) - S_{l_2}(E_\lambda)]\gamma_{\lambda_2}^2. \quad (2.14)$$

Here E_λ is the formal resonance energy, Γ_2 is the width of the ^8Be resonance and l_2 is the orbital angular momentum between the secondary α -particles. P_{l_2} is the penetrability giving the probability for the secondary α -particles to tunnel through the Coulomb and centrifugal barriers and S_{l_2} is the so-called shift function (see Appendix A for the definition). The decay amplitude $|f(E)|^2$ for the $3-\alpha$ break-up is obtained by multiplying Eq. 2.13 with the decay strength to the ^8Be resonance ($\Gamma_1 = 2P_{l_1}(E_{2,3})\gamma_{\lambda_2}^2$). For overlapping broad resonances of the same spin and parity

the simple profile in Eq. 2.13 fails to give an accurate description due to interference effects.

The amplitude needs to be symmetrized in the coordinates of the three identical α -particles as required by Bose statistics. This is not the case for Eq. 2.13. In order to account for symmetrization the modified R -matrix expression from [Bal74] is used in this work:

$$f = \sum_{m_b} (lm_a - m_b j_b m_b | j_a m_a) Y_l^{m_a - m_b}(\theta_{\alpha, \text{sBe}}, \phi_{\alpha, \text{sBe}}) Y_l^{m_a - m_b}(\theta', \phi') \quad (2.15)$$

$$\times \frac{\sqrt{\Gamma_1 \Gamma_2 / \sqrt{E_1 E_{2,3}}} e^{i(\omega_l - \phi_l)} e^{i(\omega'_l - \phi'_l)}}{E_\lambda - \gamma_2^2 [S_{l'}(E_{2,3}) - E_{l'}(E_\lambda)] - E_{2,3} - i\frac{1}{2}\Gamma_2}, \quad (2.16)$$

where $\theta_{\alpha, \text{sBe}}$ and θ' are the angles already defined in this text while $\phi_{\alpha, \text{sBe}}$ and ϕ' are the corresponding azimuthal angles. j_a and j_b are the spins of the states in ^{12}C and ^8Be with m_a and m_b specifying the directions. $\omega_l - \phi_l$ is the Coulomb minus hard sphere phase shift.

The symmetrization gives rise to the so-called order of emission interference effects which have been studied e.g. in [Bro65] and [Bal74]. Basically the point is that even if we obtain complete kinematical information about the ^{12}C break-up it is not possible to distinguish the first emitted particle from the secondary particles if they are not kinematically separated. For a given pair of measured angles $(\theta_{\alpha, \text{sBe}}, \phi_{\alpha, \text{sBe}})$ and (θ', ϕ') each of the three possibilities correspond to a different $E_{2,3}$. The symmetrization is obtained by summing Eq. 2.16 for the three different choices before taking the complex norm square.

A prime example demonstrating the importance of the interference is found in the break-up of the 1^+ state at 12.71 MeV [Bal74, Fyn03]. In [Fyn03] a sequential model based on a slightly modified version of Eq. 2.16 was shown to fit data better than the direct break-up model and a sequential model not including interference. That interference plays a role for the 12.71 MeV state is hardly surprising since it only decays through the broad first excited state of ^8Be in which case more than one term in the summation of Eq. 2.16 will contribute. The fact that the bands in the Dalitz plot - which correspond to different ordering - overlap (as in Figure 2.6a) is another way of picturing the importance of interference. Decays from the 16.11 MeV level proceeding through the ^8Be ground state will on the other hand not be affected by interference since the primary α -particles are separated kinematically from the secondary α -particles (see Figure 2.6b).

The slight adjustment to Eq. 2.16 which was made in [Fyn03] incorporate a rough procedure for describing Coulomb interactions between the primary α -particle and the secondary emitted α -particles. This interaction is neglected in the simple sequential picture. The correction is carried out by introducing extra barrier penetrabilities

in the numerator in Eq. 2.16 calculated for an specific α - α distance R and relative angular momentum L . This method for approximating the effect of the final state Coulomb repulsion is also utilized in the present work.

Motivation

In this work we probe ^{12}C resonances using the $\text{p} + ^{11}\text{B}$ reaction. To be more specific, we populate the $(J^\pi = 2^+, T = 1)$ resonance at an excitation energy of 16.11 MeV and our aim is twofold. Not only will we measure the $3\text{-}\alpha$ break-up of this state but we will also search for rare γ -decays from it. The γ -delayed particle emission process provides, as will be explained, a selective and sensitive probe to the interesting excitation region around 10-12 MeV in ^{12}C .

This chapter gives first a brief overview of some of the work done previously on the $\text{p} + ^{11}\text{B}$ reaction with particular attention to studies of the 16.11 MeV 2^+ state. Thereafter follows a detailed explanation of the γ -delayed particle emission method and our motivation will be discussed in detail.

3.1 $\text{p} + ^{11}\text{B}$ studies

1932 marked an important year in nuclear physics. This was the year where J D Cockcroft and E T S Walton used artificially accelerated protons for the first time to produce nuclear disintegrations [Coc32a]. This inspired many other researchers to investigate how nuclei disintegrate when bombarded by low energy protons. This led, among other things, to the important confirmation of Gamow's theory of barrier penetration. In 1951 Cockcroft and Walton were awarded with the Nobel prize for their pioneering work some twenty years earlier.

One of the first reactions studied by Cockcroft and Walton was $\text{p} + ^{11}\text{B}$, the same reaction we utilize today. Through range measurements of the particles emitted from the compound nucleus they suggested that it breaks up by emitting three α -particles [Coc33]. There Soon followed more detailed investigations of the reaction [Oli33, Dee36]. Kinematical information about the three-body break-up at a beam energy of 300 keV was obtained by [Dee36] and Figure 3.1 shows their measured value for the energy released in the reaction, while Figure 3.2 is the single particle energy spectrum which they describe as break-up through the $^8\text{Be}(1.\text{exc.})$. This is indeed the only decay option as they were measuring on the tail of the 2^- state at 16.57 MeV, which due to parity conservation cannot decay to the $^8\text{Be}(\text{gs})$. They came to the conclusion that the common mode of disintegration was into two α -particles at angles 150° to

180° relative to each other, with the third α -particle receiving little energy.

Since this pioneering work, the α -particle distribution and the break-up mechanisms involved at various energies have been the subject of numerous studies. Interference effects in the break-up have for example been studied in e.g. [Bro65] but a complete understanding of the break-up mechanism for several ^{12}C resonances is still missing. This is exemplified in [HB87] and [Sta11] which disagree on the decay mechanism for the 2^- resonance at $E_{\text{proton}} = 675$ keV. In [Sta11] the break-up data was found to be best described with $l_1 = 3$, disagreeing with the work in [HB87] reporting $l_1 = 1$.

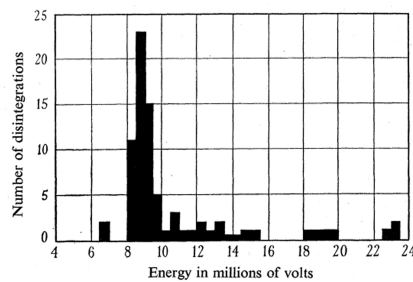


FIG. 1—Distribution of the observed energy releases.

Figure 3.1: Spectrum from [Dee36]. 79 values for the 3α sum energy measured from the $p + ^{11}\text{B}$ reaction. The sum energy was obtained from a pair of α -particle energies, deducing the third energy from conservation of momentum.

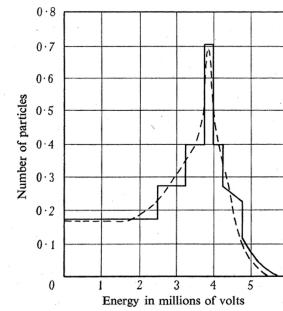


FIG. 3—Energy distribution of α -particles from boron bombarded by protons. — calculated distribution; - - - distribution of Oliphant, Kempton, and Rutherford.

Figure 3.2: Spectrum from [Dee36] showing the measured α -particle energy spectrum from the $p + ^{11}\text{B}$ reaction. The dashed line represents a calculation of the expected distribution assuming break-up via $^8\text{Be}(1.\text{exc.})$

The $p + ^{11}\text{B}$ reaction also draws interest from several other areas. From an astrophysical point of view this reaction is important since it is the primary process for depleting the stellar ^{11}B abundance and plays a role in determining the depth of stellar convection zones [Boe05]. The $p + ^{11}\text{B}$ reaction has also attracted attention due to its candidacy as an aneutronic source for future fusion reactors [Ros03]. Recently there have been promising developments in fusion reactions with laser accelerated protons and a laser generated plasma of boron [Lab13]. Cross sections for the $^{11}\text{B}(p,3\alpha)$ reaction have been measured e.g. in [HB87] (covering 22 - 1100 keV), [Dav79] (covering 35 - 1500 keV) and more recently in [Spr12] (covering 150 - 3800 keV).

3.2 16.11 MeV resonance

A sharp resonance in the $p + {}^{11}\text{B}$ reaction shows up at a proton laboratory energy of 162 keV. This resonance corresponds to the ${}^{12}\text{C}$ level at 16.11 MeV with $J^\pi = 2^+$ and $T = 1$. It is the first 2^+ isospin 1 resonance in ${}^{12}\text{C}$ and is the isobaric analogue of the first excited states in ${}^{12}\text{N}$ and ${}^{12}\text{B}$. Its total width is 5.3 ± 0.2 keV and it predominantly decays by α -particle emission [AS90]. It is interesting that a state which is unbound by 8.8 MeV with respect to particle disintegration can have such a narrow width. This fact was discussed already in 1938 where the newly invented concept of isospin was invoked in order to explain the low decay rate [Opp38]. In fact, for a pure isospin state with $T = 1$, the decay into a final state with $T = 0$ is forbidden. However, α -decays are observed from this state, which must be a consequence of an isospin impurity in it. This impurity occurs due to mixing with a [$J = 2^+, T = 0$] state in ${}^{12}\text{C}$. The state responsible for this mixing is not known, but the 2^+ state 4.44 MeV and the Giant Dipole Resonance has been discussed as possibilities in [Lin77].

In the experiment reported on in this thesis the 16.11 MeV resonance is populated through the $p + {}^{11}\text{B}$ reaction with the aim of studying the $3\text{-}\alpha$ break-up. Many studies of this resonance utilizing the same reaction have been carried out in the past. An interesting result, from these earlier studies, is on the mechanism governing the break-up proceeding through the first excited state in ${}^8\text{Be}$. Both [Que69] and [Hud72] find that this break-up is best described by assuming an angular momentum of 2 in the relative motion between the first emitted α -particle and ${}^8\text{Be}$. Interference occurring in the decay amplitude also pose an interesting phenomenon that was measured by [Tre72] and [Hud72]. Several other studies of this resonance using the $p + {}^{11}\text{B}$ reaction have been conducted, see e.g. [Deh65, Gou71, HB87].

3.2.1 Our Motivation

Our experimental setup, which will be described in Chapter 4, is better suited for measuring the 3-particle final state than the ones used in previous experiments. This alone gives motivation for conducting yet another experiment on $p + {}^{11}\text{B}$. From high quality data we will be able to extract information on the decay mechanism of the 16.11 MeV state. Our main aim for this study is however to use this state as a gateway for performing γ -spectroscopy on low lying resonances in ${}^{12}\text{C}$. Through this approach we hope to gain more information on the ${}^{12}\text{C}$ resonance spectrum with the possibility of unravelling questions related to the ${}^{12}\text{C}$ structure. The idea behind this method and further motivation will be explained in detail below.

3.3 γ -delayed α -emission

This section will motivate and explain in detail the use of γ -decay as a spectroscopic tool for studying resonances in ^{12}C . First an introduction to γ -decay in general.

3.3.1 γ -decay

Electromagnetic interactions causes an excited state in a nucleus to decay. The decay occasionally proceed by internal conversion, where an atomic electron is ejected, or by internal electron-positron pair production, but in most cases it happen by emission of a electromagnetic radiation - called γ -decay. Nuclei excited above the lowest particle emission threshold usually decay by emission of particles with γ -decay being less favorable. This difference hangs fundamentally on the nuclear force being stronger than the electromagnetic ditto. It is however possible for γ -decay to compete with particle emission if particle emission is hindered by Coulomb or centrifugal barriers, or by conservation laws.

Energetics

A γ -decay example relevant for this work is shown in Figure 3.3 where the 2^+ state at $E_i = 16.11$ MeV in ^{12}C decays to the 1^+ state at $E_f = 12.71$ MeV. The γ -ray will carry most of the released energy ($\Delta E = E_i - E_f$), while the rest goes to recoil motion of the nucleus. By applying conservation of energy and momentum,

$$\begin{aligned} E_i &= E_f + E_\gamma + E_{\text{recoil}} \\ \mathbf{p}_i &= 0 = \mathbf{p}_\gamma + \mathbf{p}_{\text{recoil}}, \end{aligned} \quad (3.1)$$

the γ energy can be determined in a non-relativistic manner:

$$E_\gamma = M_0 c^2 \left(\sqrt{1 + \frac{2\Delta E}{M_0 c^2}} - 1 \right). \quad (3.2)$$

For the example in Figure 3.3 $\frac{\Delta E}{M_0 c^2} \approx 3 \times 10^4$ and we can approximate Eq. 3.2 as

$$E_\gamma = \Delta E - \frac{\Delta E^2}{2M_0 c^2}, \quad (3.3)$$

so the recoil energy is $\frac{\Delta E^2}{2M_0 c^2}$, which in this example amounts to 0.5 keV. Thus, one may usually neglect this small energy and assume $E_\gamma = \Delta E$.

Transition rate

The transition rate $\lambda_{i \rightarrow f}$ for decays from an initial state described by the wave function ψ_i to a final state with wave function ψ_f is given by Fermi's Golden rule

$$\lambda_{i \rightarrow f} = \frac{2\pi}{\hbar} |\langle \psi_f | H_{\text{int}} | \psi_i \rangle|^2 \rho(E_f), \quad (3.4)$$

where the H_{int} is the interaction part of the Hamiltonian describing the charged particle interaction with the electromagnetic field and $\rho(E_f)$ is the density of final states. Usually one wants to put Eq. 3.4 on a form where the so-called reduced matrix element, describing the coupling between the initial state and final state due the relevant interaction operators, enters explicitly. This however requires a quite long calculation which will be omitted here. Instead, a few important points will be emphasized in the following, for a detailed calculation refer to e.g. [Sie87].

The interaction Hamiltonian includes the product of the electromagnetic current operator $\hat{\mathbf{J}}$ and the vector potential operator $\hat{\mathbf{A}}$ which is given in terms of the photon creation and annihilation operators \hat{a}_l^\dagger and \hat{a}_l

$$\hat{\mathbf{A}} = \sum_k \sqrt{\frac{2\pi\hbar c}{Vk}} \left(\hat{a}_k e^{i\mathbf{k}\mathbf{r}} + \hat{a}_k^\dagger e^{-i\mathbf{k}\mathbf{r}} \right) \boldsymbol{\varepsilon}_k, \quad (3.5)$$

where k is the photon wave number, $\boldsymbol{\varepsilon}_k$ is the photon polarization and V is the cavity volume inside which the calculation is carried out. The exponentials $e^{i\mathbf{k}\mathbf{r}}$ and $e^{-i\mathbf{k}\mathbf{r}}$ represent plane waves of incoming (absorption) and outgoing (creation) photons. Since the nuclear states are eigenstates of angular momentum, it is useful to expand the plane waves in spherical harmonics

$$e^{i\mathbf{k}\mathbf{r}} = 4\pi \sum_{l=0}^{\infty} \sum_{m=-l}^l i^l j_l(kr) Y_l^m(\theta_k, \phi_k) Y_l^m(\theta, \phi), \quad (3.6)$$

where l is the orbital angular momentum, $j_l(kr)$ are the spherical Bessel functions, (θ_k, ϕ_k) are the angles of the photon and (θ, ϕ) are the angles of \mathbf{r} . The product of $\boldsymbol{\varepsilon}_k e^{i\mathbf{k}\mathbf{r}}$ is then usually written in terms of the total angular momentum L (i.e. including both the photon spin and orbital angular momentum), its z -projection and the orbital angular momentum l . L defines the multipolarity of the emitted radiation. Eventually, after calculating $\rho(E_f)$, one reaches the following result for the transition rate

$$\lambda([E/M]L) = \frac{8\pi(L+1)}{L[(2L+1)!!]^2 \hbar} \left(\frac{E_\gamma}{\hbar c} \right)^{2L+1} B([E/M]L), \quad (3.7)$$

where $[E/M]$ denotes either electric or magnetic radiation. We introduce $B([E/M]L)$ as the reduced transition strength giving the square of the multipole operator matrix element between the initial and final nuclear states. The difference between the electric and magnetic transitions comes about due to the their different operators which

enter in $B([E/M]L)$. Reduced transition strengths depend on the structure of the states involved and are often the quantity of interest in nuclear physics. We can judge whether a transition is relatively strong or weak by comparing the measured transition strength to calculated values. One often compares to single-particle Weisskopf units which are calculated using a simple model.

The multipole order is given in terms of the angular momentum carried away by the photon as 2^L , where $L = 1$ gives the dipole, $L = 2$ the octupole and so on. Eq. 3.7 shows that the transition rate depends strongly on L and the dependence on the energy goes as E_γ^{2L+1} . The factors of E_γ comes from the phase space (E_γ^2) and $|\langle\psi_f|H_{\text{int}}|\psi_i\rangle|^2$ (E^{2L-1}), where the dependence on L comes from the plane wave expansion in which $j_l(kr) \propto (kr)^L = (\frac{E_\gamma}{\hbar c})^L$. The parity of the multipole radiation is determined by the parities of the associated operators and is given as $(-1)^L$ and $(-1)^{L+1}$ for EL and ML respectively.

Weisskopf units

It is convenient to express the decay rates in terms of the so-called *Weisskopf* units. These units give the transition rates for the electric and magnetic multipoles assuming the γ -transition to be caused by a single nucleon changing from one shell model state to another, and that the radial wave functions are constant over the nuclear interior and vanish outside. Comparing measured rates with the calculated Weisskopf rates tells us to which extent the initial and final states can be described as single particle shell model states. If the measured rate is much higher it could suggest that more than one nucleon is responsible for the transition indicating more complex structure involving collective motion.

In Table 3.1 the Weisskopf estimates for the total γ -width, $\Gamma = \hbar\lambda_W$, are presented. We see that the electric transition rates are higher than the corresponding magnetic transition rates, which is due to the stronger dependence on the nucleon number. For ^{12}C , $\Gamma_W(EL)$ is larger by a factor of ~ 17 for the lowest multipoles. The rate depends strongly on L as the rate decreases by many orders of magnitude when increasing L . Physically we understand this behaviour as a consequence of the photon wave length being much larger than dimension of the nucleus. This reduces the decay rate for higher multipoles since, as already pointed out, the photon wave number enters in the transition rate to a power of $2L$. In general this means that the lowest multipole transition that is allowed will dominate the decay. This brings us to a discussion of the γ selection rules.

Table 3.1: Weisskopf estimates for $\Gamma_W(E/M L)$. The γ energies E_λ are in units of MeV. A is the nucleon number for the decaying nucleus.

L	$\Gamma_W(E L)$ [eV]	$\Gamma_W(M L)$ [eV]
1	$6.8 \times 10^{-2} A^{2/3} E_\gamma^3$	$2.1 \times 10^{-2} E_\gamma^3$
2	$4.9 \times 10^{-8} A^{4/3} E_\gamma^5$	$1.5 \times 10^{-8} A^{2/3} E_\gamma^5$
3	$2.3 \times 10^{-14} A^2 E_\gamma^7$	$6.8 \times 10^{-15} A^{4/3} E_\gamma^7$

Selection rules

Conservation of angular momentum and parity introduces selection rules in γ -decays. Since the initial and final states have definite parity the parity of the emitted photon is strictly determined from the change in parity between the states. The multipole parity is $(-1)^L$ for electric transitions and $(-1)^{L+1}$ for magnetic transitions. If the initial state has spin J_i and the final state has spin J_f , conservation of angular momentum requires the angular momentum of the photon to be in the interval:

$$|J_i - J_f| \leq L \leq J_i + J_f. \quad (3.8)$$

As a consequence the transition between states with a large difference in J will occur via high multipoles resulting in relative low decay rates.

Decays with $\Delta T = 0$ are called *isoscalar* while decays with $\Delta T = 1$ are called *isovector*. One of these decay modes can be enhanced relative to the other, depending on the multipole transition in question. For example $\Delta T = 0$ E1 transitions are forbidden in self-conjugate nuclei and for M1 transitions are the isovector mode favored compared to the isoscalar mode.

3.3.2 Our idea: γ -delayed α -emission

As pointed out in Chapter 1, we need more accurate information about the low-energy resonance spectrum of ^{12}C as the properties of resonances in this region play an important role for our understanding of the ^{12}C structure. It was also pointed out that these properties impact on the 3α reaction rate at elevated temperatures in stellar interiors, and in combination with the recent experimental development it seems natural to strive after more experimental information about this energy region in ^{12}C .

Conducting experiments of different types is essential in the search for elusive states, like those belonging to the long sought rotational band build upon the Hoyle state. Measuring the matrix elements involved in different ways of population can give valuable information about the structure of the final state. Also, experimental

probes of different kinds have different sensitivities, so if one type of experiment fails to observe a proposed state it does not necessarily rule out its existence. This can first of all be due to quantum mechanical selection rules, making the population of given states forbidden to some order, or, Secondly, it can be due to structure differences between the initial and final states.

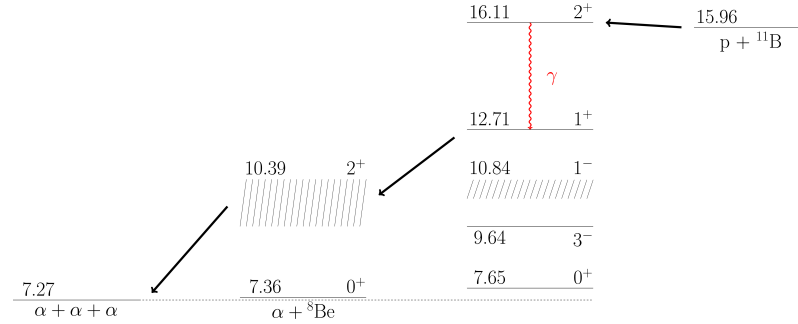


Figure 3.3: Scheme picturing $p + {}^{11}\text{B}$ populating the 16.11 MeV state and the subsequent γ -delayed 3- α break up.

Motivated by the many questions concerning the nuclear structure of ^{12}C , in particular the existence of the 2_2^+ state and its properties, the present work presents a new experimental technique for probing low-energy resonances in ^{12}C . As in the experiment by [Zim13b] we utilize electromagnetic transitions, but instead of γ -excitation we use γ -decay from a higher lying level to populate the resonances of interest. The lower lying states will be populated at different rates depending on the involved spin and parities according to the electromagnetic selection rules, see Section 3.3.1. This difference is a key ingredient in our approach, and it introduces a high degree of selectivity since the transition rate drops rapidly when going to higher multipoles.

Our way of doing γ -spectroscopy does not involve direct detection of the emitted γ -rays. Instead, information about the decay is obtained indirectly by measuring the γ -delayed α -particles. Since the γ -energy equals the difference between the energy levels to within 1 keV (see Eq. 3.3), the excitation energy of the daughter level is obtained simply by summing the energies of the three α -particles. This approach offers new possibilities for doing γ -spectroscopy on broad levels compared to conventional methods involving germanium detectors or scintillator based detectors. There are several reasons for this, one being that our type of detectors (see 4.1.1) have a more simple response function than modern γ -detectors. See Section 9.3 for the description of a response function. This is inherently important for broad resonances, and especially in the case of ^{12}C where several very broad resonances exist at relative low excitation energies. Furthermore, the intrinsic efficiency of Ge-detectors limits

their applicability for measuring rare decays, which in particular is important for the present study where we aim at observing very small γ -branches. Dealing with multi-particle final states and the capability of measuring in multi-coincidence gives near-background free spectra adding to the advantage of our method.

Hence, there are many benefits in using the γ -delayed approach, but it should be noted that even though the recoil energy is at the level of 1 keV the single particle energies will be quite broadly distributed. The shift in energy of an α -particle due to the recoil motion of the γ -daughter can, to first order in the recoil velocity, be calculated from the α -particle velocity in the rest frame of the daughter nucleus, \mathbf{v}'_α , and the velocity of the recoiling daughter in the rest frame of the initial state, $\Delta\mathbf{v}_{\text{recoil}}$,

$$\Delta E_{\text{recoil}} = M_\alpha \mathbf{v}'_\alpha \Delta\mathbf{v}_{\text{recoil}} = \frac{M_\alpha}{M_{^{12}\text{C}}} v_\alpha p_\gamma (\boldsymbol{\alpha} \cdot \boldsymbol{\gamma}) \quad (3.9)$$

$$= \left[\frac{2 M_\alpha (M_{^{12}\text{C}} - M_\alpha) Q_1}{M_{^{12}\text{C}}^3} \right]^{1/2} p_\gamma (\hat{\boldsymbol{\alpha}} \cdot \hat{\boldsymbol{\gamma}}), \quad (3.10)$$

where $\hat{\boldsymbol{\alpha}}$ and $\hat{\boldsymbol{\gamma}}$ are unit vectors pointing in the direction of the α -particle and the recoil, p_γ is the momentum of the emitted γ and Q_1 is the energy released in the $\alpha + {}^8\text{Be}$ break-up. As an example, decays to the 1^- state at 10.84 MeV will give $\Delta E = \pm 62$ keV for $\hat{\boldsymbol{\alpha}} \cdot \hat{\boldsymbol{\gamma}} = \pm 1$. This is clearly a non-negligible broadening that needs to be corrected for when looking at single particle spectra. In this work we will only be interested in the the sum-energy spectra for the γ -delayed events.

The method of γ -delayed particle emission has previously been applied to the levels at 12.71 and 15.11 in ^{12}C [Kir09]. These levels were populated in $^{10}\text{B}({}^3\text{He}, p\alpha\alpha\alpha)$ and $^{11}\text{B}({}^3\text{He}, d\alpha\alpha\alpha)$ reactions and clear γ -transitions were seen by analyzing the final four-body state in complete kinematics. For the 12.71 MeV state transitions to unbound states were seen for the first time and for the 15.11 MeV state three new transitions to broad resonances were identified. That experiment serves as proof of principle and emphasizes the power of using the detection of multi-particle break-ups as a tool for γ -spectroscopy in the case of ^{12}C .

Opportunities with the 16.11 MeV level

As already mentioned we use the $p + {}^{11}\text{B}$ reaction to populate the ($J = 2^+, T = 1$) resonance at 16.11 MeV. This state is reachable at a low-energy accelerator ($E_{\text{res}}^{\text{Lab}} = 162$ keV) and its spin-parity and isospin is favorable for the purpose of our study. The $T = 1$ nature of this state, responsible for its small α -width (see 3.2), makes it suitable for our purpose. A high rate of 3- α break-ups from the 16.11 MeV would increase the signal-to-noise level in the interesting energy region, complicating the observation of γ -delayed events. Table 3.2 shows the spin and parities of states reachable from a 2^+ level by the two lowest electric and magnetic multipole transitions. Also shown

in the table are Weisskopf transition strengths for decays to excitation energies at 10 MeV and 13 MeV. Remember, these strengths are based on large assumptions and only serve as a rough guiding for what to expect. It is the job of the experimentalist to measure, if possible, the actual strengths and make comparisons to the single particle estimates or more sophisticated theoretical predictions. Nevertheless, the Weisskopf estimates in Table 3.2 give us a quantitative measure of the expected strengths. For example it is clear that the rate difference between $L = 1$ and $L = 2$ emission is considerably larger at 13 MeV than at 10 MeV.

Table 3.2: Possible spin and parities for states to be reached by E1, M1, E2 and M2 transitions from a 2^+ state. Also shown is the Weisskopf estimates Γ_W for decays to excitation energies of 10 and 13 MeV.

El/Ml	16.11 MeV, 2^+	Γ_W [eV]	
		10.0 MeV	13.0 MeV
E1	$1^-, 2^-, 3^-$	81.1	10.7
M1	$1^+, 2^+, 3^+$	4.78	0.629
E2	$0^+, 1^+, 2^+, 3^+, 4^+$	1.14×10^{-2}	3.89×10^{-4}
M2	$0^-, 1^-, 2^-, 3^-, 4^-$	6.67×10^{-4}	2.27×10^{-5}

We are now in a position to discuss the opportunities of using the 16.11 MeV level as gate way for studying the resonance spectrum above the Hoyle state. Starting out by considering possible E1 transitions, which are expected to dominated the decay rate, we can populate 1^- , 2^- and 3^- states. Known states with these quantum numbers exist at 9.64 MeV (3^-), 10.84 MeV (1^-) and 11.83 MeV (2^-), and could potentially hinder or complicate the observation of the 2_2^+ state, as was the case with the 3^- state in the inelastic scattering experiments [Fre09, Ito11]. 2^+ states can, together with 1^+ and 3^+ states, be reached by M1 decays. Besides from the 2^+ strength measured in recent years there are no other states with these quantum numbers in the region around 10 MeV. Next we consider E2 transitions, which are expected to be a few orders of magnitude weaker than M1. This difference can prove pivotal for our work, as the very broad ($\Gamma \sim 3$ MeV) 0^+ resonance at 10.3 MeV was a major complication both in the scattering experiments and in experiments using β -decay [Hyl10b]. All states below the 16.11 MeV level, besides the one at 15.11 MeV, have $T=0$, so we are looking for isovector transitions.

The most recent experiment measuring the γ -decay of the 16.11 MeV state dates back to 1977 [Ade77] where a NaI detector was used to measure γ -transition in ^{12}C . The main aim of their work was to study the isospin mixing of the 1^+ states at 12.71 MeV and 15.11 MeV in a coincidence study of the $^{10}\text{B}(^3\text{He}, p\gamma)$ reaction, but us-

Table 3.3: Here, the branching ratios are given for the four γ -branches observed in the most recent study of γ -decays from the 16.11 MeV level. The third column gives the radiative widths as they appear in [Ade77] where a value of 6.7 keV [Seg61] was used for the total width. In the fourth column revised widths are given as the updated value $\Gamma = 5.3$ keV is used [Dav79].

16.11 \rightarrow	Ref. [Ade77]			Ref. [AS90]
	Branch. ratio	Γ_γ [eV]	Γ_γ [W.u.]	Γ_γ [eV]
gs	$(1.11 \pm 0.22) \times 10^{-4}$	(0.75 ± 0.16)	0.53	0.59 ± 0.11
4.44 MeV	$(2.42 \pm 0.29) \times 10^{-3}$	(16.2 ± 2.3)	0.49	12.8 ± 1.5
9.64 MeV	$(5.81 \pm 1.19) \times 10^{-5}$	(0.39 ± 0.09)	4.0×10^{-3}	0.31 ± 0.06
12.71 MeV	$(3.53 \pm 0.74) \times 10^{-5}$	(0.24 ± 0.05)	0.29	0.19 ± 0.04

ing the $p + {}^{11}\text{B}$ reaction they also identified four transitions from the 16.11 MeV level. Their deduced values for the branching ratios and the radiative widths to the 0^+ ground state (gs), the 2^+ first excited state (4.44 MeV), the 3^- state at 9.64 MeV and the 1^+ at 12.71 MeV are shown in Table 3.3. Also shown in the table are the revised values from [AS90] where an update value for the total width is used. Our aim is to measure transitions to the states at 9.64 MeV and 12.71 MeV and compare our values for the γ -widths to the ones of [Ade77]. Both the 9.64 MeV state ($\Gamma = 34(5)$ keV) and the 12.71 MeV state ($\Gamma = 18(3)$ eV) are narrow, which makes them easier to observed by conventional methods. It is part of our motivation to identify possible γ -lines to broad states and thereby extending the proof of principle of the method to include the 16.11 MeV level.

From the known ${}^{11}\text{B}(p, 3\alpha)$ cross section at $E = 162$ keV [Dav79], we can estimate the production rate of ${}^{12}\text{C}(16.11 \text{ MeV})$. The expected rate is $3.5 \times 10^2/\text{s}$ when using a rough value of 50 mb for the total production cross section, assuming a proton current of 2 nA and a $10 \mu\text{g}/\text{cm}^2$ natural boron target. The efficiency for detecting a $3\text{-}\alpha$ breakup in multiplicity-3 is 10-15%, and since $\frac{\Gamma_\alpha}{\Gamma} \approx 1$, we will expect to measure around 50 of these per second. We may also estimate the rate a which we will be able to observe γ -decays to the 12.71 MeV level. Based on the γ -decay branching ratio (Table 3.3) and a detection efficiency of about 1% the expected rate will be around 1×10^{-4} events per second or equivalently one event per 2-3 hours.

Experiment

In this chapter the experimental details of the $p + {}^{11}\text{B}$ experiment are reported. First the setup is described including a definition of the geometry. Next the procedures involved for measuring the ${}^{11}\text{B}(p, 3\alpha)$ reaction are explained and the measurements are grouped according to the used setup. Finally details of the calibration of the setup, including a determination of the geometry and energy calibration, are given.

4.1 Apparatus

The experiment is, as described in Chapter 3, motivated by measuring the $3\text{-}\alpha$ break-up of ${}^{12}\text{C}$ resonances with the main focus on indirect observation of γ -decays. It is the job of the experimentalist to figure out which experimental setup to use for such a measurement. How to populate the initial ${}^{12}\text{C}$ resonance and how to detect the final state particles are among the obvious questions that need to be addressed in the planning process. The answer to these questions depends firstly on the equipment available, and secondly on optimization with regard to the experimental outcome. Several things are considered, but two criteria are of critical importance in the present experiment. Firstly, abundant access to beam time is necessary since the rate of γ -delayed events as estimated in Section 3.3.2 is very low. Secondly, since we aim at detecting a three particle final state in complete kinematics, we need a compact and position sensitive setup.

We used the 400 keV single-ended Van de Graaff accelerator at Aarhus University to produce protons at the required energy around 170 keV. This choice meets the first requirement above since there were no practical limitations to the amount of beam time available. Figure 4.1 gives a simple illustration of the beamline. After the acceleration the beam is turned 45° in a switching magnet and reaches the target-chamber after passing two slits used for beam collimation. A Van de Graaff accelerator has the advantage of producing a stable generating voltage. This results in stable beam energy which is advantageous when measuring on a relatively narrow resonance as we do in the present case. The target- and detection-chamber, which was pumped by an oil diffusion pump, is shown in Figure 4.2. As detection equipment two double sided silicon strip detectors (DSSSD's) and a Faraday Cup were installed in the chamber.

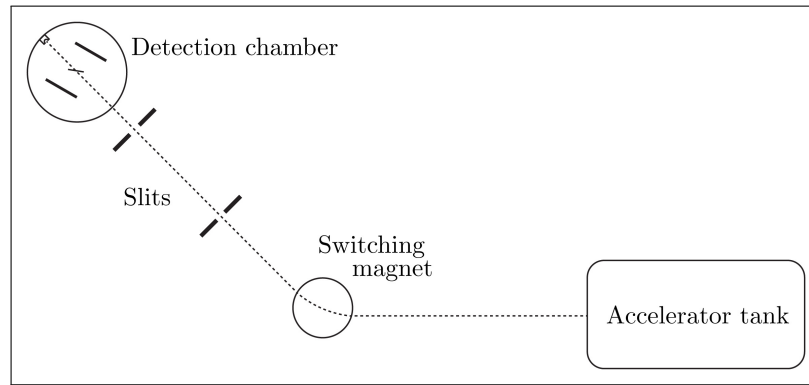


Figure 4.1: Coarse overview of the beamline showing the accelerator tank and the detection chamber.

4.1.1 Detectors

The DSSSDs are of the W design produced by MICRON [mic] and are shown in Figure 4.3. The total active area is divided into 16 strips of $3 \times 50 \text{ mm}^2$. Strips on one side run perpendicular to those on the other side, which gives 256 pixel of 3 mm^2 each, providing us with the required position sensitivity. Both detectors are $60 \mu\text{m}$ thick which is adequate for this experiment. For α -particles in silicon a range of $60 \mu\text{m}$ corresponds to approximately 9 MeV which is above the highest single particle energy produced in the reaction.

The detectors are p^+ doped on the front side while the backside is n^+ doped. They are mounted such that the front strips run horizontally. The implantation depth of the p^+ doped layer is different for the two detectors. The thicknesses of the resulting non-sensitive front layers are 200 nm and 700 nm Si equivalent respectively for the two detectors. For a more detailed detector description see [Ten04]. The detector with 200 nm deadlayer is defined as detector 1 while the 700 nm one is called detector 2. The deadlayer thicknesses, especially for detector 2, are quite large and hinder the detection of low-energy ions. This becomes an important and problematic issue for the detection of γ -delayed break-up events from ^{12}C .

4.1.2 Data acquisition

A brief description of the acquisition system used in the experiment is given here. Figure 4.4 gives a schematic overview of the different steps in the acquisition process. When a charged particle either stops in or traverses the active detector region a small current pulse is produced due to the production of electron-hole pairs. For an intrinsic silicon semiconductor the mean ionization energy ϵ , the average energy per



Figure 4.2: Photograph of the detection chamber.

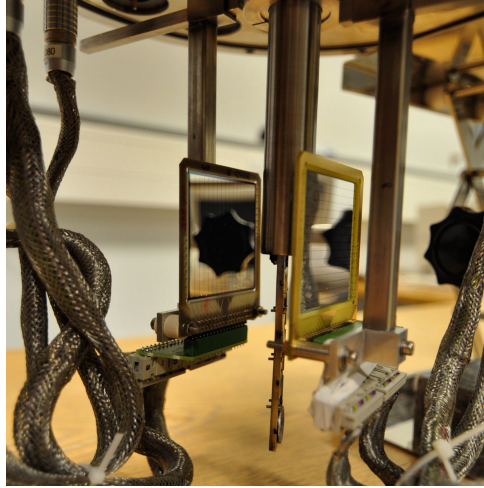


Figure 4.3: Photograph of the two DSSSDs that were used.

electron-hole pair, is 3.76 eV at room temperature, meaning that an incident particle with 1 MeV will produce roughly 2.7×10^5 electron-hole pairs. The total charge of the current pulse is therefore of the order 10^{-14} C.

This charge is impractically small to deal with making an intermediate pre-amplification step necessary. The current pulse is therefore fed into a preamplifier module, in this case a charge sensitive Mesytec MPR-32. The function of the pre-amplifier is to integrate the collected charge independently of the detector capacitance and to produce an output signal that can be passed to the next component in the chain of pulse processing. The pre-amplified signals have amplitudes of approximately 100 mV/MeV with tails of approx. 50 μ s. The capacitance of the cable between the detector and pre-amplifier increases linearly with cable length and can deteriorate the noise characteristics of the pre-amplifier. Therefore it is located as close as possible to the detector in order to minimize the capacitive loading on it.

Next in the line of processing comes the amplifier module. We used Mesytec STM16+ modules. The signal from the pre-amplifier is further amplified at this stage to a few volts, necessary for the following processing. The amplifier also shapes the input signal to produce a pulse with amplitude proportional to the collected charge in the detector and thereby to the deposited energy. The length of the shaped signal is reduced drastically in order to minimize pile-up, which occurs when signals overlap.

The shaped signal enters an analogue-to-digital converter (ADC), in this case a CAEN 785 module. Here the signal amplitude is converted into a digital number which then is proportional to the energy deposited by the incident particle. The

module used has 12 bits covering 4096 channels with an input range of 0 - 8 V. When adjusting the amplification gain one has to ensure that the highest detection energy needed can fit inside the the ADC range, which in the present case is 8.8 MeV coming from the calibration source. Taking this into account the gain was set as high as possible in order to have low energy events in as high ADC channels as possible.

The STM16+ modules have a timing filter and discriminator built in. The discriminator rejects signals with pulse heights below a specific threshold. This threshold is referred to as the trigger threshold and is set to remove electronic noise. Signals above the trigger threshold generate a delayed ECL timing signal which is sent to the time-to-digital converter (TDC), in this case a CAEN 1190 module. The timing signal keeps time information of the detected particle with respect to other signals in the event stream.

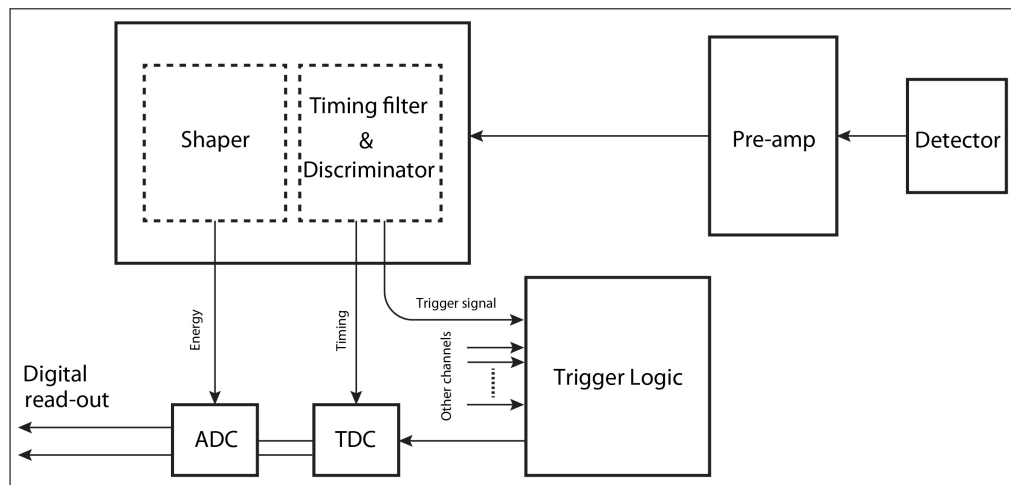


Figure 4.4: Scheme showing the electronics of the acquisition setup.

In addition a trigger signal is generated by the amplification module when above threshold. This signal is used to setup the trigger logic for the acquisition system. First the signal enters a CAEN dual timer N93B module which generates a stretched signal. This signal is sent to the acquisition control module alerting the system for a period of $2.5 \mu\text{s}$ (from here on called the ADC-window). All ADC and TDC values from any of the detectors and their strips that occur within this time window will be stored in the same event. By use of the dual timer module we generate a short signal (a few ns) positioned inside the ADC window. This signal enters the TDC module and acts as reference for the timing signals. In the analysis this time information is used to discriminate between real physical events and random coincidences. Random coincidences occur when particles from different physical events fall inside the

same ADC window. With the additional time information it is possible to reduce the number of random coincidences. At the end of the ADC window the contents of the ADC and TDC modules are converted to digital numbers and read out. This period lasts for $5.7 \mu\text{s}$, during which the system cannot accept new energy or time signals giving rise to what we call dead-time.

4.1.3 Detection threshold

We are not able to measure particle energies all the way down to zero. Energy loss effects prevent us from measuring a particle emitted from a physical process with very low energy. This problem can be minimized by choosing e.g. a detector with a thin deadlayer. But even a particle which just reaches the active detector region producing a very small current pulse can under most circumstances not be detected. Or put in a different way, although the detector actually responds to the particle, its signal will be too small to survive the acquisition chain. This is mainly due to the thresholds of the discriminator and the ADC modules.

An energy signal below the trigger threshold is lost if it is the only signal in an event (i.e. in an ADC window). If this signal on the other hand arrives inside the ADC window generated by a second signal, which then has to be above the threshold, it can be stored as sub-trigger signal. During the experiment the trigger thresholds were set for each channel at a level just above the electronic noise. This level depends on how severely external signals are picked up by the cables connecting the detectors and the STM16+ modules or at the electronic contacts. Also the ADC module has a threshold level which the digitized signal has to be above for it to be read out. ADC thresholds are typically set lower than the trigger threshold. If this was not the case sub-triggering could not occur.

In order to calculate efficiencies for detecting low-energy particles, which will be of high importance in this work, the threshold levels must be known. An accurate knowledge of the threshold levels is also necessary when allowing sub-threshold signal to survive time cuts applied in the analysis of measured data. This will be discussed in further detail in Section 5.1.1. But first one needs to determine both the trigger and ADC threshold levels in all channels. The trigger threshold is found from reaction data by plotting the number of TDC signals to ADC signals as function of energy deposited in the detector. Examples are shown in in Figure 4.5 where $\frac{N_{\text{ADC}}}{N_{\text{TDC}}}$ rises from zero to 1 with a rise "time" of a few 100 keV. This curve is interpreted as the trigger efficiency and the threshold value is determined as the energy at which the efficiency is 0.5.

Figure 4.5a shows an instructive, albeit annoying, feature. Unfortunately the trigger thresholds were set too low in detector 1 channels for some of the measurement runs. This is seen directly from the energy spectrum where an intense peak appears

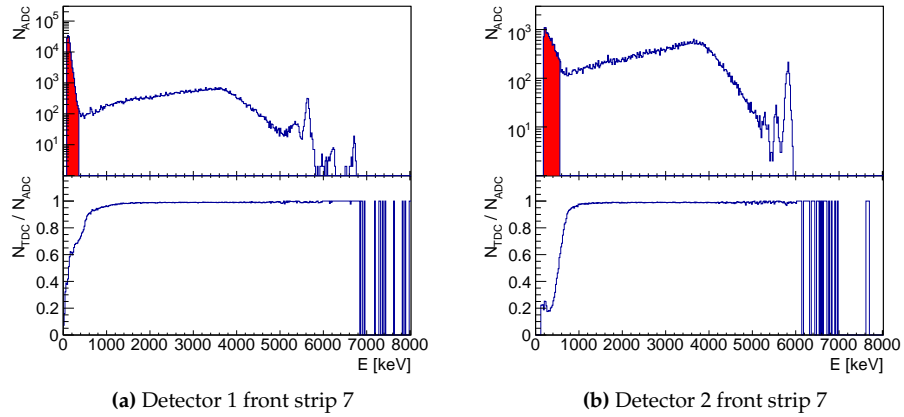


Figure 4.5: Top parts in both a and b show the raw energy spectrum. Raw refers to the fact that no cuts have been applied to the data and the energy is the deposited energy in the detectors. The red colored parts show signals that mostly are due to noise. The bottom parts display the trigger efficiency.

at low energies. This peak has contributions from electronic noise and elastically scattered protons. For detector 2 (Figure 4.5b) the trigger threshold is set higher which explains why the low-energy peak is much smaller in this case. The trigger threshold varied from channel to channel but typically was around 100 - 300 keV for detector 1 and 200 - 500 keV for detector 2.

The ADC threshold values are determined more simply as the energy at which there is a clear cut-off in the spectrum. Typically they were in the range of 10 - 100 keV for detector 1 and 100 - 200 keV for detector 2.

4.1.4 Target foils

A target ladder, also visible in Figure 4.3, was positioned in the center of the chamber. On this ladder foils of natural boron backed by carbon were mounted together with an α calibration source and a foil of Al_2O_3 . The Al_2O_3 was used for beam tuning by exploiting that it is fluorescent when bombarded by charged particles. In order to minimize shading effects a bevel was drilled in the ~ 4 mm thick ladder. Typically the foil thicknesses were around $10\text{-}15 \mu\text{g}/\text{cm}^2$ with a carbon backing thickness of $4 \mu\text{g}/\text{cm}^2$. As will be shown in Section 4.4.5 the foil thickness increased during the measurements adding to the problems of detecting low-energy α -particles. The increase in thickness is most likely due to the adsorption of carbon compounds from the diffusion pump.

4.1.5 Calibration source

A ^{228}Th α -source was used for energy calibration of the detectors. The ^{228}Th decay sequence is shown in Figure 4.6 where also the energies for the lines which are used in the calibration work are displayed. The quality of the source is quite poor and hence only the main transition lines are used. The combined thickness of the source and its front layer is found to be ~ 90 nm as described in Section 4.4.4.

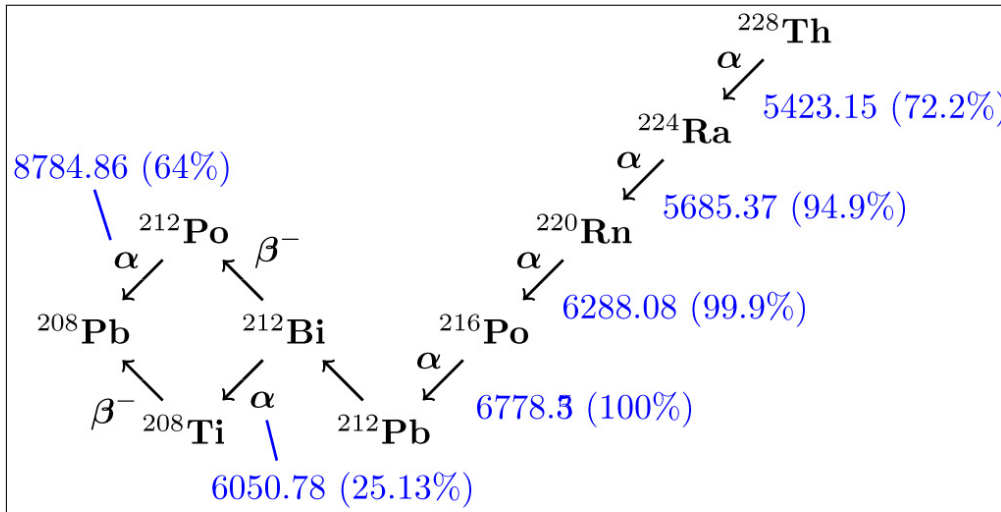


Figure 4.6: Decay sequence for ^{228}Th . Shown in keV are the energies that are used in the calibration procedure.

4.2 Geometry definition

The laboratory reference system is defined as seen in Figures 4.7 and 4.8. The z -axis is parallel to the beam axis, not necessarily coinciding with it, and the y -axis is perpendicular to the horizontal plane. The coordinates of the detector center is given by (x_D, y_D, z_D) in the laboratory frame, θ_D gives the orientation relative to the beam axis and the inclination angle of the detector is given by θ_V . A coordinate system in the detector plane, with its origin in the detector center, is defined by the x' and y' axes. With these definitions a (x', y') detector position is related to the laboratory

coordinates as

$$\begin{aligned}x_{\text{pixel}} &= x_D - x' \cdot \cos \theta_D + y' \cdot \sin \theta_V \cdot \sin \theta_D \\y_{\text{pixel}} &= y_D - y' \cdot \cos \theta_V \\z_{\text{pixel}} &= z_D - x' \cdot \sin \theta_D + y' \cdot \sin \theta_V \cdot \cos \theta_D.\end{aligned}\quad (4.1)$$

The (x', y') coordinates of the center of a pixel corresponding to front strip F and backstrip B for a DSSSD with the W1 design are

$$\begin{aligned}x' &= F \cdot 3.22 - 27.37 + 3.12 \\y' &= B \cdot 3.22 - 27.37 + 3.12.\end{aligned}$$

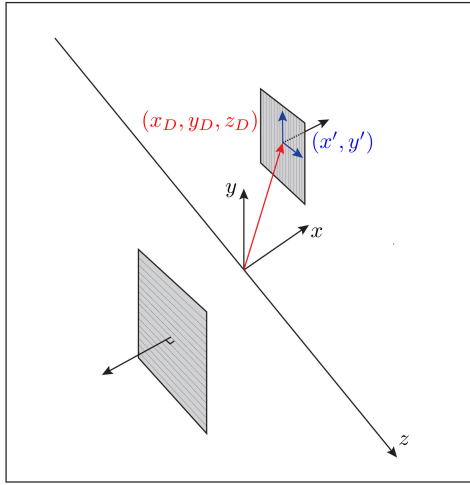


Figure 4.7: Definition of the laboratory coordinate axes (\hat{x} , \hat{y} and \hat{z}) and the local detector axes (\hat{x}' and \hat{y}').

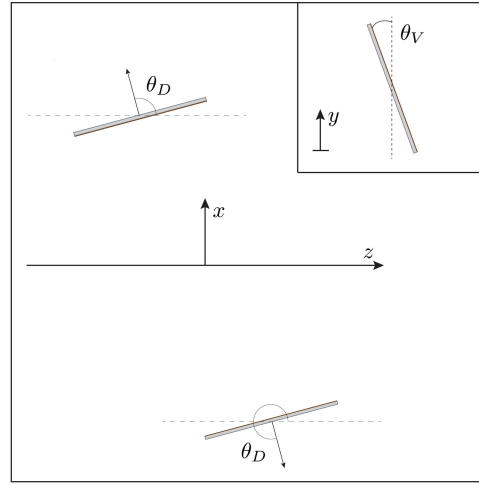


Figure 4.8: The detection setup viewed from above with definition of the angles θ_D and θ_V .

4.3 Experiment runs

In total approximately 250 hours of data was acquired on the $p + {}^{11}\text{B}$ reaction at beam energies in the range of 167-170 keV. This was over a period of four months during which changes in the setup and experimental conditions were made. The data is therefore divided into 10 groups for which the geometry of the setup is constant and where all the experimental conditions are roughly the same. The 10 groups are analyzed individually taking into account the differences between the groups. In Table

4.1 the data groups are defined in terms of the run number, beam energy and the associated geometry.

Several of the changes occurring during the experiment relate to the fact that it is a pioneering experiment where improvements were made several times during the data taking period. One essential goal was to maximize the solid angle covered by the detectors. This was done by moving the detectors as close as possible to the target without risking radiation damage and at the same minimizing shading effects caused by the target ladder.

The 16.11 MeV resonance is located 148.6 keV above the $p + {}^{11}\text{B}$ threshold corresponding to a laboratory proton beam energy of 162.2 keV. As seen in Table 4.1 the beam energy was set somewhat higher in order to compensate for energy loss in the target foil. The idea is to optimize the number of observed $3\text{-}\alpha$ break-ups by *hitting* the resonance at a favorable depth in the target foil. Since the total resonance width is 5.3 keV, and the foil energy loss for a 170 keV proton is approx. 10 keV, this involves some fine tuning of the beam energy. One could argue that the beam energy optimally should be on resonance halfway through the foil, but the backing layer on the target foil and the large difference in detector deadlayer thicknesses makes it more complicated than so. A precise calculation or simulation of the optimal beam energy is not possible since the uncertainty on target foil thickness is large. Instead the resonance profile was scanned in steps of a few keV by monitoring both the number of α_0 -particles detected in detector 1 and the number of detected $3\text{-}\alpha$ break-up events. The results are shown in Figure 4.9 where we see that both observables peak at 170 keV with a width at half maximum of approximately 10 keV. These measurements were carried out with the foil backing pointing towards the beam. For the data groups 1 - 2 and 7 - 10 the orientation of the foil was opposite explaining why a lower beam energy was chosen for the runs in these groups.

4.4 Calibration of the experimental setup

This section describes different issues concerning our understanding of the experimental setup. The name *calibration* covers our ability to take into account how the experimental apparatus reacts when used in experiment. This does not necessarily mean that a detailed understanding is needed but merely that we effectively have to be able to separate apparatus effects from the physical effects of prime interest.

4.4.1 Geometry

The first step in the data analysis is to work out the geometry of the detection setup. This means that the positions and angles of the different elements in the setup must

Table 4.1: Overview of the run groups that the data are divided into.

Groups	Runs	E _{beam} [keV]	θ _{Det1} [°]	θ _{Det2} [°]	(x ₁ , y ₁ , z ₁) [mm]	(x ₂ , y ₂ , z ₂) [mm]	θ _{foil} [°]
1	569-630	167	110	290	(20.0, -0.8, -4.5)	(-30.1, 0.0, 10.9)	229
2	633-652	167	110	290	(20.0, -0.8, -4.9)	(-30.1, -0.5, 10.9)	229
3	655-685	170	110	290	(20.0, -0.8, -9.2)	(-33.1, 0.0, 10.6)	44
4	686-701	170	110	290	(16.9, 0.0, -10.5)	(-32.1, 0.0, 9.0)	54
5	704-731	170	110	290	(16.9, 0.0, -11.2)	(-32.1, 0.0, 8.8)	54
6	746-796	170	110	290	(18.8, -0.5, -7.7)	(-24.0, -0.5, 5.8)	54
7	798-828	167	110	290	(18.6, -0.5, -5.5)	(-23.9, -0.5, 6.1)	234
8	830-856	167	105	285	(19.5, -0.8, -4.5)	(-24.6, -0.1, 4.7)	234
9	884-920	169	105	285	(19.4, 0.0, -4.5)	(-23.5, -0.5, 4.90)	234
10	921-1019	169	105	285	(19.0, 0.0, -4.9)	(-23.6, -0.5, 4.9)	234

be determined. This concerns the detector positions and the detector and target foil angles.

Uncertainties on the detector positions and angles influence the obtained precision and accuracy of the results obtained in the analysis. For that reason it is carefully considered how the geometry is determined in order to obtain good precision and minimize the risk of introducing systematical uncertainties.

It is difficult to measure the geometry directly in the laboratory at a precise level. Therefore two analytical approaches are used. Firstly, the energy calibration data is used to determine the geometry for the calibration work. The obtained geometry serves as starting point in the analysis of the data from the corresponding reaction experiment. As a second approach, and for a more accurate determination of the reaction geometry, distances and angles are adjusted until geometry dependent physical observables fit to expected values. These two ways of determining the geometry will be discussed next.

Solid angle fit

The Energy calibration data are acquired with an α -source which emits isotropically. By exploiting that the measured intensity across a detector varies according to the solid angle covered by the pixels we can find its position (x_D, y_D, z_D). The source is assumed to be point-like and located at the laboratory origin. The solid angle covered by pixel_{F,B} is estimated as

$$\Omega_{F,B} = \frac{A_{F,B} \cdot \cos \theta_{\hat{n}\vec{R}}}{R_{F,B}^2}, \quad (4.2)$$

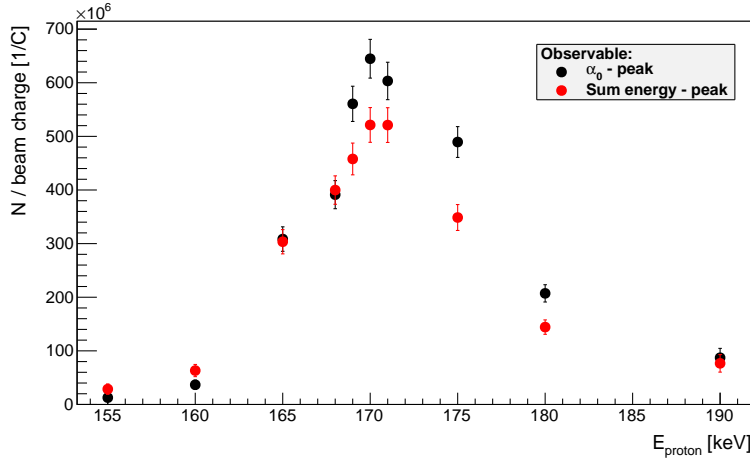


Figure 4.9: Energy scan of the 16.11 MeV resonance. The number of α_0 -particles and 3- α break-ups divided by the collected beam charge are shown.

where $A_{F,B}$ is the pixel area, R is the distance from the source to the pixel center and $\theta_{\hat{n}\vec{R}}$ is the angle between \vec{R} and the detector normal vector \hat{n} . It is assumed that \vec{R} is constant across the pixel which is the case within 1% for all geometries in this work.

The detector position is found by fitting Eq. 4.2 to the measured hitpattern. The result of such a fit is seen in Figure 4.10. In the fit-procedure the angle θ_D is fixed to the set value measured in the laboratory and θ_V is set to zero.

Center-of-mass curves

The geometry found using the calibration data cannot straightforwardly be used in the analysis of the reaction data. Either, the reaction center needs to be moved relative to the laboratory origin or the detector positions needs to be adjusted so that they are given relative to the reaction center. The latter approach was used here. The idea is that geometry dependent physical observables will provide guidance when moving the detectors. In this work the guiding was mainly obtained by observing the center-of-mass energy curve for the first emitted α -particle (see Figure 4.11), which becomes flat when the detector is moved to its true position. Here we exploit that the curve is isolated and has a small width due to the small ${}^8\text{Be}(\text{gs})$ width. Determining the geometry in this way is not as direct and intuitive as when looking at hitpatterns, but can be understood through the geometry dependence of the transformation between the laboratory and center-of-mass system. In Eq. 4.3, which transforms the laboratory energy E_{LAB} , the geometry dependence is introduced by the laboratory polar angle

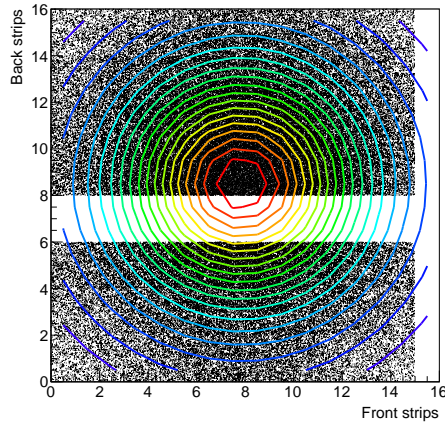


Figure 4.10: Hitpattern in detector 1 when measuring on the α -source. The contour plot is the result of a fit to the solid angles across the pixels on the detector.

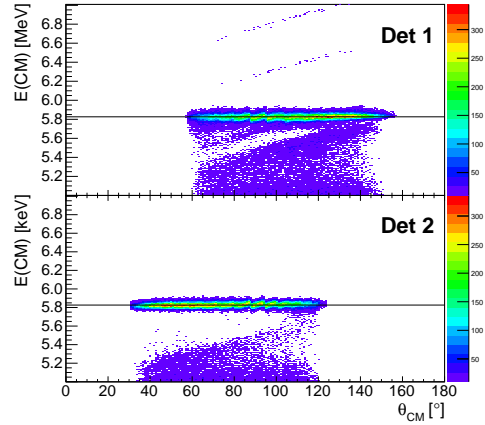


Figure 4.11: Center-of-mass curves showing the α_0 -energies when measuring on the $^{11}\text{B}(p,3\alpha)$ reaction.

θ_{LAB} :

$$E_{\text{CM}} = \gamma_{\text{CM}} \cdot (E_{\text{LAB}} - v_{\text{CM}} \cdot p_{\text{LAB}} \cdot \cos \theta_{\text{LAB}}). \quad (4.3)$$

4.4.2 Energy loss calculations

When doing simulations or when analyzing data, whether it is from reactions, calibrations or simulations, it is important to be able to correct for energy losses. This section briefly explains how the energy losses are calculated. When a charged particle passes through a slice of matter it loses energy in collisions where momentum is transferred to the electrons and nuclei of the target material. In the energy regime relevant for this work ionization of the atomic electrons is the main contributor to the energy loss. The mean energy loss, or the stopping power, for this process is given by the *Bethe-Bloch formula*, which tells us that the energy loss to good approximation is proportional to the square of the projectile charge, the electron density (in the target medium) and the inverse square of the projectile velocity. For a discussion of the physics underlying the energy loss mechanism for charged particles one would start at the *Bethe-Bloch formula*.

This mechanism is however not of particular interest here, instead we need an effective routine that calculates energy losses. For this we use the range tables calculated by SRIM [Zie08]. One could also work with the SRIM stopping powers, which are necessary for distinguishing between electronic and nuclear energy losses, but for

this work range tables are more practical. The range $R(E)$ for α -particles in silicon is shown in Figure 4.12.

A projectile with incoming energy E_{in} traverses a material of thickness d and loses the energy ΔE . This energy reduction can be determined from the corresponding range tables as

$$d = R(E_{\text{in}}) - R(E_{\text{in}} - \Delta E). \quad (4.4)$$

However ΔE enters on both sides of Eq. 4.4 which hinders a calculation in one step. The idea is to generate a spline to both the (R vs. E) and (E vs. R) sets, and start out, as indicated in Figure 4.12, by finding the range value associated with the incoming energy. According to Eq. 4.4 one subtracts the distance d and use the resulting value on the (E vs. R) spline to find $E_{\text{in}} - \Delta E$. This gives a simple procedure where we have to generate the two splines once and make two spline evaluations for each analyzed event. This routine for calculating the energy loss is quick compared to the alternative procedure where the stopping powers are integrated. Another advantage of using the range method comes from the fact that the tabulated ranges are projected ranges, which means that possible systematic errors due to angular straggling are avoided.

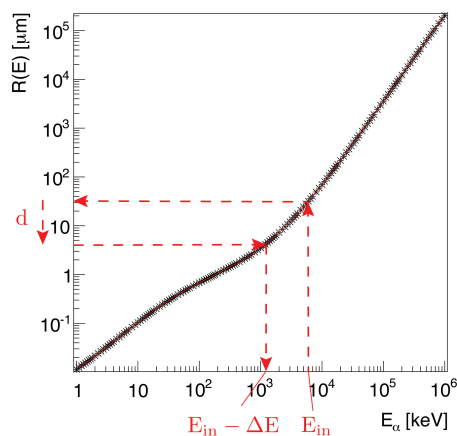


Figure 4.12: The range of α -particles in silicon. The stars are the values from SRIM and the line represents the spline made to them. The arrows are for guidance in the explanation of the energy loss calculation procedure (see the text).

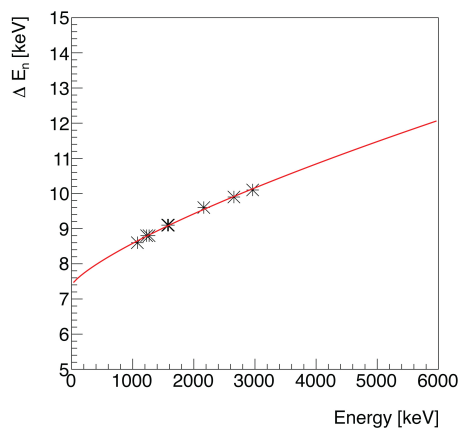


Figure 4.13: Non-ionizing energy loss of α -particles in silicon. The stars show the values from [Len86] while the line shows the parametrization used for calculating non-ionizing energy losses at arbitrary energies.

4.4.3 Non-ionizing energy losses and the pulse height defect

When a charged particle enters a semi-conductor detector not all of the deposited energy contributes to the signal measured. The energy is lost both in electronic and nuclear collisions and both of these can lead to ionization, i.e. the creation of an electron-hole pair, vacancy formation (radiation damage) and phonon production. Only the ionization process contributes to the electrical signal. The corresponding energy loss is called *ionizing energy loss* (ΔE_{ion}), while the remaining energy loss is called *non-ionizing energy loss* (ΔE_{n}). As mentioned above most of the energy loss is ionizing, mainly due to electronic collision, but the non-ionizing energy loss is non-negligible for studies aiming at few keV precision. The size of ΔE_{n} for various light ions in Si has been calculated in [Len86]. The non-ionizing energy loss for α -particles in silicon is shown in Figure 4.13 where the parametrization used in this work is shown as the solid line.

The constancy of ε for different energies and different types of radiation make semiconductors quite versatile as a tool in nuclear spectroscopy. The response of semiconductors to heavy ions is however not straightforward as the observed pulse height is substantially less than for a light ion of the same energy. This effect is known as the *pulse height defect*. There is as well a difference between protons and α -particles which is at the percentage level [Len86]. This effect only needs to be considered whenever the type of particle involved in the measurement is different from the one used in the calibration. In the work presented from the experiment at the 400 kV accelerator only the detected α -particles are analyzed and since an α -source is used for calibration no correction is needed.

4.4.4 Energy calibration

This section describes the procedure for calibrating the detectors used in the experiments. First the general calibration procedure is outlined whereafter more specific details are described. The details include corrections for energy losses in the source material and the detector deadlayer and the determination their thicknesses.

Basic procedure

Information about the energy of a detected particle is stored as a discrete value according to its ADC value. As explained in Section 4.1.2 the ADC value reflects directly the pulse height of the signal arriving from the amplifier module. The pulse height is related to the energy of the particle which in the process of detection initiated the electrical signal which, after some manipulations, reached the ADC module. Establishing the relation between the ADC value and the particle energy is the aim of the energy calibration procedure.

Depending on the needed accuracy one has to consider to what level of detail the applied calibration should be. Several effects such as non-linearity in the electronics and non-ionizing energy losses can make the calibration procedure more elaborate. In this work a linear response of the electronics in the detection system is assumed, i.e. a linear relationship between the ADC value and energy. The linear relationship is assumed after correcting for the small energy dependence on the non-ionizing energy loss (see Figure 4.13) in the detector.

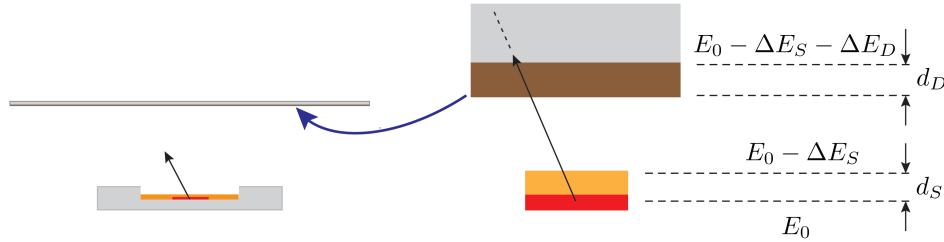


Figure 4.14: Illustration of the source and detector. The left side is drawn to scale. On the right side the source and the front of the detector are zoom in on. The yellow layer illustrates the layer on top of the source and the brown layer represent the non-active layer on the detector front side. The calibration procedure takes into account energy losses of the α particles in these layers.

The calibration is done by pointing an α source directly towards the detector to be calibrated (see Figure 4.14). An α -particle with initial energy E_0 emitted at an angle θ (relative to the detector normal) reaches the active detector volume with the energy $E_D(\theta) = E_0 - \Delta E_S(\theta) - \Delta E_D(\theta)$, where $\Delta E_S(\theta)$ and $\Delta E_D(\theta)$ are energy losses in the source and detector deadlayer respectively. Before relating the energy $E_D(\theta)$ to the measured pulse height the non-ionizing energy loss ΔE_N is subtracted. The resulting energy is the energy available for electron-hole pair production and therefore the one that should be compared to the measured pulse height.

After the energy-loss corrections are made the calibration of each strip is carried out by doing a linear fit to the $E_D(\theta) - \Delta E_N$ values against the peak positions. The calibration procedure written for this purpose could determine the peak position by fitting with a simple gaussian, a gaussian convoluted with an exponential tail, by simple mean or median finding or by use of ROOT's TSpectrum tool [Bru97]. In this experiment the TSpectrum tool was used as it was found to be more robust than the fitting method owing to the poor quality of the α -source. An example of a calibration spectrum is seen in Figure 4.15 and the associated linear fit to the known energies is shown in Figure 4.16. More details of the calibration work is explained in the following

sections.

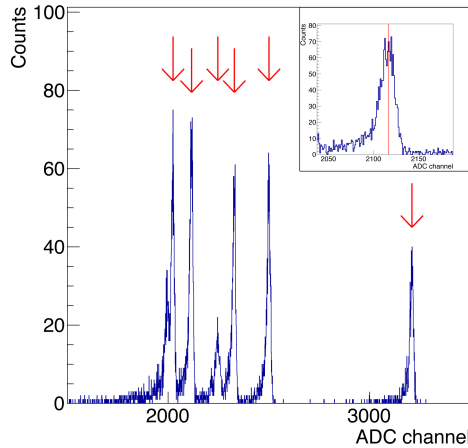


Figure 4.15: ^{228}Th calibration spectrum in a detector strip. The arrows point at the peaks used for calibration and the inset is a close up look at one of the peaks.

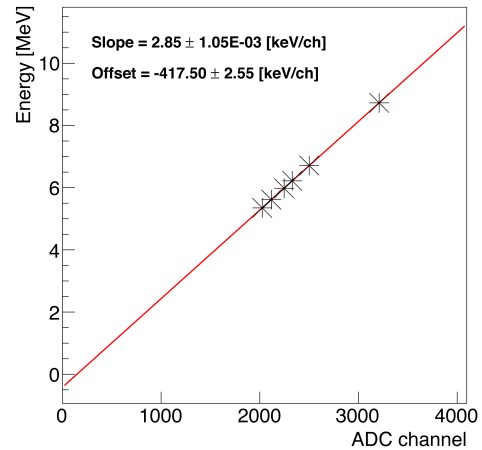


Figure 4.16: Final linear fit from which the calibration coefficients are obtained. These relate ionizing energy with ADC channel.

Source thickness

The first energy loss that the α -particles are subject to is in the source itself. To correct accurately for this the thickness of the source and its front window must be known. Information about these thicknesses were unknown beforehand for the ^{228}Th source hence these needed to be measured. For simplicity we assume that the energy is lost only in one layer, i.e. we do not distinguish between the source material and front window, and the layer is assumed to consist of graphite. Through these assumptions an effective source thickness is determined. As long as the model for estimating the thickness is the same as the one used when doing the correction in the calibration routine no systematic error should occur due to inaccuracies in the assumptions made. Furthermore the source is assumed to be point like with no spatial extension.

The thickness was determined by doing three measurements, one where the source points directly towards detector 1 and two where the source is turned $\pm 60^\circ$ relative to detector 1. This turning angle is called θ_s . The situation is pictured in Figure 4.18. The general idea is to compare the peak positions in a detector front strip (going vertically) between the two cases where $\theta_s = 0^\circ$ and $\theta_s = \pm 60^\circ$. The detector is kept stationary which ensures that any differences in the measured peak positions are due to differences in the traversed path lengths within the source. The source thickness

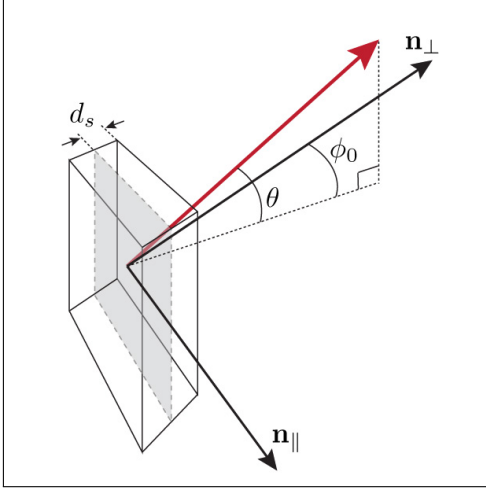


Figure 4.17: Visualization of the angles involved in the source thickness calculation

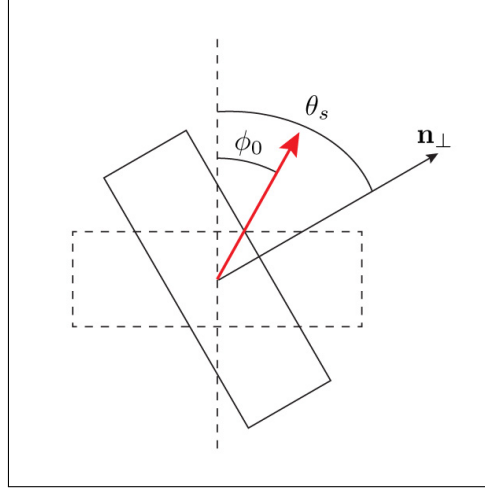


Figure 4.18: Looking in the $-\hat{y}$ direction.

is expected to be small, which means that in order to observe an effect, θ_s must be large. Since the detector is situated only about 25 mm away turns have to be made in both directions in order to cover the entire detector. The distance traversed by an α -particle for a source direction θ_s is denoted d_{θ_s} and the difference in path lengths is related to the measured energies (in the same strip) as

$$d_{\theta_s} - d_{0^\circ} = R(E_s) - R(E_s - (E_{0^\circ} - E_{\theta_s})), \quad (4.5)$$

where $R(E)$ is the range at the energy E , E_s is the tabulated source energy while E_{0° and E_{θ_s} are the measured energies. The energy E_s in Eq. 4.5 should in principle be replaced by E_s minus the energy lost in the source for θ_0° , but this would require a priori knowledge of the source thickness itself. The approximation is however quite good since the change in slope of $R(E)$ over a few tens of keV is negligible for this purpose. The measurement of E_{0° and E_{θ_s} is subject to the same approximation since it requires an already working energy calibration. Having obtained $d_{\theta_s} - d_{0^\circ}$ the source thickness d_s can be calculated as

$$d_s = [d_{\theta_s} - d_{0^\circ}] \cdot \left[\frac{1}{\langle \cos \theta \rangle} \cdot \left(\frac{1}{\cos(\phi_0 - \theta_s)} - \frac{1}{\cos \phi_0} \right) \right]^{-1}, \quad (4.6)$$

where ϕ_0 is the emission angle relative to the source normal direction when it is in the $\theta_s = 0^\circ$ position (\mathbf{n}_\perp) and θ is the emission angle relative to the \mathbf{n}_\perp - \mathbf{n}_\parallel plane. See Figures 4.17 and 4.18 for visual explanation. While ϕ_0 only varies $\approx 7^\circ$ across a front strip, θ varies by as much as 90° . The value used for $\langle \cos \theta \rangle$ is therefore averaged with respect to the solid angle in each pixel in the given front strip.

Figure 4.19 shows the peak position differences Δ_{ch} in all front strips for the calibration peak of lowest energy. The difference is observed to be highest for the central strips while it decreases outwards to strip number 1 and 15. This behavior is caused by energy loss in the source. In order to visualize this conclusion Figure 4.19 also displays how the calculated factor $\left[\frac{1}{(\cos \theta)} \cdot \left(\frac{1}{\cos(\phi_0 - \theta_s)} - \frac{1}{\cos \phi_0} \right) \right]$ (from here on called the *angle factor*) from Eq. 4.6 varies across the detector. Close to $\phi_0 = 0$, i.e. for the central strips, the angle factor is largest which fits with the observed Δ_{ch} being largest for strip 8 and 9. With the given choice for θ_s it becomes difficult to measure d_s for strips other than the central ones. This is because the angle factor approaches and crosses zero for increasing ϕ_0 , which means that the expected path difference will be small and the associated differences in peak positions will be hard to measure. For that reason only strips 8 and 9 are used for extracting a value for the source thickness. As shown in Figure 4.20 the thickness is measured and calculated for 5 of the calibration peaks in both the $\theta_s = +60^\circ$ and $\theta_s = -60^\circ$ positions. Peak number 3 has been left out because of the low number of counts in it. Combining the obtained results the source was determined have a thickness of 100 ± 4 nm (graphite eqv.).

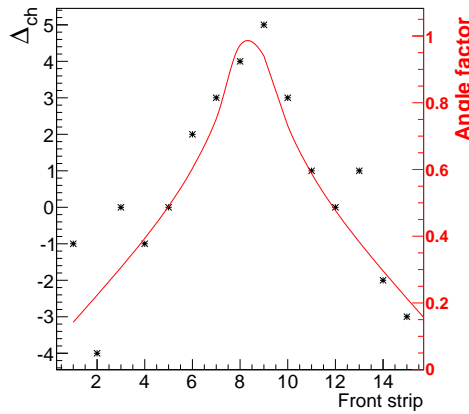


Figure 4.19: Measured differences in positions for the calibration peak of lowest energy. The results for strips 1-8 are with $\theta_s = -60^\circ$ while for strips 9-15 $\theta_s = +60^\circ$. The red curve displays the second factor in 4.6 (called the *angle factor*) which gives the expected variation in the path length difference across the detector.

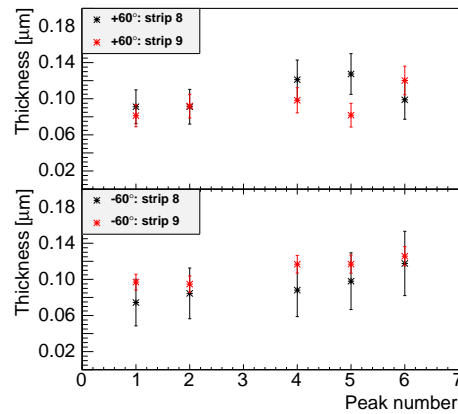


Figure 4.20: Measured source thicknesses determined by use of front strip 8 and 9. Top part is for $\theta_s = -60^\circ$ while the bottom part is for $\theta_s = +60^\circ$.

Detector deadlayer thickness

The detector deadlayers was determined to 200 nm and 700 nm Si equivalent for detector 1 and 2, respectively. This was done by analyzing the pulse height variation across the pixels in strip in measurements with the ^{228}Th α -particle source.

4.4.5 Growth on target foil

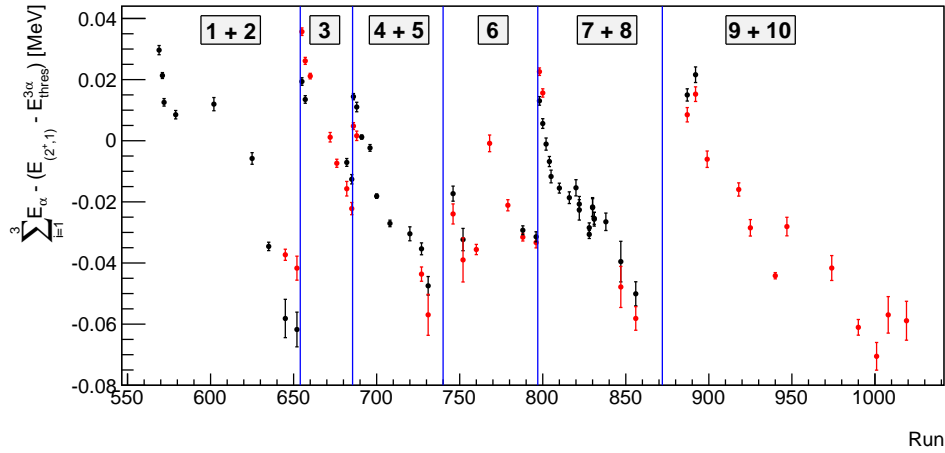


Figure 4.21: Deviation from expected 3α sum energy versus run number. The vertical lines indicate positions where discontinuities in the sum energy trend are apparent. The numbers in each division gives the run series number in accordance with the definition in Section 4.3.

During the analysis of the acquired data it became apparent that the measured α -particle energy shifted over time. The shift is observed after correcting for known changes in the setup which can introduce changes in the energy losses that the α -particles are subject to. The deviation from the expected sum energy of three α -particles is shown for some run numbers in Figure 4.21. The shift goes towards lower energies and there is a recurring structure in the deviations. Each of the data runs are analyzed with the energy calibration belonging to the relevant data group. Discontinuities in the energy shift are observed at five occasions, indicated by the vertical lines in Figure 4.21. These are in coincidence with transitions between different data-groups and thus also with shifts between the applied energy calibrations. This could point to the fact that changes in the signal amplification, and thereby the energy calibration, are responsible for the measured energy shifts. This is however not the case since the energy calibration changes very little between two data groups. This is seen in Figure 4.21 where runs just before and after the vertical lines are analyzed

using calibrations for the groups after and before the vertical line respectively. This is indicated by the fact that the alternating black and red colored points overlap into neighboring regions. In fact during all runs in the experiment the energy calibration is observed to change only by approximately 0.2%.

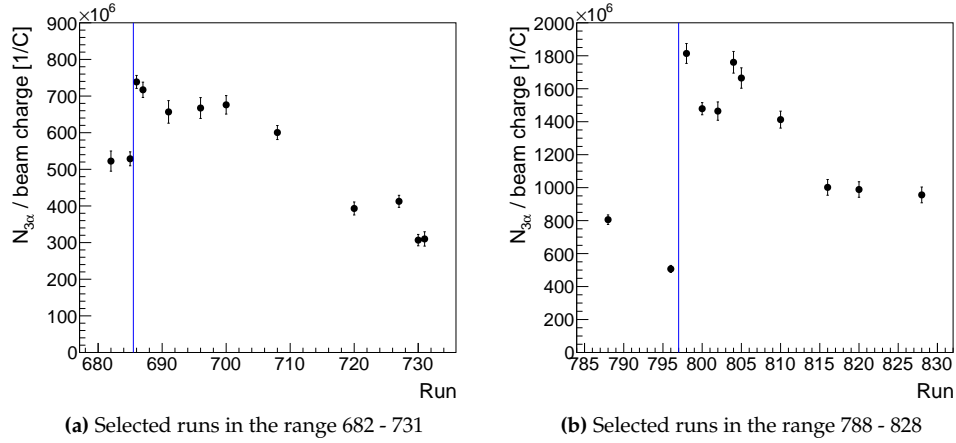


Figure 4.22: The number of 3- α events per beam charge measured from the $(2^+, 1)$ resonance.

Having established that the measured energy is shifting during the experiment we now address the question: what causes this shift? A clue is given by the fact that we hardly observe any energy shift for the α_0 -peak at 5 826 keV. Therefore it must be the low energy α -particles that mainly are shifted in energy, and since the stopping power is higher for the low energy α -particles, compared to the α_0 -particles, this behaviour indicates that the effect is caused by energy loss in some material that gradually increases its thickness. Such an effect should lower the measured 3- α rate as the detection efficiency for the low energy α -particles will decrease. This behaviour is exactly what we observe as seen in Figure 4.22 where the measured number of break-ups divided by the collected beam charge is shown around two of the transition regions. The fact the different energy calibrations are compatible excludes that the extra material should be deposited on the detectors. We conclude that the effect must be caused by adsorption on the target foil. The target chamber was pumped by an oil diffusion pump and our hypothesis is that a carbon layer grows on the foil due to contaminants from the pump. Openings of the chamber coincide with the transitions where the sum energy shifts up again indicating that this operation removes this extra layer.

In the analysis extra layers of graphite was added to both sides of the target foil in order to correct for this effect. This was done in an effective way so that the average

3- α sum energy fitted with the expected one for each of the ten data groups.

Data reduction and analysis

In this chapter the basic procedures involved for analyzing the acquired data on the $p + {}^{11}\text{B}$ reaction are described. Basic steps in the data reduction are described to begin with followed by a treatment of more specific elements related to the spectroscopy of ${}^{12}\text{C}$. Finally the routine used for simulating the break-up data is described.

5.1 Basic steps

The basic elements of the analysis are treated in the first section. These elements form the first and general steps necessary when analyzing data acquired with silicon strip detectors.

5.1.1 TDC cut

The first step of the data analysis involves the time signals (TDC values) that accompany the energy signals (ADC values) in a data event. The time information is used to remove random coincidences. This is important when measuring very weak decay branches, hence in particular for our purpose of measuring the γ -delayed break-up of ${}^{12}\text{C}$.

The procedure involves the construction of a TDC acceptance window in which the TDC signal for a particle must lie to be accepted for further analysis. The TDC window is generated by looking at the TDC spectra for each strip and selecting a region containing the physical events of interest. Optimally, the spectra only consist of one peak and a constant background, but as shown in Figures 5.1a and 5.1b, displaying the TDC spectra for the front sides of detector 1 and 2, two peaks appear right next to each other. We note an approximately constant background in the spectra. This background contains noise signals or time signals originating from physical events in random coincidence with the one that triggered the acquisition system. The narrower we construct our acceptance window, the lower the risk of random coincidences. Setting a too narrow window cuts away good break-up events.

It turns out that α -particles from the ${}^{12}\text{C}$ break-up all have time signals that fall inside the first of two peaks. This is exemplified in Figure 5.2b on page 69 where

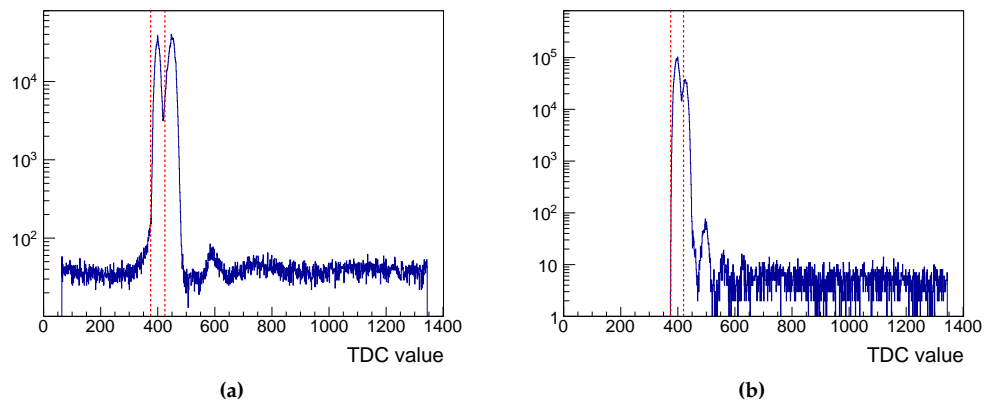


Figure 5.1: Summed TDC spectra for front side strips for a single data file with the number of counts on the ordinate. The dotted lines indicate the acceptance region. **(a)** Detector 1. **(b)** Detector 2.

the summed ADC spectrum for all front strips in detector 1 is shown when gating on the first TDC peak (as illustrated in Figure 5.1a). The broad distribution is a clear signature of the $3\text{-}\alpha$ break-up. Comparing Figure 5.2b with Figure 5.2a, which shows the ADC spectrum when all signals are accepted (i.e. no TDC gate has been imposed), we see clearly that the number of low energy signals are reduced drastically when applying the TDC gate. At the same time we do the important observation that none of the α -particles are lost. As will be shown in Figure 5.8 on page 76, the TDC gating is extremely important for our ability to measure γ -delayed events. Without it, the signal-to-noise ratio would be impractically high.

As demonstrated here, it is mainly low energy signals that lie in the second TDC peak, but why they appear in a distinct peak is less clear. It turns out that time signals in the second peak only appear in coincidence with time signals in the first peak indicating that signals in the second peak are beam induced. The amplitude of the second peak is observed to be strongly correlated with the maximum energy in an event. The higher the maximum energy the more signals in the second peak. The origin of these signals are not investigated further, we merely note that all good events fall inside the first peak.

Sub-trigger energy signals, signals which fall below the trigger threshold and therefore have no corresponding TDC signals, can be allowed to survive the TDC cut. With no way of telling if an energy signal without a TDC signal originates from electronic or beam-induced noise or from a real break-up event, all signals that are below the trigger threshold can be assumed good, while those above are rejected

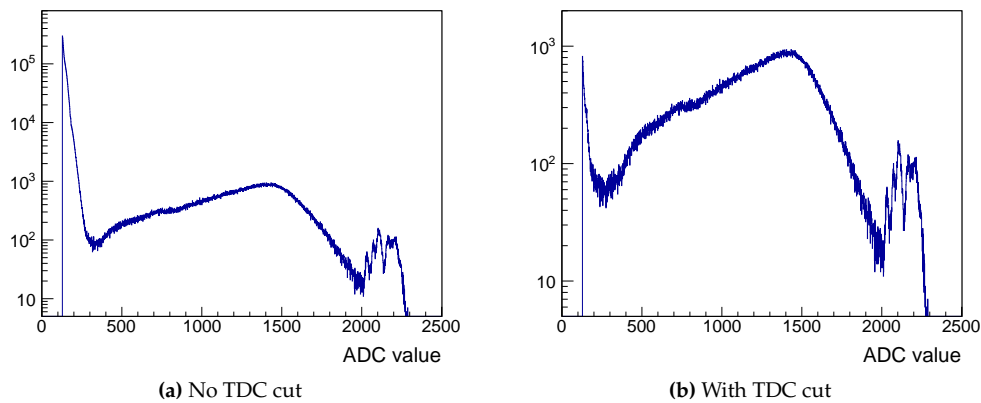


Figure 5.2: Summed ADC spectra for front side strips on detector 1 for a single data file with the number of counts on the ordinate. In **(a)** the spectrum is plotted without applying TDC cuts, while in **(b)** the TDC cuts are applied.

since they should have had a TDC signal. This requires that the trigger thresholds are known (see Section 4.1.3), and provides a way of handling low energy signals that give a higher sensitivity for low energy particles. This would be advantageous for a complete kinematics study of ^{12}C , where α -particles of low energy are expected (see Section 2.1.1). However, since our measurements are strongly affected by unwanted low energy signals, we do not allow sub-trigger signals to survive for further analysis.

5.1.2 Energy calibration

The next basic step in the analysis is the conversion from ADC values to energies, which in this context includes three different actions. Firstly, the ADC signals that survived the TDC cuts are transformed to ionizing energies. This is done by using the linear calibration coefficients which were obtained from the energy calibration of the detectors (see Section 4.4.4). Secondly, the ionizing energies are converted to incoming energies by adding the non-ionizing energy losses (see Section 4.4.3). This correction depends on the particle type, but we do not have particle type identification, hence a choice must be made concerning the particle type. Thirdly, if the chosen particle type is different from an α -particle, correction for the pulse height defect is made (see Section 4.4.3). After these operations the energies are in form of deposited energies in the active detector region, which are the same as the incoming energies since the α -particles are fully stopped in the detectors.

5.1.3 Front-back matching

As pointed out earlier, position sensitivity is needed for a complete kinematical detection of the $3\text{-}\alpha$ break-up. The segmentation of the detectors facilitates multi-particle detection, but, recalling the discussion in Section 4.1.1, a front side hit only gives position information along the horizontal direction while for a back side hit it is along the vertical direction. Combining the information about which front and back strips were hit, the position sensitivity is improved. This is important for performing accurate energy loss corrections and kinematical transformations. In a clean experiment, i.e. one with minimal noise, where only one front and back signal is measured, we naturally assume that they are due to the detection of a particle somewhere in the pixel specified by the overlap of the front and back strips that were hit. However, dealing with noise, multiple detections and particle hits in inter-strip regions, complicates the situation.

For several detections in an event, how does one assign front and back positions to a particle hit? We exploit that the number of holes and electrons, collected at the back and front sides, are approximately the same when they originate from the same particle detection. Charge collection efficiencies depend to a small degree on detector type and stopping range and will inevitably introduce differences in the measured signals at the front and back side. These differences are small enough (~ 1 keV) to be neglected in this work. For the identification of a particle we therefore require that the calibrated front and back energies match within some tolerance. Plotting these energies against each other, as done for detector 1 in Figure 5.3 using α calibration data, reveals a clear diagonal structure. Pairs of energies located on this diagonal correspond to genuine particle detections and are selected for further analysis. Our tolerance is chosen to be 150 keV, illustrated in Figure 5.4, where the difference between front and back energies are plotted using $p + {}^{11}\text{B}$ data.

Notice in Figure 5.3 the horizontal and vertical bands extending from the points of high intensity. The horizontal bands are caused by α -particles stopping in the inter-strip regions on the detector front side. Conduction band electrons in these regions are collected at the aluminum electrodes of the neighbouring strips, between which the particle stopped, thereby splitting the energy signal between them. Since the back strips run orthogonal to the front strips the corresponding back strip will most often receive the full signal. Similarly, the vertical bands in Figure 5.3 correspond to stopping in back side inter-strip regions. Notice also that the horizontal lines extend from points on the diagonal somewhat below the high intensity points. This effect is caused by the extra deadlayer of $0.9\ \mu\text{m}$ Si equivalent in the inter-strip region on the front side.

Sharing events are not selected for further analysis when applying the diagonal cut on the front vs. back energy spectrum, and as a consequence the detection ef-

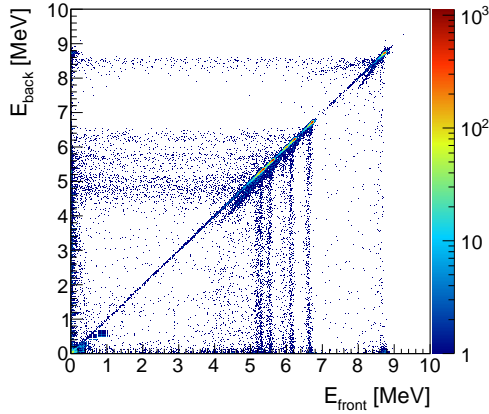


Figure 5.3: Back and front strip energies for detector 1 using the ^{228}Th source.

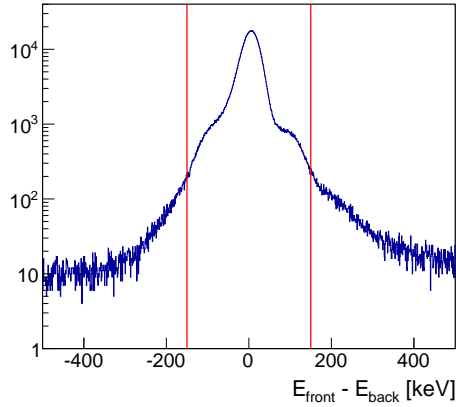


Figure 5.4: Difference between front and back energies in detector 1 using $p + ^{11}\text{B}$ data. The red lines indicate the applied tolerance level.

efficiency is reduced. For one of the detector sides this reduction is approximately $\frac{15 \cdot 100 \mu\text{m}}{16 \cdot 3.2 \mu\text{m}} = 3\%$ (inter-strip and strip element widths are $100 \mu\text{m}$ and $3120 \mu\text{m}$ respectively, see [Ten04]). If our understanding of inter-strip signals, as simple sharing between neighbouring strips, is correct, the *lost* detection efficiency can be regained by searching for neighbouring pairs of energies on one side that match with the energy of one signal on the other side. Whether to implement this in the analysis of reaction data is a matter of choice, but it has to be consistent with the procedure used for calculating detection efficiencies. In this work the efficiencies are obtained by using a simulation programme that shares the energy deposited between strips (see Section 5.4).

On Figure 5.5a the energy spectrum measured in detector 2 (for reaction data) is divided into three spectra: one for detections that lie on the front vs. back diagonal, one for sharing events between front strips and one for summing events occurring when two particles are detected in the same front strip. Similarly Figure 5.5b shows sharing on the back side and summing with two particles detected in the same back strip. Sharing events on the back side are two orders of magnitude less frequent than the directly matched events (those on the diagonal), roughly agreeing with the 3% calculated above. Sharing events on the front side are more infrequent. The sharing spectra seem to be scaled down versions of the total spectrum, which is roughly what we would expect. The large difference in sharing probability on the front and back side is less intuitive and constitutes an interesting phenomenon which has been measured and discussed in a recent paper by [Gra14]. Using proton micro-beams [Gra14] investigated inter-strip region effects for DSSSD's of type W1, the same as in the

present experiment, and found differences in the front and back side behavior. In particular they found that for inter-strip regions on the front side the measured energies do not add up to the total energy, whereas they do for back side inter-strip regions. This could be consistent with our observations, as we see fewer front side sharing events.

Unlike the number of sharing events, the number of sum events is sensitive to kinematical correlations. Since the polar angle varies up to $\simeq 7^\circ$ across front strips, and we know that the break-up angle between the secondary α -particles can fall below this value (see Figures 2.4b and 2.3b in Section 2.1.1), we expect some contribution from summing. The spectra based on summing events shows a distinctive structure which does not resemble the total spectrum. This structure fits with the expected energies for secondary α -particles emitted in the $^8\text{Be}(\text{gs})$ decay channel, in which the break-up angle - as seen from the laboratory or center-of-mass system- can become quite small.

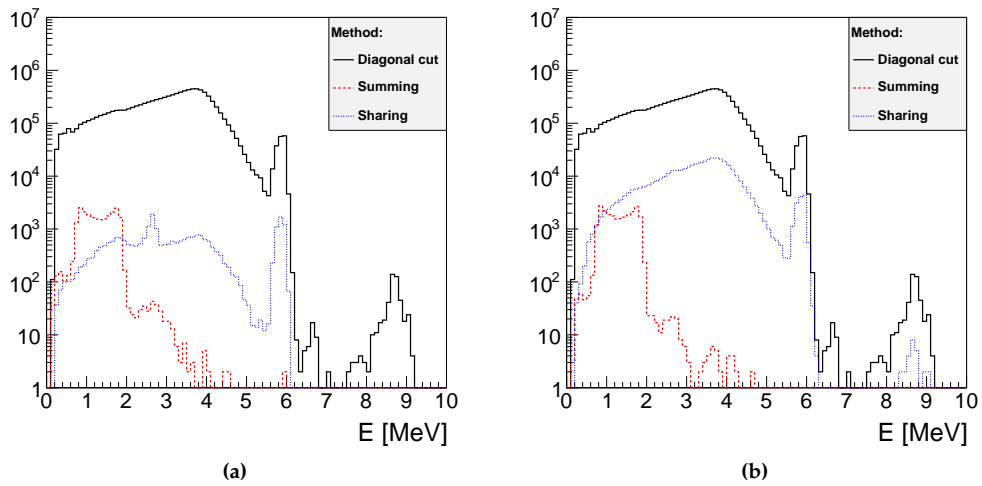


Figure 5.5: Plots showing the front-back matched energy spectrum measured in detector 2. The total spectrum is divided into three spectra depending on the front-back matching method: events lying on the front vs. back diagonal, sharing events and summing events. **(a)** Front side sharing and summing. **(b)** Back side sharing and summing.

5.1.4 Energy loss corrections and center-of-mass transformation

Having identified the energies of the detected particles, they are now transformed to the physical system of interest, in this case ^{12}C . Prior to this, we need to correct for energy loss in the detector deadlayer and target foil. Assuming the detected particle

is an α -particle firstly the deadlayer energy loss is added, and next the foil loss is added. The energy loss is calculated as described in Section 4.4.2, but in this case the arrow directions in Figure 4.12 on page 57 are opposite as we are recovering lost energy. When calculating energy losses in the foil it is assumed that the reactions take place half way through the foil.

The laboratory energies (E_{LAB}) are now transformed to the center-of-mass system (E_{CM}), which coincides with the ^{12}C rest frame. Choosing the beam velocity along the laboratory z -axis, and doing a relativistic transformation, the center-of-mass energy is obtained as

$$E_{\text{CM}} = \gamma_{\text{CM}} \cdot (E_{\text{LAB}} + M_{\alpha} - v_{\text{CM}} \cdot P_{\text{LAB}} \cdot \cos \theta_{\text{LAB}}), \quad (5.1)$$

where γ_{CM} is the relativistic Lorentz factor for the CM motion, M_{α} the α -particle mass, v_{CM} the center-of-mass velocity, θ_{LAB} the laboratory polar angle and $P_{\text{LAB}} = \sqrt{(E_{\text{LAB}} + M_{\alpha})^2 - M_{\alpha}^2}$ is the α -particle momentum measured in the laboratory.

Next the detection angles are transformed. They are necessary for calculating the momentum components in the CM system. The CM polar angle is calculated as

$$\theta_{\text{CM}} = \cos^{-1} \left(\frac{P_{z,\text{CM}}}{P_{\text{CM}}} \right), \quad (5.2)$$

where the z -component for the CM momentum is determined from the transformation

$$P_{z,\text{CM}} = \gamma (P_{\text{LAB}} \cdot \cos \theta_{\text{LAB}} - v_{\text{CM}} \cdot E_{\text{LAB}}), \quad (5.3)$$

while the total momentum in the CM frame P_{CM} is found as $\sqrt{(E_{\text{CM}} + M_{\alpha})^2 - M_{\alpha}^2}$. The azimuthal angle ϕ is left unchanged since the CM motion is along the z -axis.

5.2 ^{12}C analysis

Upon having applied the basic analysis steps to the $p + ^{11}\text{B}$ data, we now start doing analysis that is specific to the spectroscopic study of ^{12}C . The data are divided into two different sets. Both give full kinematical information: one for multiplicity-three events and one for multiplicity-two events.

5.2.1 multiplicity-three

For multiplicity-three events, which in this terminology can include three or more detections, we calculate the ^{12}C excitation energy by directly adding the α -particle

center-of-mass energies:

$$E_{\text{exc.}} = 7.275 \text{ MeV} + \sum_{i=1}^3 E_{\text{CM},i}, \quad (5.4)$$

where 7.275 MeV is the energy of the $3\text{-}\alpha$ threshold relative to the ground state in ^{12}C . When more than three particles are detected, the two particles of highest energy are chosen as two of our α -particles, while the third is chosen as the one of the remaining particles that best satisfies the cuts to be discussed below.

Cuts

Although the TDC cuts remove most of the random coincidences, additional cuts are necessary to reduce the background further. These will be discussed here.

First we exploit that the total momentum of the three particles, as measured in the center-of-mass system, is zero for genuine $3\text{-}\alpha$ events due to momentum conservation. Cuts are therefore made both on the total momentum and its components. Figure 5.6a shows a typical example of the total momentum distribution for a subset of the acquired data, while Figure 5.6b displays the distribution for the x -component of the total momentum. The cut levels that are applied to the data are shown as well. These requirements are equally applicable for triple α decays from the 16.11 MeV level and those that are γ -delayed. This is the case since the photon momentum ($\sim 1 \text{ keV}$ - see Section 3.3.1) is negligible compared to the spread in total momentum.

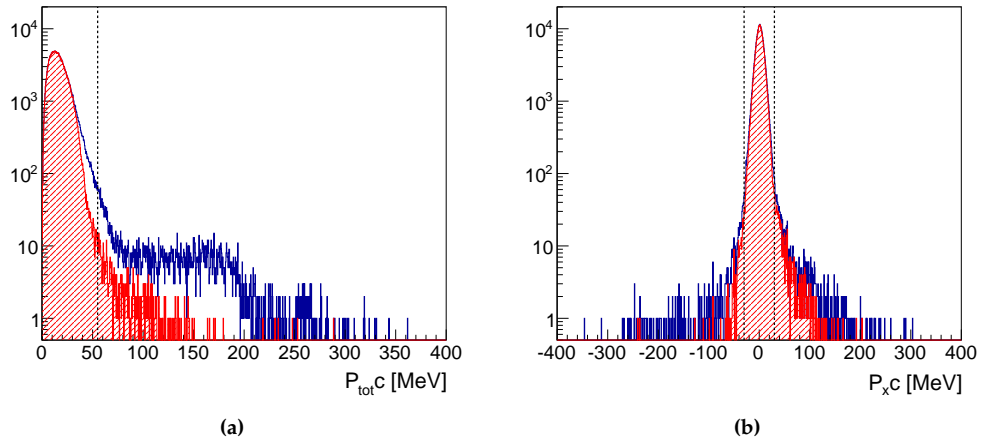


Figure 5.6: In blue: distributions for the total momentum (a) and the x -component of the total momentum (b) for all detections that survive the TDC cut. Red hatched histograms: additional requirements on the sum-angle and $\theta_{1,23}$.

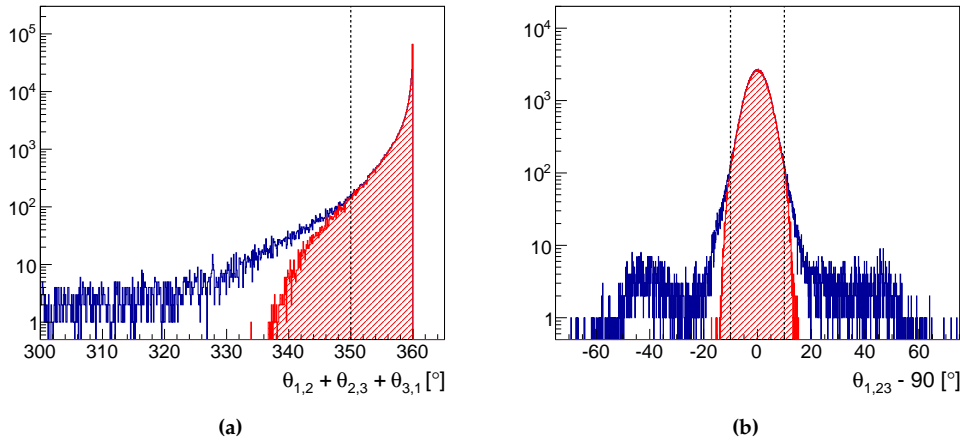


Figure 5.7: In blue: distributions for $\theta_{1,2} + \theta_{2,3} + \theta_{3,1}$ **(a)** and $\theta_{1,23}$ **(b)** for all detections that survive the TDC cut. Red hatched histograms: additional requirements on the total momentum and its components.

Next we impose two requirements of geometrical character that further reduce the number of random coincidences. Firstly, we require that the relative angles between the three particles ($\theta_{1,2}$, $\theta_{2,3}$ and $\theta_{3,1}$ - all in the center-of-mass frame) sum to 360° . Figure 5.7a shows how this sum is distributed for a subset of the acquired data. The dotted line in the figure represents the applied cut level. Secondly, the three α -particles must be emitted in the same plane. In order to quantify this we introduce the angle $\theta_{1,23}$, which is defined via

$$\mathbf{P}_1 \cdot (\mathbf{P}_2 \times \mathbf{P}_3) = P_1 \cdot P_2 \cdot P_3 \cdot \sin\theta_{23} \cdot \cos\theta_{1,23}, \quad (5.5)$$

where \mathbf{P}_1 is the momentum vector of the primary α -particle, \mathbf{P}_i ($i = 2, 3$) is the momentum vectors of the secondary α -particles and θ_{23} is the angle between the secondary α -particles. All quantities are in the center-of-mass reference frame, therefore $\theta_{1,23}$ measures to which degree the break-up occurs in one plane as required by momentum conservation. On Figure 5.7b the $\theta_{1,23}$ distribution is shown together with the applied cut level.

There is some degree of redundancy of the applied cuts to the momentum and angle distributions. Most events that survive the momentum cuts are expected to survive the angle cuts and vice versa. To what extent this is the case can be seen in Figures 5.6a and 5.6b where the hatched histograms show the momentum distributions when only applying angle cuts, while in Figures 5.7a and 5.7b the hatched histograms correspond to angle distributions when momentum cuts have been im-

posed. As an example Figure 5.6a shows that the angle cuts leave some events with a relatively high total momentum value.

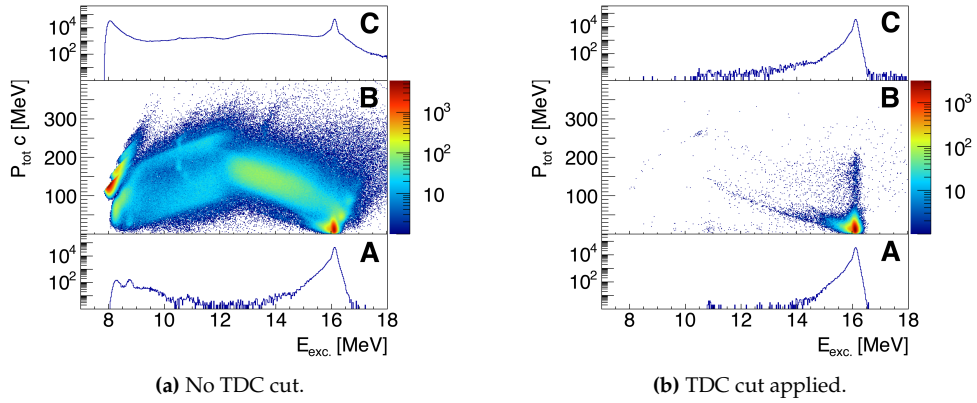


Figure 5.8: Total momentum plotted against the reconstructed excitation energy (panel B). Panel A shows the projection onto the energy axis when momentum and angle cuts are applied, while Panel C is the projection without these cuts. (a) No TDC cuts applied. (b): TDC cuts applied. The plots are based on a small subset of the acquired data.

The importance of momentum and angle cuts is illustrated in Figure 5.8 where the total momentum is plotted against the excitation energy (panel B). The plot is made for a small subset of the acquired data. Projections onto the excitation energy axis are shown for the two cases where momentum and angle cuts have been applied (panel A) and where no cuts have been applied (panel C). Figures 5.8a and 5.8b are with and without TDC cuts applied, respectively. Comparing the two figures it is evident that the TDC cut plays a crucial role in cleaning up the excitation energy spectrum. Panel A in Figure 5.8b shows that the combined effect of TDC cuts and momentum cuts is necessary to achieve sensitivity for γ -delayed events. For the data presented here, we already see hints of γ -events below 14 MeV. The spectrum accumulated over all acquired data is presented in Section 6.2 where it is also discussed how γ -decay events are unambiguously identified.

5.2.2 multiplicity-two

Complete kinematical information on the 3- α break-up can also be obtained for events where only two α -particles are detected. For events with two front-back matched energy signals, we assume that they originate from α -particles, and construct the energy of the unobserved third α -particle using momentum conservation. In terms of background reduction, the detection of two α -particles is not as strong a requirement as

requiring the detection of three α -particles. The background level is therefore higher in the excitation energy spectrum obtained from multiplicity-two data, preventing us from observing γ -decays in these data. The multiplicity-two data is however rich in information on the break-up of the 16.11 MeV level and will prove important in accessing regions of the phase space that multiplicity-three data is insensitive to. Experimental acceptances will be described in Section 6.1.2.

5.3 Decay channel

As one of the significant advantages of measuring the 3- α break-up of ^{12}C in complete kinematics, it allows us to determine the decay channel for each event. Since the two possible decay routes, either through the ^8Be ground state or the first excited state, are kinematically well separated (see e.g. the two plots in Figure 2.6 on page 27), we are able to distinguish between them by calculating the relative energy for all three combinations of α -particle pairs. By calculating the relative momentum \mathbf{P}_{23} , and assuming it to be between the ^8Be break-up α -particles, we get the ^8Be energy:

$$E_{^8\text{Be}} = \frac{\mathbf{P}_{23}^2}{4 \cdot M_\alpha}. \quad (5.6)$$

In case any of the three calculated values match the ^8Be ground state energy, the decay is identified as going through this state.

The relative energy of two secondary α -particles, when emitted from the ^8Be ground state, is 91.8 keV. The measured distributions for multiplicity-two and three events are shown in Figure 5.9. The distributions peak at the expected energy and are broadened considerably due to geometry uncertainties and the resolution of the detectors. The multiplicity-two distribution is wider than the multiplicity-three distribution, since multiplicity-two data is more sensitive to low-energy background signals. Also shown in Figure 5.9 are the cut-levels for identifying ground state decays which is set higher for the multiplicity-two data. The dotted lines around the cut levels are used for estimating the systematic error in our method, which is found to 1.5% for multiplicity-two data and 0.2% for multiplicity-three data.

Our ability to determine the decay channel allows an unambiguous identification of decay events originating from natural parity states. This follows from parity conservation which forbids the decay of unnatural parity states to the ^8Be ground state. This identification is a very useful tool for spectroscopy studies and is made possible by the complete kinematical detection.

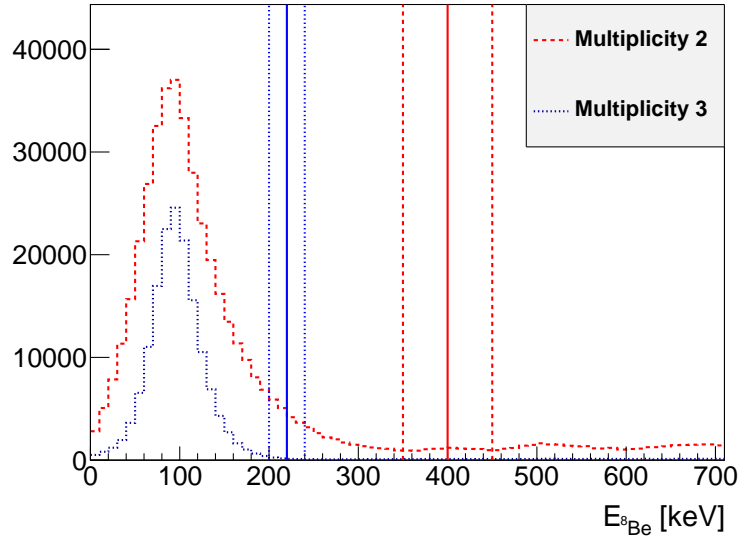


Figure 5.9: Relative energies (${}^8\text{Be}$ energies) for the three combinations of α -particle pairs. The spectra for multiplicity-two (red dashed line) and three (blue dotted line) data together with the cut-levels applied to identify the decay channel are shown.

5.4 Simulation

The experimental results obtained in this work, be it the number of observed gamma decays or the measured Dalitz plot distributions, cannot directly be compared to theoretical predictions. Accurate knowledge of the detection efficiencies for γ -delayed break-up events are for example necessary in order to calculate γ -decay branching ratios. Monte Carlo simulations are in this context essential. Through simulations we gain understanding of the experimental acceptances and the physics involved in the decay processes we study.

The simulation of the $p + {}^{11}\text{B}$ experiment is divided into three parts. The first part describes how the α decays are generated, either from the directly populated 16.11 MeV level or following a γ -decay. The second part deals with experimental effects and the last part concerns the analysis of simulated data. The simulation package used in this work is developed in our group by Oliver S. Kirsebom and is documented online [Sim].

5.4.1 Decay process

The initial excitation energy in ${}^{12}\text{C}$ is given by the specified proton beam energy and the decays are generally treated as being sequential. The initial state decays via an

intermediate resonance in ${}^8\text{Be}$ as two dynamically independent two-body break-up's. If the intermediate resonance is narrow ($\Gamma < 10$ keV) we assign a fixed excitation energy to it. When wider than 10 keV, the excitation energy is sampled from a Breit-Wigner function,

$$f(E) = \frac{P_{\text{entr.}}(E) \cdot P_{\text{exit}}(E)}{(E - E_0)^2 + (\Gamma/2)^2}, \quad (5.7)$$

where $P_{\text{entr.}}(E)$ and $P_{\text{exit}}(E)$ are the penetrabilities in the entrance and exit channels, respectively. For γ -decays of an initial state to an intermediate state the entrance penetrability is replaced by the appropriate phase-space factor, E_γ^{2L+1} .

When angular correlations are present, they are included in the simulation by specifying the relevant angular correlation function. The correlation function is derived from theory [Bie53] as shown in Section 2.1.2. The angular correlations will be different depending on the partial waves involved in the break-up. Comparing simulations with different partial waves to the measured energy distributions we gain insight into the break-up mechanism.

As discussed in Section 2.2.1, order-of-emission interference effects can play a significant role for intermediate resonances that are broad. These effects are taken into account by performing a separate simulation that assigns a weight w , given by the symmetrized amplitude in Eq. 2.16 in Section 2.2.1, to each simulated phase space decay. We apply the Von Neumann sampling method to the weighted events: an event is accepted if its weight is larger than rw_{max} , where r is a random number between 0 and 1 and w_{max} is the maximum weight. The energy distribution of the three α -particles acquired from this simulation serves as input for the overall simulation.

5.4.2 Experimental effects

Having simulated the decay process, which provides us with the momenta of the three α -particles, a correction for the experimental effects that the α -particles are subject to is needed. To mention a few, these effects include energy loss corrections and the response of the detection system.

We assume that the reactions occur uniformly throughout the target foil. Both the proton beam and the reaction products lose energy in the target foil, the foil backing and, if added, in coating layers on each side of the foil. The option of coating layers is used to take into account the temporal variations in foil thickness (see Section 4.4.5). The α -particles lose additional energy in the detector deadlayers before their deposited energies, in the active detector region, are stored as the detected energy. Energy losses are calculated by the same method as used in the analysis, i.e. by use of range tabulations from SRIM.

Regarding the detector response, the energy resolution of the DSSSD detectors is described by a Gaussian, and the effects of summing, i.e. particles hitting the same strip, and sharing, i.e. particles hitting inter-strip regions, are included. We also implement detection thresholds which mimic the ADC and trigger thresholds in the experiment. For a full description of all the included effects see [Sim].

Simulations are particularly helpful for estimating systematic errors concerning uncertainties in the experimental setup. This is done by varying parameters describing the setup by their estimated uncertainty, and then performing simulations with these adjusted values.

5.4.3 Analysis of the simulated data

The third and final step in the simulation procedure involves the analysis of the simulated data. The idea is to use the same analysis as used on measured data. For this the simulated data is stored in the same ROOT [Bru97] TTree structure as the measured data.

Differences in the analysis of the measured and simulated data exists. First of all, since the energy signals in the simulation corresponds to the incoming energy of a particle when it reaches the active detector region, no calibration of the simulated data is done nor do we correct for non-ionizing energy losses. Secondly, since sub-threshold energy signals are excluded in the analysis of measured data, we need to require a similar cutoff when analyzing simulated data. We approximate the behavior of the trigger threshold by excluding all simulated particle energies that fall below the measured trigger threshold in the given channel.

Results and discussion

The results obtained from the $p + {}^{11}\text{B}$ experiment are presented and discussed in this chapter. The chapter is divided into two overall sections, one concerning the break-up of the 16.11 MeV state (Section 6.1), and one concerning the observation of γ -transitions (Section 6.2).

6.1 Break-up of the 16.11 MeV state

As already noted in Section 3.2, the $p + {}^{11}\text{B}$ experiment is partly motivated by achieving a detailed understanding of the decay mechanism involved in the $3\text{-}\alpha$ break-up of the 2^+ resonance at 16.11 MeV in ${}^{12}\text{C}$. Our compact detection setup provides good sensitivity throughout the $3\text{-}\alpha$ phase space allowing us to utilize the Dalitz plot technique from which information on the break-up mechanism is extracted. Besides from the direct physical interest in a good description of the 16.11 MeV break-up, this description is also needed for the purpose of normalization. The α -width of the 16.11 MeV resonance is used to achieve absolute normalization of our γ -decay branches. It is therefore worthwhile to perform a careful study of the 16.11 MeV break-up, providing us with the foundation for achieving accurate γ -transition strengths.

6.1.1 Measured energy distributions

This section presents the measured spectra for various energy distributions and significant features are commented on. First the single particle energy spectra are presented after which the two-dimensional Dalitz plot are discussed.

Single particle energy spectra

Figure 6.1 shows the single α -particle energy spectrum measured in detector 1. The spectrum is created from data set number 9. The filled histogram represents the coincidence spectrum where at least one detection in each detector is required. The overall structures in the spectrum can be explained from kinematical consideration (see Section 2.1.1). The distinct peak around 6 MeV originates from primary α_0 -particles,

which are expected to be sharply distributed at 5.89 MeV. The broad distribution, extending over several MeV and peaking near 4 MeV, is formed by primary and secondary α -particles emitted in the ${}^8\text{Be}(\text{exc})$ decay channel. The raised structure on the low energy flank between 1 MeV and 2 MeV is the signature of secondary α -particles emitted in the ground state channel. These interpretations, regarding the broad distribution, follow from Figure 2.3a in Section 2.1.1. The more detailed shape of the distribution is harder to understand intuitively. It involves knowledge of the ${}^8\text{Be}(\text{exc})$ resonance profile, possible dynamical correlations and symmetrization of the decay amplitude. These effects will be simulated for the α_1 break-up channel as described in Section 6.1.3.

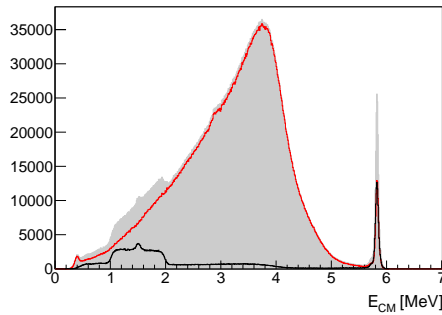


Figure 6.1: α -particle energy spectrum measured in detector 1 for data set number 9. The filled spectrum is the total coincidence spectrum. The red spectrum is obtained by requiring exactly one detection in each detector, while the black spectrum has been obtained when requiring at least three detections.

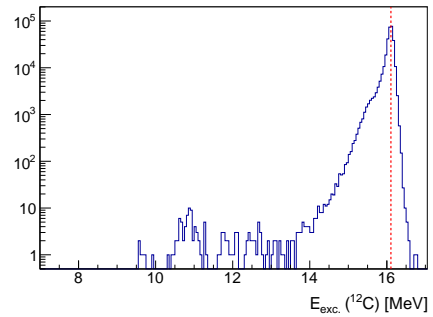


Figure 6.2: Reconstructed excitation energy spectrum for multiplicity-three events for data set number 9. All cuts have been applied in this plot. The dotted red line illustrates the known excitation energy of the 2^+ resonance.

The α_0 break-up channel is easier to describe in the sequential picture due to the narrow width of the ${}^8\text{Be}$ ground state, validating the assumption of dynamical independence between the $[{}^{12}\text{C} \rightarrow \alpha + {}^8\text{Be}]$ and $[{}^8\text{Be} \rightarrow \alpha + \alpha]$ break-up's. In addition, only one possible combination for the involved angular momenta, namely $[l_1 = 2 \wedge l_2 = 0]$, is possible and no angular correlations arise assuming an unpolarized initial state. The fact that the α_0 channel is more easily described makes it less rich in information compared to the α_1 channel. The difficulty in describing the latter channel constitutes at the same time the possibility of acquiring interesting physical information regarding the break-up.

The coincidence spectrum is divided into two spectra in Figure 6.1. One of them describes double coincidences (red line) while the second spectrum describes triple

coincidences (black curve). These spectra illustrate an important aspect of our setup. Requiring at least three detections will drastically lower the ability to detect break-up's that proceed through ${}^8\text{Be}(\text{exc})$. That is clear since the broad distribution is almost fully absent in the multiplicity-3 spectrum or put in a different way: the multiplicity-two spectrum nearly exhaust the total coincidence spectrum. This behavior is basically explained by the large difference in the energies available in second break-up for the two channels. As shown quantitatively in Figures 2.3b, 2.4a and 2.4b in Section 2.1.1 the measured angle between the two secondary α -particles is quite large for the ${}^8\text{Be}(\text{exc})$ channel whereas it is much smaller for the ground state channel. This explains the difference between the two spectra since the efficiency for detecting all three α -particles will decrease as the break-up angle increases.

Two minor structures of artificial character are also worth noting in Figure 6.1. The first is seen in the multiplicity-3 spectrum showing a small peak located at 1.5 MeV, exactly in the middle of the distribution caused by the secondary α -particles emitted in the ${}^8\text{Be}(\text{gs})$ channel. It occurs when two α -particles are detected in the same detector and the front(back) energy of one particle is paired with the back(front) energy of the second particle in the front-back matching routine. The assigned energy of each pair is then placed in the middle of the distribution since the detected energy is taken as the average of the front and back signals. The probability for this increases with increasing tolerance level in the front-back matching. This tolerance level could in the present case have been set more tightly (see Figure 5.4 in Section 5.1.3), but no significant error is introduced due to this effect. The effect is understandably not visible in the multiplicity-two spectrum since, as already pointed out, the efficiency for detection both secondary α -particles is low in the ${}^8\text{Be}(\text{exc})$ channel. The second structure to be noted is the small increase in the multiplicity-two spectrum just below 3 MeV. It originates from detections of all three α -particles in the ${}^8\text{Be}(\text{gs})$ channel, but where the summing of the secondary α -particles is interpreted as sharing. This happens when two particles hit the same front(back) strip and neighbouring back(front) strips, in which case the signals are assumed to originate from one particle. By judging from the calculated break-up angles (see Figure 2.4a in Section 2.1.1) ($0 - 20^\circ$) and the typical angular coverage of two strips, which maximally is $\sim 7^\circ$, we expect to observe this artificial effect in the multiplicity-two spectrum.

Excitation energy spectrum

The reconstructed ${}^{12}\text{C}$ excitation energy spectrum is shown in Figure 6.2 for the same data as used in Figure 6.1. The decay of the 16.11 MeV state clearly dominates the spectrum but at lower excitation energy the signature of γ -delayed events is seen. In particular there seems to be evidence for γ -decays to the 1^- state at 10.8 MeV. In Section 6.2 the combined spectrum of all the acquired data will be presented.

Dalitz plots

The Dalitz plots obtained for multiplicity-two and three events are presented in Figure 6.3. In accordance with the observations made from the single α -particle energy spectrum, it is clearly seen that the multiplicity-three Dalitz plot is insensitive to break-up's proceeding through the ${}^8\text{Be}(\text{exc})$ channel. Events from this break-up channel should be located more centrally than the ground state bands (see Section 2.1.3). The ground state bands are clearly seen in the top and bottom left and right corners. On the other hand, the multiplicity-two Dalitz plot display a large amount of intensity in the central Dalitz plot region. Notice that the the central region consist of a triangular distribution instead of the band structure as naively pictured in Figure 2.6 in Section 2.1.3. As will be shown in Section 6.1.3 we understand this as constructive interference in the center of the Dalitz plot.

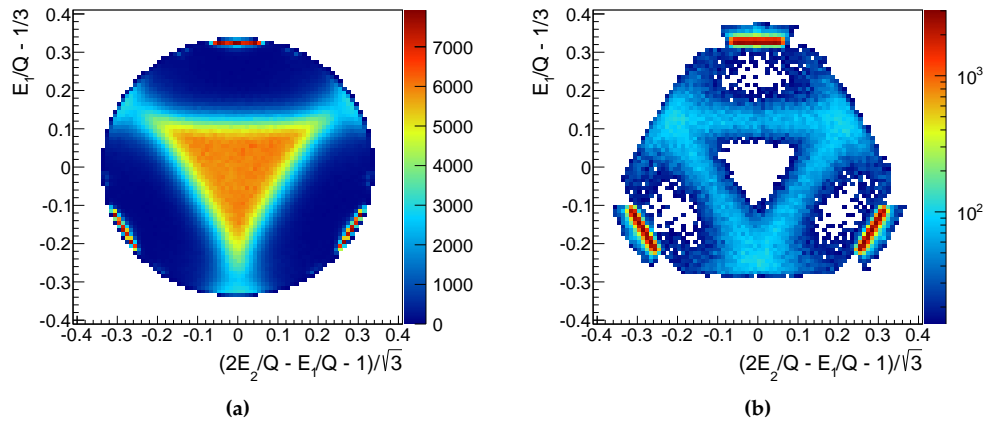


Figure 6.3: Dalitz plot distribution for data set 9. In (a) the distribution is plotted for multiplicity-two events and in (b) it is plotted for multiplicity-three events.

6.1.2 Acceptances

Our sensitivity to the different break-up channels for the two different data sets have been discussed qualitatively above. In order to clearly disentangle the observed structures in the Dalitz plots from experimental effects we investigate how the multiplicity-two and three sensitivities vary across the Dalitz plot. A pure $3\text{-}\alpha$ phase space decay is simulated and Figure 6.4b shows the expected uniform Dalitz plot distribution when no experimental effects are taken into account. Analyzing, i.e. taking experimental effects into account, the phase space events gives the distributions shown in Figures 6.4a and 6.4c for multiplicity-two and three requirements,

respectively. These plots clearly show which regions of the Dalitz plot that our detection setup provides sensitivity in. The sensitivity is highest at the rim of the Dalitz plot, corresponding to back-to-back break-up's. While the acceptance in the central region is non-vanishing for multiplicity-two events it is zero for multiplicity-three events. Figure 6.4c shows us that for detections of all three α -particles we are practically only sensitive to break-ups where one particle gets the maximal allowed energy (defined by the momentum conservation circle in the Dalitz plot) resulting in a low break-up angle between the secondary particle.

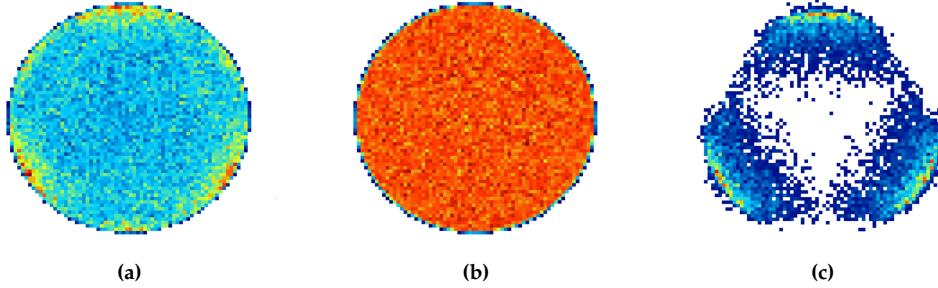


Figure 6.4: Dalitz plot distributions for a pure phase space simulation of the $3\text{-}\alpha$ break-up. The unmodified distribution, i.e. without taking experimental effects into account, is shown in (b). In (a) the phase space distribution resulting from a multiplicity-two analysis is shown, while (c) shows the corresponding distribution resulting from a multiplicity-three analysis. The non-vanishing regions in (a) and (c) marks the regions of the $3\text{-}\alpha$ phase space that the detection setup provides sensitivity in.

6.1.3 Simulation of break-up models

Having presented the measured energy distributions resulting from the $3\text{-}\alpha$ break-up we now seek a deeper understanding of the break-up mechanism for the 16.11 MeV level. The α_0 break-up channel is not as complicated and rich in information as the α_1 channel. We therefore focus our effort on the latter channel, where we, as mentioned previously, mainly have two goals: One is to test whether the break-up is best described with $l_1 = 2$, with l_1 being the orbital angular momentum between the primary α -particle and the ${}^8\text{Be}$ recoil. Secondly, we want to test the importance of interference effects in the break-up.

Six different models for the ${}^8\text{Be}(\text{exc})$ break-up are compared to the measured data, both in the form of single α -particle energy spectra and Dalitz distributions. The models used are listed in Table 6.1. Model 1 is the simplest model. This model does not take symmetrization in the final state amplitude into account and is therefore

unable to describe interference structures. It uses $l_1 = 2$ and employ the angular correlation function specified in Eq. 2.9 (Section 2.1.2). Model 2 assumes a democratic break-up as described in Section 2.1. The democratic break-up amplitude is calculated by using $K = 2$, which is the lowest possible value for a 2^+ state. The third model calculates the symmetrized decay amplitude from Eq. 2.16 (Section 2.2.1) with $l_1 = 2$. Models 4, 5 and 6 also use the symmetrized amplitude in Eq. 2.16 but in a modified version where extra barrier penetrabilities for each of the two secondary α -particles are introduced. As explained in Section 2.2.1 this is a crude way of correction for the electromagnetic interaction between the primary α -particle and the secondary α -particles. The interaction distance is chosen to $R = 5$ fm with a relative angular momentum $L = 2$. Model 4 uses $l_1 = 0$, model 5 uses $l_1 = 2$ and model 6 uses $l_1 = 4$.

Table 6.1: Definition of the models that are compared to data. See the text for definitions of the listed quantities.

Model	Seq./Demo.	Symmetrization	l_1	R	L
1	Seq.	no	2	-	-
2	Demo.	yes	2	-	-
3	Seq.	yes	2	-	-
4	Seq.	yes	0	5	2
5	Seq.	yes	2	5	2
6	Seq.	yes	4	5	2

Comparison to single α -particle spectra

First, the simulated single α -particle energy spectra are compared to the measured ones. The spectra are plotted when requiring coincidence events. The comparison is done at a qualitative level in Figures 6.5 and 6.6, where simulated spectra based on models 1-6 are compared to the corresponding spectra measured in detector 2. The obtained results are similar for detector 1. Figure 6.5 shows the spectra obtained from models 1, 2, 3 and 5 with the simulated ${}^8\text{Be}(\text{gs})$ spectrum added to them. The simulated spectra are normalized to the measured spectrum. Models 1, 3 and 5 all reproduce the gross structures while model 2, based on the democratic model, fails completely in describing the measured spectrum. The simple model 2, only including angular correlations, overestimates the high energy side of the spectrum. This part of the spectrum is reproduced better with models 3 and 5, indicating significant interference. Model 5 gives a slightly better description compared to model 3 underlining the presence of dynamical correlations between the [${}^{12}\text{C} \rightarrow \alpha + {}^8\text{Be}$] and

[${}^8\text{Be} \rightarrow \alpha + \alpha$] break-up's.

Figure 6.6 shows the obtained spectra from simulations based on models 4, 5 and 6, which use $l_1 = 0, 2, 4$, respectively. Again, model 5 gives the best description of the measured data, while models 4 and 6 overestimate the high energy side significantly. Our data therefore clearly supports the assignment of $l_1 = 2$ in the decay of the 16.11 MeV state.

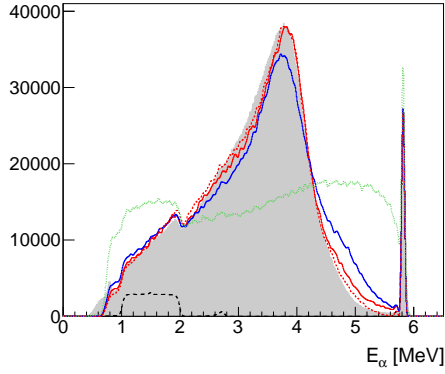


Figure 6.5: Coincidence single α -particle energy spectrum measured in detector 2 (grey filled histogram). Simulated spectra: model 1 (blue solid line), model 2 (green solid line), model 3 (red solid line) and model 5 (red dashed line). The ${}^8\text{Be}(\text{gs})$ channel is represented by the long dashed black line and is added to the ${}^8\text{Be}(\text{exc})$ spectra.

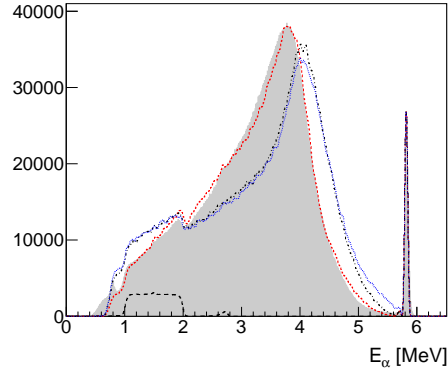


Figure 6.6: Coincidence single α -particle energy spectrum measured in detector 2 (grey filled histogram). Simulated spectra: model 4 (black dotted-dashed line), model 5 (red dashed line) and model 6 (blue dotted line). The ${}^8\text{Be}(\text{gs})$ channel is represented by the long dashed black line and is added to the ${}^8\text{Be}(\text{exc})$ spectra.

As already pointed out, break-up's proceeding through the first excited state in ${}^8\text{Be}$ are very difficult to observe in triple coincidences. We do however observe some of these events, as barely seen in Figure 6.1, and by comparing to the simulated multiplicity-three data we achieve a more sensitive test of the break-up mechanism. In Figures 6.7 and 6.8 the triple coincidence single particle energy spectrum is compared to models 1-6. The measured spectrum consists mainly of ${}^8\text{Be}(\text{gs})$ events, but the small amount of events in the region 2-5.5 MeV are from the ${}^8\text{Be}(\text{exc})$ channel. Our conclusions regarding how well the different models describe the measured data is generally the same as for the coincidence two spectra. Model 5 gives again the best description, reproducing the plateau at ~ 2 -3.2 MeV and the broad peak at ~ 4 MeV, but with significant deviations, in particular just below the α_0 peak where the model underestimates the measured intensity. Model 3 lies somewhat closer to the measured intensity in this region, telling us that the extra coulomb repulsion in-

cluded in model 5 not necessarily gives the best description of the physics involved in the break-up process. This is expected since the coulomb modification in model 5 is based on crude assumptions. It is clear from Figure 6.8 that also the triple coincidence spectrum supports the $l_1 = 2$ assignment.

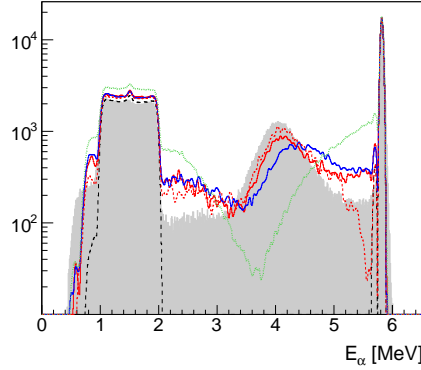


Figure 6.7: Triple coincidence single α -particle energy spectrum measured in detector 2 (grey filled histogram). Simulated spectra: model 1 (blue solid line), model 2 (green solid line), model 3 (red solid line) and model 5 (red dashed line). The ${}^8\text{Be}(\text{gs})$ channel is represented by the long dashed black line and is added to the ${}^8\text{Be}(\text{exc})$ spectra.

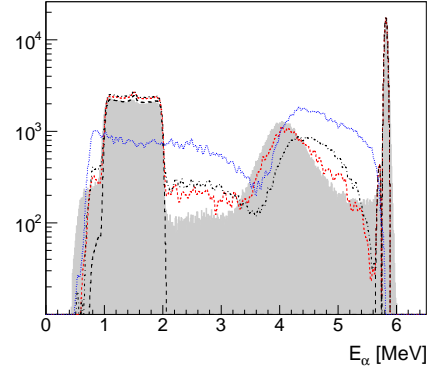


Figure 6.8: Triple coincidence single α -particle energy spectrum measured in detector 2 (grey filled histogram). Simulated spectra: model 4 (black dotted-dashed line), model 5 (red dashed line) and model 6 (blue dotted line). The ${}^8\text{Be}(\text{gs})$ channel is represented by the long dashed black line and is added to the ${}^8\text{Be}(\text{exc})$ spectra.

Comparison to Dalitz plot distributions

The Dalitz plot is an indispensable tool for studying the break-up of ${}^{12}\text{C}$ resonances. As discussed in Section 2.1.3, each point in the Dalitz plot provide complete kinematical information and structures in the plot are due to symmetry constraints and final state interactions. The Dalitz plot is therefore richer in information on the break-up compared to the single particle spectra. The simulated Dalitz plots based on models 1, 2, 4 and 5 are shown in Figure 6.9. They all show different structures. Comparing the distributions in Figure 6.9c and 6.9d, which are with $l_1 = 0$ and $l_1 = 2$ respectively (model 4 and 5), we note a large difference in central intensity. The α -particles are therefore more likely to share the available energy equally when $l_1 = 2$ which is caused by the centrifugal barrier lowering the penetrability of the first emitted α -particle. Comparing the two models with $l_1 = 2$ (model 1 and 5) with Dalitz distributions shown in Figures 6.9a and 6.9b, we observe that model 1 produces an intensity

minimum in the central region which is not produced by model 5. This is a clear signature of constructive interference between the Dalitz plot bands which is further supported by the rapid decrease in intensity at the edge of the triangular distribution (Figure 6.9d) indicating destructive interference.

The simulated distributions are now compared to the multiplicity-two plot in Figure 6.3. Since two-dimensional plots are ill-suited for visual comparison to theoretical models we construct three one-dimensional projections for this purpose. The projections are described in terms of the coordinates ρ , ξ and η as introduced in Section 2.1.3.

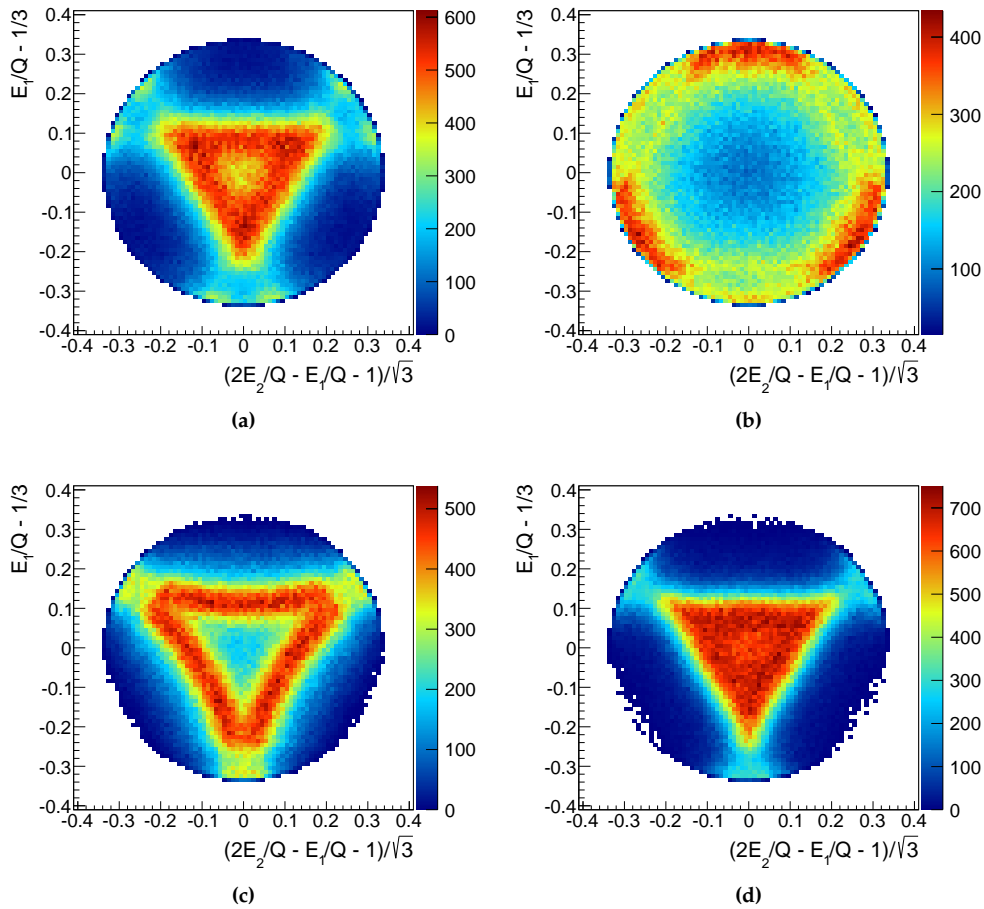


Figure 6.9: Simulated Dalitz plot distributions for the ${}^8\text{Be}(\text{exc})$ channel. The simulations are based on model 1 (a), model 2 (b), model 4 (c) and model 5 (d).

The projected data is shown in Figure 6.10 where comparisons to models 2, 3, 4

and 5 are made. The simulated spectra are fitted to the measured spectrum. The democratic model (green curves) fails to reproduce the gross structures in any of the three projections, while model 4 ($l_1 = 0$) does a better job, but still with large deviations. Models 3 and 5 makes the best comparisons to the measured spectra. In Figures 6.10a and 6.10b, model 5, the symmetrized model including the Coulomb modification, gives a slightly better fit, while it seems to be opposite for Figure 6.10c. For both models there are systematic deviations from the measurement, in particular near 0 and 1 on the abscissae, but the overall agreement is good.

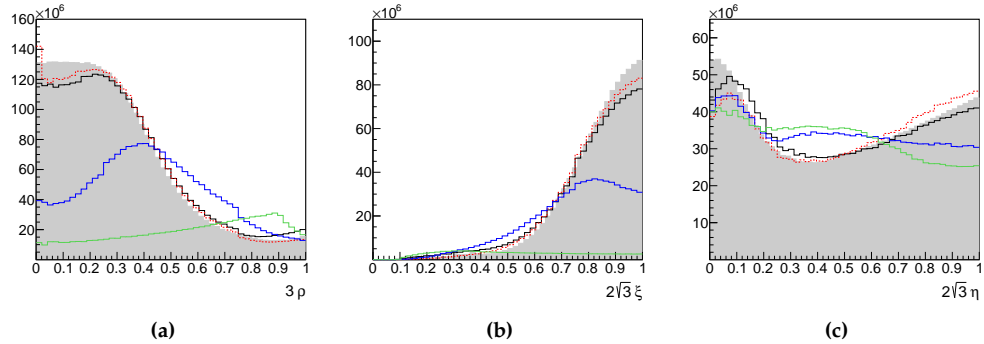


Figure 6.10: Dalitz plot projections as defined in Section 2.1.3. The projected coordinates are 3ρ (a), $2\sqrt{3}\xi$ (b) and $2\sqrt{3}\eta$ (c). The grey filled histograms are the measured distributions. The simulated data is based on model 2 (green solid line), model 3 (black solid line), model 4 (blue solid line) and model 5 (red dotted line).

Based on comparisons to single particle energy spectra and Dalitz plots we have seen that model 5 gives the best description of the measured data. Detection efficiencies for the ${}^8\text{Be}(\text{exc})$ break-up of the 16.11 MeV state is therefore calculated using this model.

6.1.4 Efficiencies

The results obtained on the γ -decay of the 16.11 MeV state will be presented in the next section. Absolute normalization for the measured γ -branches is achieved by using the known α -width of the 16.11 MeV. This method of normalization requires the detection efficiencies for the two break-up channels of the 16.11 MeV to be determined. The detection efficiencies needed are those for multiplicity-three events, since we only observe γ -transitions in multiplicity-three data.

By simulating N_{sim} break-up events and counting the number of detected 3α decays in a given decay channel $N_{\text{obs, sim}}^{\text{gs/exc}}$, the detection efficiency $\varepsilon_{\text{gs/exc}}$ is determined

as the ratio

$$\varepsilon_{\text{gs/exc}} = \frac{N_{\text{obs,sim}}^{\text{gs/exc}}}{N_{\text{sim}}}. \quad (6.1)$$

Alternatively, and as a consistency check, the efficiency can be inferred by looking at the single α -particle energy spectrum. The number of counts in the spectrum and the number of simulations needed to reproduce the measured spectrum gives the efficiency. This method gives a visual impression on how well the simulated model describes the measured data (as discussed above), and provides, together with the literature value for the ${}^8\text{Be}(\text{gs})$ branching ratio, a guideline in the procedure for obtaining accurate efficiencies. The ${}^8\text{Be}(\text{gs})$ branching ratio is taken from [Alc12] ($\frac{\Gamma_{\alpha_0}}{\Gamma_{\text{tot}}} = 5.8(9)\%$). The branching ratio is calculated as

$$\frac{\Gamma_{\alpha_0}}{\Gamma_{\alpha,\text{tot}}} = \frac{\frac{N_{\text{obs}}^{\text{gs}}}{\varepsilon_{\text{gs}}}}{\frac{N_{\text{obs}}^{\text{gs}}}{\varepsilon_{\text{gs}}} + \frac{N_{\text{obs}}^{\text{exc}}}{\varepsilon_{\text{exc}}}}. \quad (6.2)$$

Table 6.2: Branching ratios for the ${}^8\text{Be}(\text{gs})$ break-up channel as measured on basis of multiplicity-two and three data. Efficiencies for detecting ${}^8\text{Be}(\text{gs})$ and ${}^8\text{Be}(\text{exc})$ break-up's are listed for both multiplicities. For the branching ratios the first parenthesis gives the statistical error while the second parenthesis gives the systematic error. The error on the efficiencies are the total error.

Data set	Multip. 3			Multip. 2		
	ε_{gs}	$\varepsilon_{\text{exc.}} \times 10^3$	B.R. _{gs}	ε_{gs}	$\varepsilon_{\text{exc.}}$	B.R. _{gs}
1	0.114(5)	3.9(7)	5.7(0.06)(1.0)	0.256(12)	0.21(2)	5.2(0.012)(6)
2	0.112(8)	3.4(6)	4.1(0.05)(8)	0.256(7)	0.21(2)	5.3(0.015)(5)
3	0.103(5)	1.7(3)	6.3(0.1)(1.1)	0.232(12)	0.171(17)	5.1(0.015)(6)
4	0.091(4)	2.5(5)	6.5(0.08)(1.1)	0.231(15)	0.178(17)	5.2(0.013)(6)
5	0.093(5)	3.3(8)	6.9(0.08)(1.5)	0.241(12)	0.19(2)	5.13(0.02)(6)
6	0.140(11)	3.9(8)	7.10(0.07)(1.5)	0.290(10)	0.270(2)	5.4(0.013)(5)
7	0.141(15)	4.7(1.0)	4.4(0.04)(1.0)	0.295(14)	0.28(3)	5.0(0.013)(5)
8	0.142(10)	8.0(1.0)	5.4(0.05)(1.0)	0.297(8)	0.29(3)	4.7(0.02)(4)
9	0.143(9)	6.2(8)	6.3(0.05)(0.9)	0.298(13)	0.288(12)	5.3(0.011)(3)
10	0.149(9)	6.1(7)	4.9(0.04)(6)	0.298(11)	0.289(17)	5.1(0.01)(3)

The obtained efficiencies and ground state branching ratios for multiplicity-two and three data are listed in Table 6.2 for the 10 data sets. For each listed efficiency N_{sim} is 3×10^6 . Although not interesting on its own, the multiplicity-two values are included as a consistency check of the multiplicity-three values. The average branching ratios are determined to 5.1(0.5) and 5.4(1.1) for the multiplicity-two and three

data sets, respectively. Our values are consistent among each other and with the literature value (5.8(9)%) providing us with confidence that our efficiency calculations are correct. The errors on the efficiencies are dominated by systematic errors and since the number of $3\text{-}\alpha$ detections are of the order 10^5 for the multiplicity-3 data sets and of the order 10^6 for multiplicity-two data sets, the total error on the branching ratios are also dominated by systematic effects. This is seen in Table 6.2 where the two parentheses after the branching ratio values denote the statistical and systematic errors. The relatively large errors on the extracted multiplicity-three branching ratios are mainly due to the large error on the $3\text{-}\alpha$ detection efficiency in the ${}^8\text{Be}(\text{exc})$ channel. Small uncertainties in the detection geometry induce a large error on the ${}^8\text{Be}(\text{exc})$ efficiency since our setup is just barely capable of detecting both secondary α -particles emitted in this channel (this is exemplified in Figure 2.3b in Section 2.1.1 where the break-up angle is seen to be very large in the laboratory system).

6.1.5 Summary and discussion: $3\text{-}\alpha$ break-up of the 16.11 MeV state

The decay of the 16.11 MeV state, proceeding through the first excited state in ${}^8\text{Be}$, has been measured providing the best description of the break-up mechanism to date. Comparisons of measured one- and two-dimensional energy spectra to simulated models show that the break-up is described excellently using a sequential model (model 5) that symmetrize the final state amplitude. Compared to a sequential model that only include angular correlations (model 1) the important role of symmetrization is underlined due to the presence of interference. Including extra barrier penetrabilities in the decay amplitude, as a rough way of correcting for dynamical correlations between the [${}^{12}\text{C} \rightarrow \alpha + {}^8\text{Be}$] and [${}^8\text{Be} \rightarrow \alpha + \alpha$] break-up's, give a slightly better fit to the measured data than if these extra penetrabilities were not included. This indicates the short coming of the assumption of dynamical independence in the sequential break-up picture.

At the other extreme, a democratic decay model was compared to the measured data. This model gives a very poor description of the data in all cases and is therefore not responsible for the break-up mechanism. This conclusion stands in contrast to the work in [Deh65], where a sequential break-up description is rejected based on the nearly constant intensity in the central region of the Dalitz plot. Not realizing that this structure of the Dalitz plot results from interference, the break-up mechanism was interpreted as democratic.

A more precise description of the measured data can possibly be achieved using a full three-body calculation that treats ${}^{12}\text{C}$ as a $3\text{-}\alpha$ cluster system at all distances. This has successfully been done for the 1^+ state at 12.71 MeV and the 4^- state at 13.35 MeV [Kir10] using the three-body calculations published in [AR08]. Such calculations for a 2^+ state are currently not available at 16.11 MeV.

The orbital angular momentum between the first emitted α -particle and the ${}^8\text{Be}$ recoil (l_1) is constrained by selection rules to 0, 2 or 4. As a first guess one would assume the $l_1 = 0$ channel to dominate since it does not involve a centrifugal barrier. But as shown in Figures 6.6 and 6.8 our data is clearly best described by $l_1 = 2$, confirming the findings of [Que69] and [Hud72]. This property might be reflected in the structure of the unknown ($j^\pi = 2^+, T = 0$) strength which isospin-mixes with the 16.11 MeV ($j^\pi = 2^+, T = 1$) state.

6.2 γ -decays

Turning to the results of our search for γ -decays from the 16.11 MeV level we start out by focussing on Figure 6.11. The figure consists of two panels that share the same abscissa. The lower panel shows the ${}^{12}\text{C}$ excitation energy spectrum up to 14.5 MeV for all acquired data. The top panel display how the three α -particle energies are distributed as function of excitation energy. The one-dimensional energy spectrum contains three distinct peaks positioned quite accurately at the energies of the known 3^- ($E = 9.64 \text{ MeV}, \Gamma = 48(2) \text{ keV}$ [Kok13]), 1^- ($E = 10.85 \text{ MeV}, \Gamma = 272(5) \text{ keV}$ [Alc12]) and 1^+ ($E = 12.71 \text{ MeV}, \Gamma = 18(5) \times 10^{-3} \text{ keV}$ [AS90]) levels. Transitions to the 3^- and 1^+ levels were seen in the latest γ -decay study of the 16.11 MeV state [Ade77] (see Table 3.3) whereas transitions to the 1^- level have not been reported before.

The different histogram shadings in the excitation energy spectrum represent decays identified as going through the ${}^8\text{Be}$ ground state (blue shaded) and first excited state (solid red). The 1^+ state stands out clearly as decaying through the first excited state, which is expected since ground state decays are forbidden for unnatural parity states due to parity conservation. The decay channel for each events is achieved as described in Section 5.3, but is also visually obtainable from the top panel in Figure 6.11. The diagonal structure extending from the top right corner follow the linear relation

$$E_\alpha = \frac{2}{3} (E_{\text{exc.}} - E_{{}^8\text{Be}(\text{gs})}), \quad (6.3)$$

which is the expected energy of a primary α -particle decaying through ${}^8\text{Be}(\text{gs})$. Thus the diagonal structure represents ${}^8\text{Be}(\text{gs})$ decays. This two dimensional visualization of the $3\text{-}\alpha$ events serves most importantly as a confirmation of the observed γ events. Take for example the distribution of events between the 1^- and 1^+ state. Judging from the excitation energy spectrum in the lower panel of Figure 6.11 it is hard to tell whether it originates from genuine γ events or from background. But if we at the same time compare to the two-dimensional spectrum in the top panel, it is clear that this region is essentially background free since most events have an associated single α -particle energy on the diagonal. This quality is obviously critical for our

objective and it leaves us with the interesting problem of interpreting these events, which must originate from γ decays to natural parity states. Hints of a natural parity state is also visible around 10.0 MeV. The interpretation of this natural parity strength is discussed later.

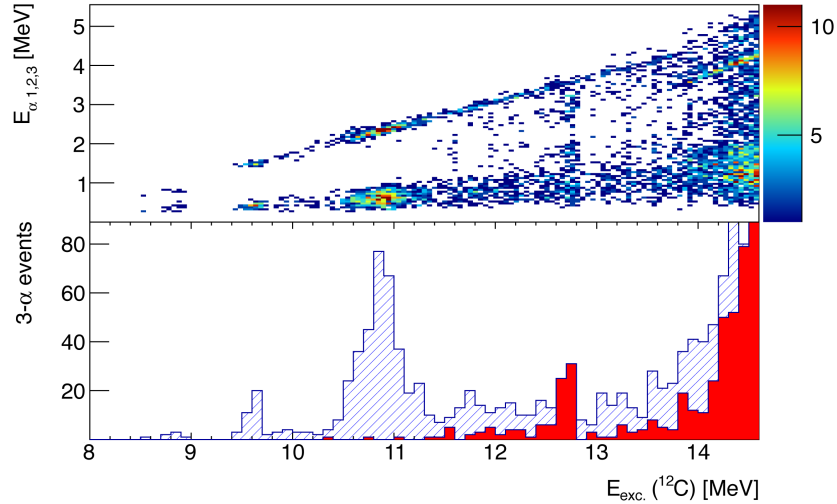


Figure 6.11: Lower plot: excitation energy spectrum for all coincidence three data. The blue hatched histogram represents 3- α decays proceeding through the ground state in ^8Be , while the red histogram represents those going via the first excited state in ^8Be . Top plot: for each 3- α decay event the energies of all three α -particles are plotted. The diagonal structure represents ^8Be ground state decays.

Decays to unnatural parity states have the distinct vertical line signature in the two-dimensional plot in Figure 6.11. This is clearly visible for the 1^+ state, but indications of extra unnatural parity structure is also visible around 11.6 MeV, 12.0 MeV, 13.2 MeV and 13.6 MeV.

6.2.1 Efficiency calculations

Bringing the discussion of the observed γ -transitions to a quantitative level we need to perform efficiency simulations for the transitions mentioned above. Doing this enables us to calculate the observed transition widths and corresponding reduced matrix elements which in case of the 3^- and 1^+ levels can be compared to the results obtained by [Ade77].

The efficiencies for the γ -delayed events are simulated using the same program as used for simulating the 3- α break-up of the 16.11 MeV level. The simulations are, for

the sake of clarity, divided into five groups. The first three groups deal with the 1^+ , 1^- and 3^- levels that are clearly seen in the data. Groups four and five include the natural parity distributions in the 11.5-13.0 MeV and 10.0 MeV regions, respectively. The five groups are listed in Table 6.3 showing the basic physics assumptions entering the simulations.

Table 6.3: The five different groups that simulation are carried out for. Group 4 is divided into 6 intervals, 250 keV wide each. The simulations in groups 4 and 5 are divided into two sub-groups assuming M1 and E1 decays to 2^+ and 3^- states, respectively. Individual simulations are performed for all the 10 data sets.

Group	Decay group	^8Be break-up ch [gs/exc]	E/ML	l_1	l_2
1	1^+	exc	M1	2	2
2	1^-	gs	E1	1	0
3	3^-	gs	E1	3	0
4	11.5-13.0 MeV (2^+ , 3^-)	gs	M1,E1	2	0
5	9.8-10.25 MeV (2^+ , 3^-)	gs	M1,E1	2	0

For the 1^+ state we assume a sequential break-up proceeding through the first excited state of ^8Be . The break-up is described by the symmetrized amplitude in Eq. 2.16, which, as previously noted in Section 2.2.1, has been shown to give the best description of the break-up. We use the modified version of Eq. 2.16 approximating the $\alpha+^8\text{Be}$ Coulomb interaction in the second break-up. When calculating the extra barrier penetrabilities we use $R = 10$ fm and $L = 2$, which gave the best description of the 1^+ decay in [Fyn03]. Conservation of angular momentum and parity constrain the relative angular momenta in the break-up process to $l_1 = 2$ and $l_2 = 2$.

As shown in Figure 6.11 the 1^- and 3^- states decay through the ^8Be ground state. For the 3^- state this is the only open channel. The simulations therefore treat the break-up as proceeding via the $^8\text{Be}(\text{gs})$ and the relative angular momenta in the [$^{12}\text{C} \rightarrow \alpha + ^8\text{Be}$] and [$^8\text{Be} \rightarrow \alpha + \alpha$] break-up's are chosen as $l_1 = 3, l_2 = 0$ for the 3^- level and $l_1 = 1, l_2 = 0$ for the 1^- level. These are the only allowed combinations.

The natural parity strength observed at 10.0 MeV and in the interval 11.5-13.00 MeV are also simulated as proceeding through the ^8Be ground state. Since it is unclear which resonances in ^{12}C these events originate from, we perform two simulations, one treating the break-up events as succeeding E1 γ -decays and one treating them as succeeding M1 transitions. These multipolarities are chosen since they are expected to facilitate the largest transition rates compared to transitions of higher multipolarities. E1 and M1 transitions can populate several states of different spin and parities (see Table 3.2 in Section 3.3.2). As specified in Table 6.3 the E1 transitions are assumed

to populate 3^- states while the M1 transitions are assumed to populate structures with 2^+ .

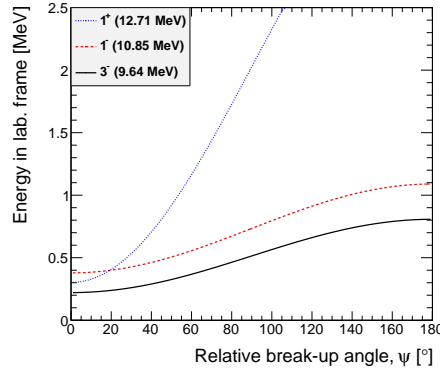


Figure 6.12: Ordinate: Laboratory energy of an α -particle emitted from ^8Be after decay of the 3^- , 1^- and 1^+ levels. Abscissa: Relative ^8Be break-up angle relative to the first emitted α -particle.

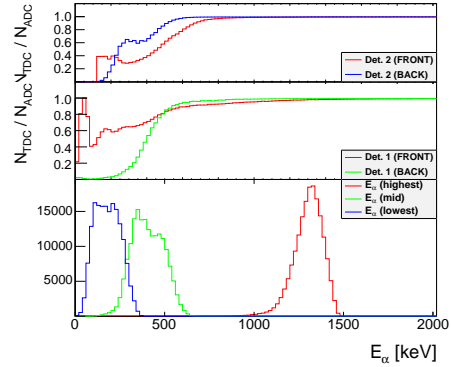


Figure 6.13: Bottom part shows simulated deposited energies of the three α -particles emitted from the 3^- level. Energy losses are taken into account. The two top plots show the trigger efficiency (summed over all strips) variation as a function of deposited energy in the detectors.

Several factors make it difficult to obtain precise and accurate triple coincidence detection efficiencies for the γ -delayed break-up's. Most importantly, threshold effects become problematic when simulating 3α decays from low lying states in ^{12}C due to the low energy of the emitted α -particles. This will in particular influence the detection efficiency for the 3^- state at 9.64 MeV. Figure 6.13 shows the trigger efficiency curves for detector 1 and 2 as determined from data set number 9. Also shown are the simulated energies of the three α -particles emitted from the 3^- level, which for each event are ordered in terms of their sizes. The energies are deposited energies, i.e. it is the energies that are directly relevant when comparing to detection thresholds. The energies of the secondary α -particles, represented by the two low energy peaks (the blue and green curves), are located close to - and even extending below - the detection thresholds. The simulation and analysis is therefore extremely sensitive to the applied threshold levels. Other systematic errors induced by geometry uncertainties and the growth in target foil thickness also contribute to the complexity in determining accurate efficiencies. The situation becomes less severe when moving up in excitation energy as seen from Figure 6.12, which shows the laboratory energy of a secondary α -particle from the 1^- and 1^+ states as function of break-up angle θ' . Note how the shape of the E vs. θ' curve for 1^+ is drastically different from the 3^-

and 1^- curves due to the different decay channels.

The obtained detection efficiencies for the 1^+ , 1^- and 3^- levels are presented in Tables 6.4 and 6.5, respectively, in the next section. Regarding groups four and five, only the final results concerning the transitions strengths are listed (see Table 6.7).

6.2.2 γ -widths and reduced matrix elements

The measured γ -width [$\Gamma_\gamma(16.11 \rightarrow E_i)$] is calculated from the total number of γ -decays [$N_{\gamma,i}^{\text{tot}}$] to the energy level E_i and the total number of decays from the 16.11 MeV level [$N_{16.11}^{\text{tot}}$]. The ratio of these quantities gives the γ branching ratio, still a relative measure, but exploiting that the total width of the 16.11 MeV state (Γ_{tot}) is known to 5.3(2) keV [AS90], gives the γ -width:

$$\Gamma_\gamma(16.11 \rightarrow E_i) = \Gamma_{\text{tot}} \frac{N_{\gamma,i}^{\text{tot}}}{N_{16.11}^{\text{tot}}}. \quad (6.4)$$

This merely states the definition of $\Gamma_\gamma(16.11 \rightarrow E_i)$, calculating it we need to convert the observed number of γ -decays [$N_{\gamma,i}^{\text{obs}}$] to the total number [$N_{\gamma,i}^{\text{tot}}$]. The same is required for total number of decays from the 16.11 MeV state. The observed γ -width is then calculated as

$$\Gamma_\gamma(16.11 \rightarrow E_i) = \Gamma_{\text{tot}} \frac{\frac{N_{\gamma,i}^{\text{obs}}}{\varepsilon_{\gamma,i}}}{N_{16.11}^{\text{tot}}} = \Gamma_{\alpha,\text{tot}} \frac{\frac{N_{\gamma,i}^{\text{obs}}}{\varepsilon_{\gamma,i}}}{\frac{N_{16.11,\text{gs}}^{\text{obs}}}{\varepsilon_{\text{gs}}} + \frac{N_{16.11,\text{exc}}^{\text{obs}}}{\varepsilon_{\text{exc}}}}, \quad (6.5)$$

where, at the second equality, the total width is replaced by the total α -width [$\Gamma_{\text{tot}} \rightarrow \Gamma_{\alpha,\text{tot}}$] and in the denominator the total number of decays is replaced by the total number α -decays. We approximate $\Gamma_{\text{tot}} \simeq \Gamma_{\alpha,\text{tot}}$, which is a valid assumption since any other decay modes than α -decay are smaller than the error on the total width. The proton width is $\Gamma_p = 0.0217(18)$, an order of magnitude smaller than the error on the total width.

The measured γ -widths for decays to the 1^+ , 1^- and 3^- states in each data set are shown in Tables 6.4 and 6.5, respectively. Note that apart from the case of the 1^- level, the number of observed γ -events in each data set is quite low. It is therefore a delicate task to retrieve trustworthy results based on such low statistics, which manifests itself in the relatively large statistical errors for the 1^+ and 3^- γ -widths. Some severe cases are apparent e.g. in data set number 7 where the error on the 1^+ result exhausts the deduced value while the 3^- value is highly outlying. The results are most uncertain in case of the 3^- state which is to be expected based on the discussion in the previous section.

A single value for the γ -widths deduced from the 10 data sets cannot be obtained from a simple weighted average due to the very low number of counts. Instead we

Table 6.4: Results obtained for each data set on the γ -decays to the 1^+ (12.71 MeV) and 1^- (10.85 MeV) levels. The second column in each table gives the number of observed γ -decays. The third column gives the obtained detection efficiency. The final column presents the γ -width in units of eV.

1^+ (12.71 MeV)				1^- (10.85 MeV)			
Data set	N_γ	$\varepsilon_\gamma \times 10^3$	Γ_γ [eV]	Data set	N	ε_γ	Γ [eV]
1	6	16(3)	0.082(33)(21)	1	38	37(4)	0.23(4)(5)
2	7	14(3)	0.17(7)(4)	2	21	21(2)	0.33(7)(7)
3	6	11(2)	0.30(12)(8)	3	30	21(2)	0.77(14)(16)
4	7	11(3)	0.17(6)(5)	4	38	19(3)	0.53(9)(13)
5	0	-	-	5	20	27(2)	0.50(11)(12)
6	5	17(3)	0.17(7)(4)	6	31	31(4)	0.55(10)(13)
7	1	17(6)	0.020(20)(5)	7	20	17(2)	0.42(9)(10)
8	4	17(9)	0.26(13)(7)	8	9	21(3)	0.50(17)(12)
9	11	20(3)	0.14(4)(3)	9	66	24(3)	0.71(9)(12)
10	24	16(4)	0.17(3)(4)	10	92	11(2)	0.94(10)(18)

perform a combined maximum likelihood analysis on two groups of data, one containing the data sets 1-5 and the second group containing data sets 6-10. This rough division is motivated by the large change in geometry between data set 5 and 6 (see Table 4.1). Since geometry uncertainties are responsible for most of the systematic uncertainties we assume the systematic uncertainties in these two groups to be uncorrelated. The Γ_γ -values and the corresponding reduced matrix elements recommended from this work are listed in Table 6.6. The reduced matrix elements, $B([E/M]L)$, which were defined in Eq. 3.7 in Section 3.7, are calculated from the $\lambda_\gamma = \frac{\Gamma_\gamma}{\hbar}$ values.

The results for the events at 10 MeV and in the 11.5-13.0 MeV region are listed in Table 6.7. The γ -width and reduced matrix element for the 10 MeV strength is very uncertain due to the low number of counts and the low excitation energy. For the six groups from 11.5 MeV to 13.0 MeV our results are obtained with a somewhat better precision.

6.2.3 Summary and discussion: γ -decay of the 16.11 MeV state

As presented in Figure 6.11, we observe clear evidence for γ -decays to the known 3^- , 1^- and 1^+ states at 9.64 MeV, 10.85 MeV and 12.71 MeV, respectively. This is the first time that γ -decays from the 16.11 MeV state have been seen using the method of indirect detection. Previously, only two transitions to unbound states have been ob-

Table 6.5: Results obtained for each data set on the γ -decays to the 3^- (9.64 MeV) level. The second column gives the number of observed γ -decays. The third column gives the obtained detection efficiency. The final column presents the γ -width in units of eV.

Data set	N	$\varepsilon_\gamma \times 10^3$	Γ [eV]
1	4	8.5(1.2)	0.10(5)(2)
2	2	2.2(3)	0.31(22)(7)
3	3	2.4(5)	0.67(39)(19)
4	8	2.2(3)	0.98(35)(23)
5	1	4.9(1.2)	0.13(13)(5)
6	2	5.5(1.1)	0.2(14)(6)
7	3	0.022(5)	50(30)(15)
8	1	1.7(3)	0.70(70)(18)
9	6	2.9(4)	0.52(21)(9)
10	6	1.9(3)	0.36(15)(7)

Table 6.6: Average values for the measured γ -widths to the 1^+ , 1^- and 3^- levels. The corresponding literature values are the adjusted values from from [Ade77] as listed in [AS90]. Reduced matrix elements are calculated assuming the lowest possible multipolarity possible.

	Γ_γ [eV]	Γ_γ [eV] (litt.)	$B(E1)$ [$e \text{ fm}^2 \times 10^{-3}$]	$B(M1)$ [$(\mu_N/c) \text{ fm}^2$]
1^+	0.14(2)(5)	0.19(4)	-	0.31(4)(11)
1^-	0.48(4)(11)	-	3.2(3)(7)	-
3^-	0.33(8)(8)	0.31(6)	1.2(3)(3)	-

served by conventional methods, namely to the 3^- and 1^+ states. Our measurement is therefore the first observation of γ -decays to the 1^- level, a fact that illustrates the power of our method. One can speculate why it was missed in the study by [Ade77] since it is the most intense transition in our measurement. A probable explanation is the large width of the state [$\Gamma = 272(5)$ keV], which makes it difficult to observe due to the complicated response of γ -ray detectors. In our method, based on the detection of charged particles, our spectra are not influenced by complicated detector responses.

The recommended values for the γ -widths and reduced matrix elements are shown in Table 6.6. The 3^- and 1^+ γ -widths agree with the literature values. The measured transitions are in general weak compared to the Weisskopf estimates. This can be seen by comparing to the examples calculated in Table 3.2 (Section 3.3.2) where the

Table 6.7: Results obtained averaging over all data sets on the γ -decay to the natural parity distribution at 10.0 MeV and at 15.5-13.0 MeV. The second column gives the number of observed γ -decays. Columns 3 and 5 give the γ -widths for the 2^+ and 3^- cases, respectively, while columns 4 and 6 present the corresponding reduced matrix elements.

ΔE [MeV]	N_{Tot}	2^+		3^-	
		Γ_γ [eV]	$B(M1)$ [$(\mu_N/c)\text{fm}^2$]	Γ_γ [eV]	$B(E1)$ [$e(\text{fm})^2 \times 10^{-3}$]
9.8-10.3	15	0.18(7)(6)	0.07(3)(2)	0.18(8)(6)	0.8(3)(3)
11.5-11.75	32	0.21(5)(5)	0.20(5)(5)	0.21(5)(5)	2.2(5)(5)
11.75-12.00	35	0.19(4)(5)	0.22(5)(6)	0.19(4)(5)	2.4(5)(6)
12.00-12.25	33	0.15(4)(4)	0.21(6)(6)	0.15(4)(3)	2.3(6)(4)
12.25-12.50	31	0.12(3)(3)	0.20(5)(5)	0.14(3)(3)	2.6(6)(6)
12.50-12.75	31	0.11(3)(3)	0.23(6)(6)	0.12(3)(2)	2.7(7)(5)
12.75-13.00	21	0.07(3)(2)	0.18(3)(2)	0.08(3)(2)	2.3(9)(6)

E1(M1) Weisskopf strength varies from 81 eV to 11 eV (0.5 eV to 7.8 eV) in the excitation energy interval from 10.0 MeV to 13.9 MeV.

The γ -decays to structures of natural parity at 10 MeV and 11.5-13.0 MeV is an additional and highly interesting result of our measurement. As pointed out earlier, these events must originate from genuine γ -decays, which raise the immediate question: which resonance or resonances are responsible for the measured strength? No resonances of natural parity state are known in the region around 11.5-14 MeV, making the question very interesting.

Just as interesting is it that the highly debated 2_2^+ state has been reported observed in the 10 MeV region [Fre12b] [Zim13b]. Most likely the transitions are of E1 or M1 nature, giving the highest transition rates. Allowed E1 and M1 transitions from a 2^+ state can populate 1^\pm , 2^\pm and 3^\pm states, of which 2^+ and 3^- would be particularly interesting. The 2^+ choice attracts attention because of the long search for the 2_2^+ , while the observation of a 3^- in the interval between 11 and 14 MeV could help distinguish between different geometric configurations of the Hoyle state. In [ML14] it is discussed how a 3^- state belonging to the Hoyle state rotation band is expected in this energy region on the basis of an algebraic cluster model [Bij00]. In this model the Hoyle state α -cluster configuration is treated as an equilateral triangle, and the observation or non-observation of states predicted from this model could provide information on the structure of the Hoyle state. Our results can in this respect prove very important, as the transitions to natural parity states might be the first indication of structures, which, when properly identified, hold information on the fundamental

structure of Hoyle state.

6.3 Conclusion

Using the $p + {}^{11}\text{B}$ reaction we have studied ${}^{12}\text{C}$ resonances by detecting the α -particles that are emitted in their decay. Our results on this reaction are divided into two parts.

First, the break-up mechanism for the directly populated resonance at an excitation energy of 16.11 MeV has been studied. The break-up of this state has been investigated and debated since the early days of nuclear physics, but with our high quality measurement, where the 3-particle final state is detected in double and triple coincidences, we are able to obtain precise information on the break-up mechanism. The state is shown to decay primarily through the first excited state in ${}^8\text{Be}$ in a sequential fashion where the relative angular momenta are $l_1 = 2$ and $l_2 = 2$. Imposing symmetry constraints on the 3- α final state prove important for an accurate description of the decay spectra. The presented comparisons to different theoretical models is the most accurate study of the decay-mechanism for the 16.11 MeV state to date.

The second part of our results concerns the γ -decay of the 16.11 MeV state. Clear evidence for transitions to three known states in ${}^{12}\text{C}$ has been obtained. One of these, to the broad 1^- state at 10.85 MeV, has never been observed before. Decays to natural parity states around 10 MeV and 11.5-13.0 MeV are also seen, providing evidence for new states. For a clear interpretation of these natural parity structures more statistics is needed. This will become important for our understanding of the structure in ${}^{12}\text{C}$, where problems, such as the location of 2^+ strength at these energies, are important. This interpretation is likely to have consequences for the 3- α reaction rate stellar environments being important for our understanding the chemical evolution of the universe. The observed natural parity structure in this work may well be due to 2^+ state(s).

Part II



Introduction

The second part of the thesis deals with the analysis of an experiment on the β -decay of ^{20}Ne . Detecting the α -particles emitted from ^{20}Ne resonances populated in the β -decay allows a study of resonances in ^{20}Ne . The presented data surpasses existing data in quality, motivating an improved understanding of the resonance spectrum. Like ^{12}C , ^{20}Ne displays significant cluster structure, and as a consequence the resonance spectrum populated in the β -decay is dominated by broad resonances making a correct analysis more challenging. This chapter introduces the physical system at hand, the more detailed motivation for studying it and some concepts relevant for its study. First the cluster structure of ^{20}Ne is briefly discussed whereafter its astrophysical significance is described. Next follow a general introduction to β -decay, describing some relevant concepts and the specific case of ^{20}Ne . Finally the experiment is briefly discussed.

7.1 ^{20}Ne structure

The description of ^{12}C as made up of α -particle clusters was, as discussed in the introduction in Part 1, motivated by the even number of protons and neutrons and the fact that the α -particle is a robust entity. In a similar manner, the even-even nucleus ^{20}Ne is also considered as a cluster system. The cluster structure in ^{20}Ne consists of the asymmetric arrangement of an α -particle and the closed shell nucleus ^{16}O .

The $[\alpha + ^{16}\text{O}]$ cluster structure of ^{20}Ne has often been cited as one of the best examples of clustering in light nuclei [Fre07] and it has been the subject of numerous studies, both theoretically [Buc95, Kim04] and experimentally [Hin83, Mic87, Ric84], with the identification of several rotational bands containing resonances with very large α -widths. Figure 7.1 shows an example in which the experimentally observed energy levels in the first two rotational bands are reproduced excellently in a simple $[\alpha + ^{16}\text{O}]$ potential model [Buc95]. The more advanced AMD framework, treating the nucleus at a microscopic level without the initial assumption of clustering, also reproduce the asymmetric cluster arrangement in ^{20}Ne [Kim04].

The experimental signature of clustering in ^{20}Ne comes from measurements of enhanced γ -transition rates between states belonging to the same rotational bands

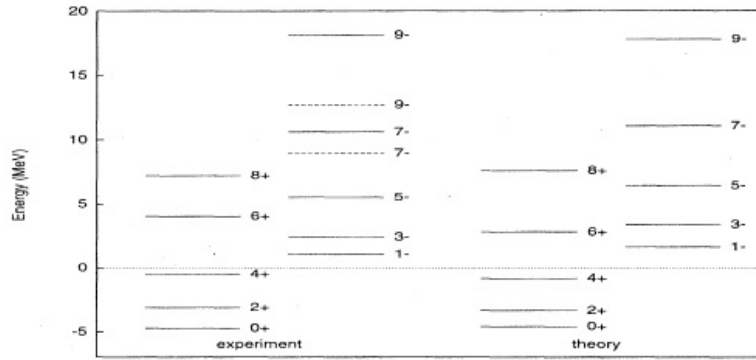


Figure 7.1: Comparison of the experimental energy spectrum in the two lowest rotational bands in ^{20}Ne with predictions from the simple $\alpha + ^{16}\text{O}$ core model in [Buc95]. The band heads are the ground 0^+ state and the excited 1^- state. Illustration from [Buc95].

[Mac80] and the identification of states showing large α -widths compared to the Wigner-limit (α -decay widths close to the Wigner-limit is a signature of α -clustering). This work reports on the observation of the second 2^+ resonance in the fourth 0^+ rotation band in ^{20}Ne . As will be presented, the state is observed at 8.77(2) MeV and due to its very large α -width it is interpreted as a cluster state.

7.2 Astrophysics: $^{16}\text{O}(\alpha, \gamma)^{20}\text{Ne}$

In Section 1.4 it was explained how the existence of a natural parity state inside the Gamow window facilitate a $3\text{-}\alpha$ reaction rate high enough to account for the observed amounts of carbon and oxygen in the universe. The excitation spectrum of ^{20}Ne plays a similar important role for nucleosynthesis, but in this case with the opposite effect.

After the formation of ^{16}O , the next step in the main reaction chain of helium burning is the $^{16}\text{O}(\alpha, \gamma)^{20}\text{Ne}$ reaction. This reaction determines the stellar abundance of ^{16}O before the next burning phase, carbon burning, sets in. The fact that ^{16}O survives the phase of helium burning and is a relative abundant nucleus in the universe, is in part attributed to the slow $^{16}\text{O}(\alpha, \gamma)^{20}\text{Ne}$ reaction rate. Therefore, in the mindset of Hoyle, the slow reaction rate is no surprise and it must be attributed to the low energy structure of ^{20}Ne .

The explanation is obtained by studying Figures 7.2 and 7.3, which show the ^{20}Ne level scheme and the Gamow window for the $^{16}\text{O}(\alpha, \gamma)^{20}\text{Ne}$ reaction, respectively. The Gamow window is plotted for $T = 0.2 \times 10^9$ K. The level scheme includes all states in the proximity of the α -threshold (within ± 1 MeV) which may be involved

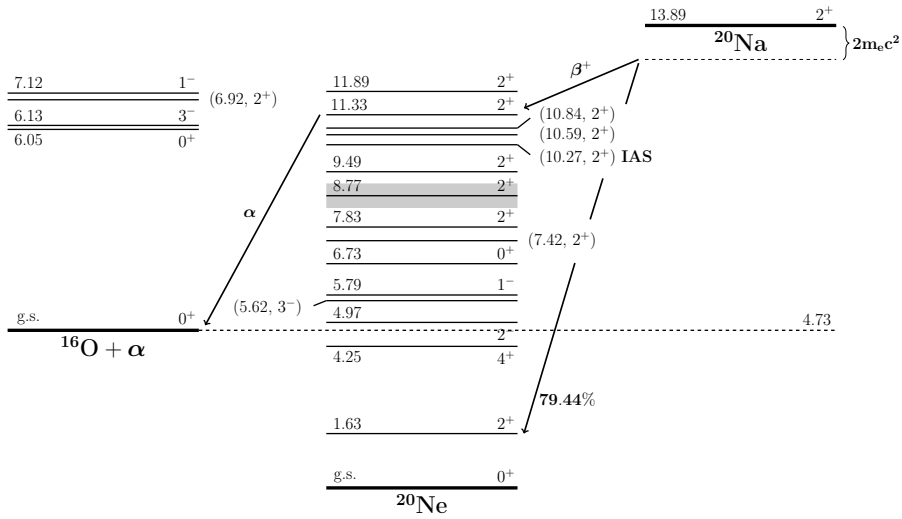


Figure 7.2: Level scheme for ^{20}Ne showing states relevant for an astrophysical discussion (near the $\alpha+^{16}\text{O}$ threshold) and above threshold states from which β -delayed α -particles are measured in the present work.

in the reaction. The two arrows shown in the Gamow window reflect the energy positions of the first two levels above the α -threshold at $E_{\alpha+^{16}\text{O}} = 4.730$ MeV. If the resonance level at $E_r = 0.24$ MeV, which lies fairly close to the Gamow window maximum at 390 keV, had natural parity it would facilitate the α -capture process, just as the Hoyle states does in the 3α reaction. However, as seen in the figures, it has unnatural parity and cannot contribute to the process. The first level of natural parity (3⁻) occurs at a center-of-mass energy of 0.89 MeV and contributes only through its low energy tail. A resonance of natural parity (4⁺), located 0.48 MeV below $E_{\alpha+^{16}\text{O}}$, contributes by its high energy tail. These non-resonant contributions are in general small, preventing a large reaction rate. The reaction is additionally hindered by the centrifugal repulsion due to the large angular momenta involved (d and f waves). To summarize, the absence of natural parity resonances in the Gamow window is responsible for the slow $[\alpha + ^{16}\text{O}]$ reaction rate.

Recently two measurements of the $^{16}\text{O}(\alpha, \gamma)^{20}\text{Ne}$ reaction [Cos10, Hag11] have been carried out with the purpose of obtaining the astrophysical *S-factor* at the Gamow window. In [Cos10] an *R*-matrix analysis was used to extract details about the reaction mechanism and it was found that the main contribution comes from so-called *direct s-wave* capture onto the first excited state in ^{20}Ne . Direct capture is a non-resonant nuclear reaction mechanism occurring in one step, not involving the formation of a compound nucleus. In this context it is interesting that the results presented in this

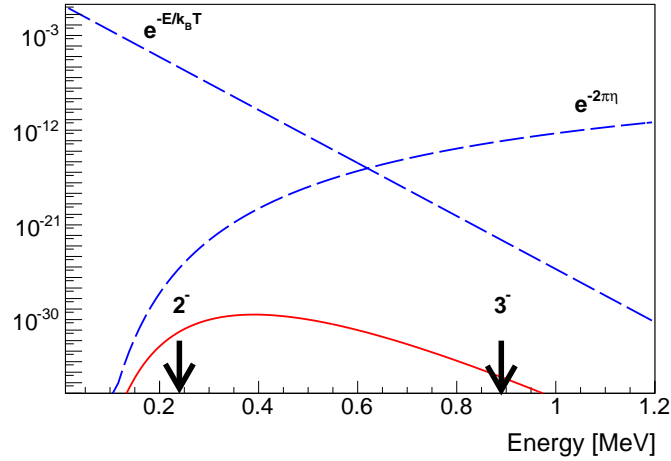


Figure 7.3: Figure showing the Maxwell-Boltzmann factor ($e^{-E/k_B T}$) and the Gamow factor ($e^{-2\pi\eta}$) for a temperature of 0.2 GK in case of the ${}^4\text{He} + {}^{16}\text{O}$ reaction. Both these factors enter the integrand in Eq. 1.8 (Section 1.4) and their product, the red solid line, determines the energies at which thermonuclear processes occur. The arrows indicate the positions of the ${}^{20}\text{Ne}$ resonances closest to the Gamow window. The ordinate is in arbitrary units.

thesis gives information about a very broad resonance located at higher energy. Contribution to the non-resonant cross section via this resonance is an interesting possibility, which was not included in the R-matrix analysis of [Cos10].

7.3 β -decay

The nuclei on either side of the stability line are radioactive and decay weakly. Those with an excess of neutrons decay by β^- -decay toward the valley of stability, while proton rich nuclei decay by β^+ -decay or electron capture. ${}^{20}\text{Na}$ decays by β^+ -decay (see figure 7.4). The general reaction scheme for the β^+ -decay of the *parent* nucleus \mathbf{X} to the daughter nucleus \mathbf{Y} looks like



and neglecting electronic binding energies the Q-value is

$$Q_{\beta^+} = [M({}^A_Z\mathbf{X}_N) - M({}^A_{Z-1}\mathbf{Y}_{N+1}) - 2m_e] c^2.$$

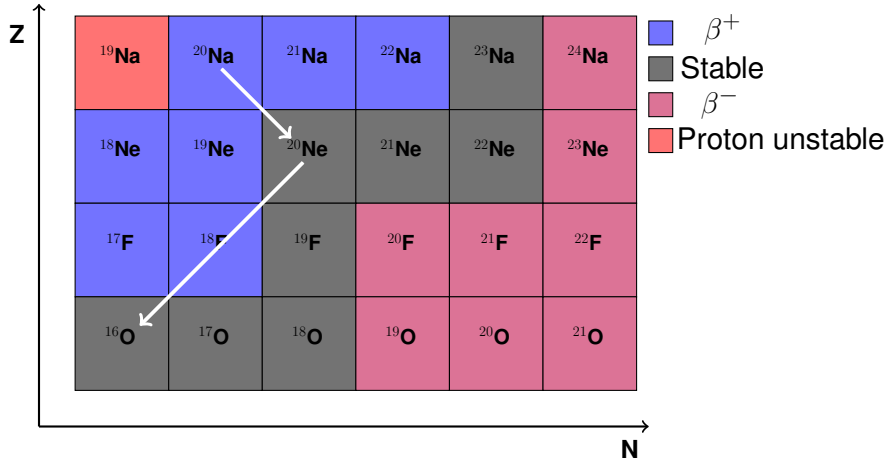


Figure 7.4: Section of the nuclear chart. Arrow pointing from upper left indicates β^+ -decay while the other signifies the possible α -emission.

7.3.1 Fermi and Gamow-Teller decays

The history of our understanding of β -decay, which is a weak process, presents an interesting story. Not until 1957, with the observation of parity violation, could the weak interaction Lagrangian be settled to constitute of both a vector and a axial-vector part. These two parts are represented by the following transition operators relevant for β^+ -decay,

$$\hat{O}_V = -\frac{G_F}{\sqrt{2}} \delta(\mathbf{r} - \mathbf{r}') \hat{T}_- \quad (7.1)$$

$$\hat{O}_A = -\frac{G_F}{\sqrt{2}} \frac{g_A}{g_V} \frac{2\mathbf{s}}{\hbar c} \delta(\mathbf{r} - \mathbf{r}') \hat{T}_-, \quad (7.2)$$

where G_F is the *Fermi* coupling constant related to the weak charge, g_V and g_A the strengths of the vector and axial-vector contributions, \mathbf{s} the spin operator and \hat{T}_- the isospin lowering operator. These operators cause two different β -decay modes. The vector operator corresponds to β -decays where the spins of the emitted leptons couple to zero leaving the nuclear spin unchanged, these decays are called *Fermi* decays. In decays involving \hat{O}_A the lepton spins on the other hand sum to one and the nuclear spin is allowed to change. These decays are called *Gamow-Teller* decays.

A Fermi decay does also not change the isospin, which implies that it populates a state in the same isospin multiplet very similar to the initial state. Only the $N - Z$ value changes leaving all remaining quantum numbers unchanged. This state is called the *Isobaric Analog State* (IAS). Due to invariance of the nuclear force on

the third component of isospin the energy position of the IAS is determined by the electromagnetic interaction. The possibility of spin and isospin change makes the Gamow-Teller strength distribution quite different from the Fermi one.

The different properties of Fermi and Gamow-Teller decays implies that the recoil momentum of the daughter nucleus on average is larger in a Fermi decay than in a Gamow-Teller decay. This owes to the fact that weak interactions only couple to left-handed fermions and right-handed anti-fermions, which for a Fermi transition means that the lepton spins only can couple to zero if they move in the same direction¹ and thereby prompting maximum recoil to the daughter nucleus. In Gamow-Teller transitions the leptons will move in opposite directions leading to the opposite effect.

7.3.2 Matrix elements and ft values

The matrix element describing the β -decay to a given state $\langle f |$ in the daughter nucleus, $M_{F/GT} = \langle f | \hat{O}_{V/A} | i \rangle$, relates to the partial half live, $t_\lambda^{1/2}$, for decays to that state by

$$f(E_\lambda) t_\lambda^{1/2} = \frac{B}{|M_F|^2 + \frac{g_A^2}{g_V^2} |M_{GT}|^2} = \frac{B}{B_F + \frac{g_A^2}{g_V^2} B_{GT}}, \quad (7.3)$$

where $f(E)$ is the phase space function, $B = 6147 \pm 2 \text{ s}$ [Har05] is a constant and $|\frac{g_A}{g_V}| = 1.2695 \pm 29$ [Yao06]. The phase space function is highly energy dependent, an important fact to keep in mind when extracting the B_{GT} values for a low-lying states, which are favoured by phase space considerations. Even though the branching to such a state might be high they do not necessarily carry much of the total B_{GT} strength.

The measured values for B_F and B_{GT} constrain theoretical models that seek to describe the parent and daughter nuclei.

7.3.3 β -delayed particle emission

Moving toward the driplines the isobaric mass differences increases parabolically and the binding energy of the least bound nucleon or cluster (e.g. an α -particle) will decrease. This circumstance increases the possibility that a β -decay will populate particle unbound states in the daughter nucleus, which subsequently decays by emitting the type of particle to which it is unstable. This kind of delayed particle emission is an interesting object of study. It facilitates a way to measure properties of unbound resonances as done in the study presented here. Another reason for studying β -delayed particle emission is found in [Cli89] where it made a test of the Conserved Vector Current hypothesis (CVC) possible.

¹Holds strictly true in the relativistic limit.

7.4 β -decay of ^{20}Na

^{20}Na is located on the proton rich side of the stability line and its β -decay to ^{20}Ne has been the subject of many experimental investigations. One of them [Cli89] measured Fermi and Gamow-Teller decay components for six allowed decays by studying angular correlations between the delayed α -particle and the positron. In combination with the measured ft value for the IAS, located at an excitation energy of 10.274 MeV, they could determine the vector coupling constant g_V , appearing in Eq. 7.2, and thereby testing the CVC hypothesis. In addition, though not the main aim of their work, they gave a new interpretation of the β -delayed α -spectrum in terms of populated levels in ^{20}Ne . This interpretation gave part of the motivation for the present study, because a proper R -matrix analysis, as shall be seen, expose it as incorrect.

Interest in the [$\alpha + ^{16}\text{O}$] cluster structure of the even-even nucleus ^{20}Ne is another reason for studying this decay. The cluster structure is indicated by the broad structure around 3 MeV in the β -delayed spectrum (Figure 7.6), which must be analyzed in a framework treating interference phenomena correctly due to overlapping structures resulting from resonances with the same spin and parity. In the analysis presented here, an R -matrix analysis is applied in order to meet this challenge.

The astrophysical importance of ^{20}Ne makes yet another motivation for studying the β -decay of ^{20}Na . Obtaining precise experimental information for broad levels of natural parity in ^{20}Ne is relevant for a precise determination of the astrophysical S -factor in the $^{16}\text{O}(\alpha, \gamma)^{20}\text{Ne}$ reaction, as discussed in Section 7.2.

7.5 Present experiment

The experiment producing the β -delayed α -spectrum was performed in 2008 at University of Jyväskylä at the IGISOL radioactive beam facility. The ^{20}Na data was originally only intended as calibration data for a precision measurement of the ^8B decay [Kir11]. The ^{20}Na ions were produced through the reaction $^{24}\text{Mg}(p, n\alpha)^{20}\text{Na}$ using the Ion Guide Isotope Separator On-Line technique (IGISOL) [Ä01]. The proton primary beam had an energy of 40 MeV and a typical intensity of 8-10 μA . The produced ions were, after mass separation, implanted in a thin carbon foil ($26 \pm 2 \frac{\mu\text{g}}{\text{cm}^2}$) surrounded by four double sided silicon strip detectors (DSSSD) each backed by an unsegmented silicon detector. The DSSSD's were 60 μm thick stopping all the α -particles while the β -particles passed through. The detector setup is shown in figure 7.5.

The data recording was split in two runs lasting 5 and 7 hours, between which the vacuum was not broken. Several experimental circumstances e.g. very thin detector dead layers and low trigger thresholds made detection of the low-energy recoiling

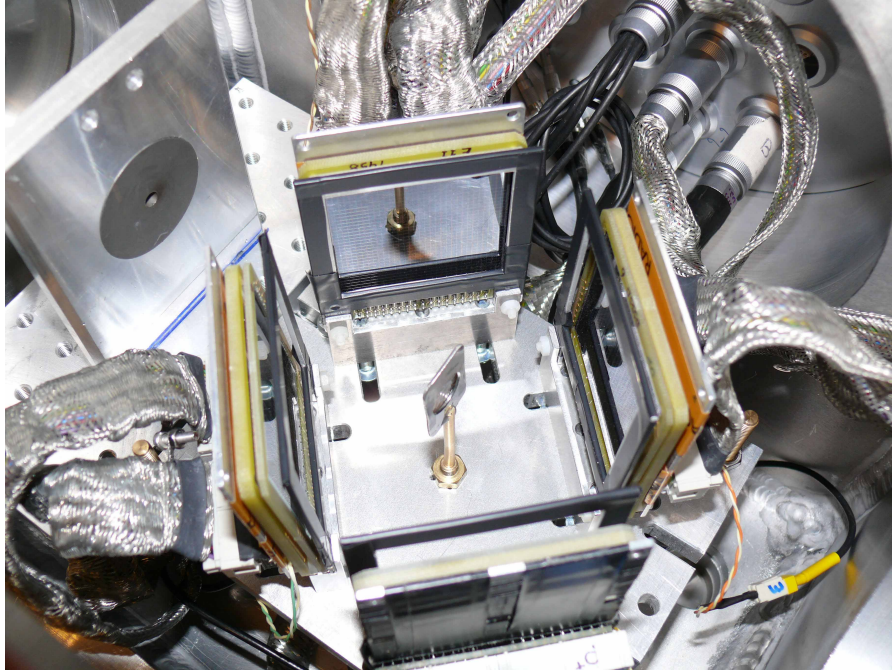


Figure 7.5: Detector setup in the Jyväskylä experiment.

^{16}O nuclei possible. This triggered the observation of new low energy α -lines. The results on these new lines are published in [Lau13]. For more details concerning the experimental setup see [Kir11].

7.6 Data

The recorded spectrum in detector 1 during the second run is presented on a log scale in Figure 7.6. The spectrum, consisting of single particle events, displays several pronounced features. At low energies two intense peaks appear at energies around 0.54 MeV and 1.11 MeV. These are identified as the ^{16}O recoils associated with the two most intense α -particle peaks located at $E_\alpha = \frac{m_{^{16}\text{O}}}{m_\alpha} E_{^{16}\text{O}} = 2.15$ MeV and $E_\alpha = 4.43$ MeV. The numbering follows the interpretation in [Cli89] and will be referred to later on. See for example table 10.1 on page 132. The low energy shoulders marked by asterisks are satellite peaks occurring due to extra energy loss in the front side aluminum grid that covers $\sim 5\%$ of the detectors.

The spectrum displays a very characteristic interference minimum around 3 MeV which is of key interest in the present study. The broad feature in this region indicates

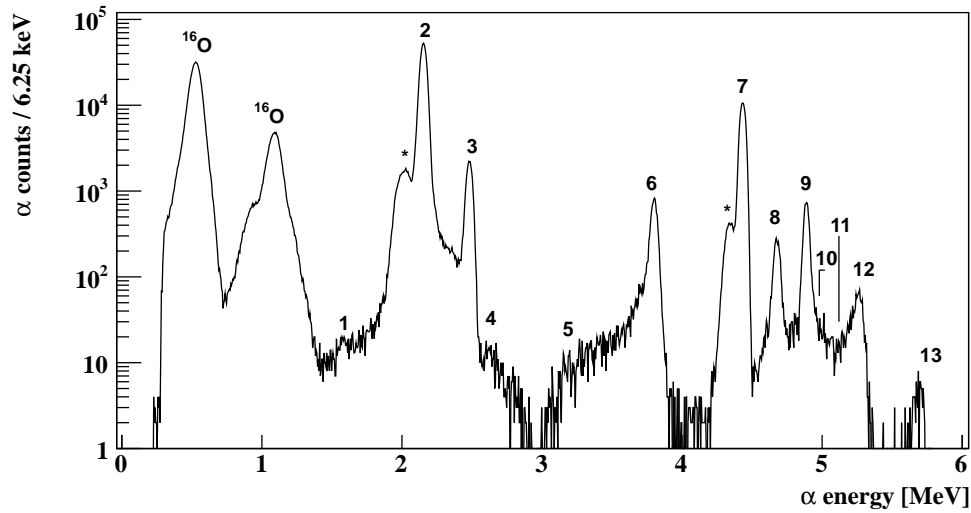


Figure 7.6: Events recorded in DSSSD 1 in the 2nd run. Numbering reflects the interpretation of [Cli89]. Asterisks indicate the position of satellite peaks.

the presence of a very broad resonance in ^{20}Ne . A broad 2^+ state, the second member of the fourth 0^+ rotational band, with a width of ~ 800 keV and $E = 9.00 \pm 180$ MeV is known to be populated in two scattering experiments [$^{16}\text{O}(\alpha, \alpha), ^{20}\text{Ne}(\pi, \pi')$] [McD60] [Bur89] and a reaction experiment ($^{19}\text{F}(^3\text{He}, d)^{20}\text{Ne}^*$) [Til98]. In the comprehensive work done on $^{20}\text{Na}(e^+\nu_e)^{20}\text{Ne}$ in [Cli89] a broad distribution is also observed, but even though the possibility is mentioned, they do not attribute it to the 2^+ state in the 0_4^+ -band. The state has also been predicted theoretically as e.g. in the AMD calculation of Kimura [Kim04].

So the natural question arises: is the broad distribution seen in the present data the first evidence for β -decay to the second member of the 0_4^+ -band? In order to conclude on that question one needs to analyse the recorded spectrum in a rigorous way that, besides from including interference effects, also corrects for different experimental effects. The R -matrix formalism, which adequately describes a spectrum consisting of broad resonances, is utilized in the present analysis and will be introduced in the next chapter.

R-matrix theory

As described in Section 1.1, the modern study of nuclear reactions began in the early 1930's. Experiments in which different nuclei were bombarded by neutrons and protons revealed the existence of many narrow and closely spaced resonances. These observations led to the *compound nucleus* model first proposed by Bohr in the 1930's. This model, in which the energy of the incident projectile is shared rapidly among the target nucleons, initiated the development of theoretical frameworks describing nuclear resonances. Breit and Wigner gave at the same time a cross section formula successful in fitting a large amount of data describing nuclear resonances. This formula, adequate in describing narrow non-interfering resonances, is named the *Breit-Wigner* formula

$$\sigma \propto \frac{\Gamma_i \Gamma_f}{(E - E_\lambda)^2 + \frac{\Gamma_{\text{tot}}^2}{4}}. \quad (8.1)$$

The applicability of this formula is however limited and several more formal frameworks were quickly developed. One of these, the *R-matrix* framework, originally worked out by Wigner and Eisenbud, has turned out to be successful in analysing data related to astrophysical important nuclear reactions. This work makes use of this tool in analyzing the ^{20}Na data.

Central to the *R-matrix* theory is the division of configuration space into an internal and external region. The internal region corresponds to the compound nucleus and is where all the nuclear interactions take place. The external region defines the reaction channels and the only interactions in this region are Coulomb interactions. The *R-matrix* theory parameterizes the nuclear problem such that a solution of the Schrödinger equation is not required in the internal region. Matching the exact solutions for the wave function in the external region to those in the internal region one can extract parameters describing the internal states. One of the main advantages of *R-matrix* theory is that the *R-matrix* parameters have a direct interpretation in terms of physical properties of the nuclear states in question.

In the following section the basics of the *R-matrix* formulation will be presented. The description is similar to the ones in [Hy110a] and [Lan58b]. Next will follow a description of how to implement the *R-matrix* theory as a data analysis tool with emphasis on the application to β -delayed particle emission.

8.1 Basic theory: Inner and outer region

The overall goal is to find the cross section for a nuclear process. As pointed out above, the essential idea is to match the wave functions in the inner region to the solution in the outer region. This is done by using an appropriate boundary condition at the matching radius $r = a_c$ for the given channel c . The channel is specified by the nuclei appearing in it and their relative angular momentum.

Therefore, solving the Coulomb problem analytically for systems in the external channels, allows information on the nuclear parameters of the internal region to be gained. The fundamental assumption behind this procedure is that all interactions of nuclear type are confined to the inner region.

The wave function in the external region is written as

$$\Psi = \sum_c \psi_c u_c(r), \quad (8.2)$$

where ψ_c is the channel wave function containing the channel quantum numbers such as spin and angular momentum, and $u_c(r)$ is the radial wave function which is a solution to the radial Schrödinger equation [Bra03],

$$\left[\frac{d^2}{dr^2} - \frac{l(l+1)}{r^2} - U(r) + k^2 \right] u(r) = 0, \quad (8.3)$$

where $U(r) = \frac{2mV(r)}{\hbar^2}$ ($V(r)$ being the Coulomb potential) and $k^2 = \frac{2mE}{\hbar^2}$. It is possible to make a power series expansion for $u(r)$ ¹ and the solutions found will be the irregular and regular Coulomb functions, denoted by G_c and F_c , respectively. From these the incoming (I_c) and outgoing (O_c) wave functions are found and the radial wave function can be written as

$$u_c = \frac{1}{\sqrt{v_c}} (x_c O_c + y_c I_c), \quad (8.4)$$

where x_c and y_c denote the amplitudes of the incoming and outgoing waves respectively. The relative velocity is given by v_c . An important quantity, the *collision matrix*, is defined as

$$x_{c'} = - \sum_c U_{c'c} y_c, \quad (8.5)$$

relating the outgoing and incoming amplitudes resulting from all channels considered. This matrix represents the physics at play in the inner region dominated by the nuclear forces.

¹As long as the potential is less singular than r^{-2} .

In R -matrix theory the collision matrix is constrained by matching the outer wave functions to the inner ones at the matching radius a_c . Without concern for the complicated form of the nuclear potential, the Schrödinger equation in the inner region is written as

$$H\Psi = E\Psi. \quad (8.6)$$

The eigenstates of this region, X_λ , form a complete basis fulfilling

$$HX_\lambda = E_\lambda X_\lambda. \quad (8.7)$$

The total wave function is expanded in terms of these eigenstates, $\Psi = \sum_\lambda C_\lambda X_\lambda$, where C_λ are the expansion coefficients. The eigenstate wave functions in the internal region are constrained by their logarithmic derivatives at boundary surface,

$$a_c \left. \frac{dX_\lambda}{dr} \right|_{r=a_c} = B_c X_\lambda(a_c), \quad (8.8)$$

which ensures the correct behaviour in the nuclear region. The value for the boundary parameter B_c is to some extent a matter of choice, related to the problem of extracting observed physical parameters of the internal system, i.e. the compound nucleus at hand. This is discussed further in Section 8.3.

Derivation of the collision matrix, central to the R -matrix theory, is shown in appendix A. Some concepts introduced in that appendix is referred to later on.

8.2 Application to β -delayed particle emission

The R -matrix formalism applied to β -delayed break-up is applied in this work. The R -matrix formula for exit channel c , written as a decay probability, is given by [Bar88]:

$$w_c(E) = C^2 f_\beta P_c \sum_{x=F,GT} \left| \sum_{\lambda\mu} g_{\lambda x} \gamma_{\mu c} A_{\lambda\mu} \right|^2, \quad (8.9)$$

where C is a normalisation constant, f_β is the phase space function and $g_{\lambda x}$ is a parameter containing the β -decay strength to the level λ . The other quantities appearing P_c , $\gamma_{\mu c}$ and $A_{\lambda\mu}$ are introduced in Equations A.17, A.7 and A.15 respectively. $\gamma_{\mu c}$ is the reduced width of the level λ and $A_{\lambda\mu}$ is the *level-matrix*. The outer sum runs over Fermi (F) and Gamow-Teller (GT) decay contributions, which do not interfere, while the sum inside runs over the populated levels λ and μ . The parameters $\gamma_{\mu c}$ and $g_{\lambda x}$ are measures of the overlap between the resonance wave function and the outgoing and incoming channel wave functions, respectively.

Fitting Eq. 8.9 to a β -delayed particle spectrum with N counts is performed by calculating the expected number of counts as function of energy, which then is

$$N(E) = \frac{NT_{1/2}}{\ln 2} w_c(E), \quad (8.10)$$

where $t_{1/2}$ is the β -decay half life.

8.3 Physical parameters

When extracting parameters for a resonance level, which in case of β -delayed α -particle emission are the level energy, α -width and β -decay matrix element, it is instructive to look at Eq. 8.9 in the limiting case of one level and compare to the Breit-Wigner formula (8.1):

$$w_c = C^2 f_\beta P_c \sum_{x=F,GT} \left| \frac{g_{\lambda x} \gamma_{\lambda c}}{(E_\lambda - E) - \sum_c \gamma_{\lambda c} (S_c - B_c + iP_c)} \right|^2. \quad (8.11)$$

Taking the norm square gives many terms in the denominator but after some manipulations one get

$$w_c = C^2 f_\beta \sum_{x=F,GT} \frac{|g_{\lambda x}|^2 \frac{1}{2} \Gamma_\lambda}{(E_\lambda - E + \Delta_\lambda)^2 + \frac{1}{4} \Gamma_\lambda^2}, \quad (8.12)$$

where $\Delta_\lambda = -\sum_c \gamma_{\lambda c}^2 (S_c - B_c)$ and $\Gamma_\lambda = \sum_c 2P_c \gamma_{\lambda c}^2$ have been introduced. This looks in some sense as the Breit-Wigner formula (Eq. 8.1) but it has some "new" features. First of all the Δ_λ has been added in the denominator and secondly, this quantity and Γ_λ are now energy dependent through their dependence on the shift function (S_c) and the penetration function (P_c) which are introduced in Eq. A.16 and A.17, respectively. Making a first order expansion of Δ_λ around E_λ , which gives $[\Delta(E_\lambda) - \gamma_{\lambda c}^2 (E - E_\lambda) \frac{dS}{dE}|_{E=E_\lambda}]$, and inserting in Eq. 8.12 we get

$$w_c = C^2 f_\beta \sum_{x=F,GT} \frac{|g_{\lambda x}|^2}{[1 + \sum_c \gamma_{\lambda c}^2 \frac{dS}{dE}|_{E=E_\lambda}]} \frac{\frac{1}{2} \Gamma_\lambda^\circ}{(E_\lambda - E + \Delta_\lambda^\circ)^2 + \frac{1}{4} (\Gamma_\lambda^\circ)^2}, \quad (8.13)$$

where the energy dependence of Δ_λ has been removed since Δ° is given as $\Delta_\lambda(E_\lambda) / (1 + \sum_c \gamma_{\lambda c}^2 \frac{dS}{dE}|_{E=E_\lambda})$. The $^\circ$ marks quantities as *observed* ones. This is as far as one gets in comparing the one-level R-matrix decay formula to the Breit-Wigner formula and the observed width of the level λ is identified as

$$\Gamma_\lambda^\circ = \frac{\sum_c 2P_c \gamma_{\lambda c}^2}{1 + \sum_c \gamma_{\lambda c}^2 \frac{dS}{dE}|_{E=E_\lambda}}. \quad (8.14)$$

The observed resonance energy for the level λ is not necessarily equal to the R-matrix parameter E_λ , but instead $E_\lambda + \Delta(E_\lambda)$. At this energy the decay probability (Eq. 8.12)

peaks. Typically the energy shift is eliminated by choosing $B_c = S_c$ for one specific level, making E_λ the observed energy. Obviously this can not be done simultaneously for all levels and the R -matrix parameters must be transformed in order to satisfy $S(E_\lambda) = B_c$ for the other levels [Dig06].

At first sight it seems surprising that the width Γ_λ and energy shift Δ_λ is energy dependent. One way to comprehend these phenomena is by realising that the external wave function will vary across the width of the nuclear resonance. This will lead to a large energy shift for broad levels.

8.3.1 Level matrix: Alternative form

It is possible to form an alternative level matrix $\bar{A}_{\lambda\mu}^{-1}$ depending directly on the observed parameters which we denote as \bar{E}_λ , $\bar{\gamma}_\lambda$ and \bar{g}_λ . These are equal to the parameters one would get by using Eq. A.15 with $B_c = S_c(E_\lambda)$. The derivation is described in [Bru03] and results in the following expression for $\bar{A}_{\lambda\mu}^{-1}$

$$\begin{aligned} \bar{A}_{\lambda\mu}^{-1} &= (\bar{E}_\lambda - E) \delta_{\lambda\mu} - \sum_c \bar{\gamma}_{\lambda c} \bar{\gamma}_{\mu c} (S_c + iP_c) \\ &+ \sum_c \begin{cases} \bar{\gamma}_{\lambda c}^2 S_{\lambda c} & , \quad \lambda = \mu \\ \bar{\gamma}_{\lambda c} \bar{\gamma}_{\mu c} \frac{S_{\lambda c}(E - \bar{E}_\mu) - S_{\mu c}(E - \bar{E}_\lambda)}{E_\lambda - \bar{E}_\mu} & , \quad \lambda \neq \mu. \end{cases} \end{aligned} \quad (8.15)$$

8.3.2 β -decay matrix elements

When describing how strongly a β -decay populates different states in the daughter nucleus there are basically two ways of doing that. Either one can use the ft -value which relates to the branching ratio, BR_λ , for the level in question as

$$f(E_\lambda) t_\lambda^{1/2} = f(E_\lambda) \frac{t^{1/2}}{BR_\lambda}, \quad (8.16)$$

where $t_\lambda^{1/2}$ is the partial half live. As another measure one can use the $B_{F/GT}$ value (see Eq. 7.3 on page 110). The first approach is straightforward if the measured spectrum consist of narrow and well separated peaks. In that case the measured intensity is simply counted at the relevant energy regions. In the case of broad and overlapping states, which may even interfere, there is however no clear-cut definition of how to extract branching ratios. Another issue with this approach, in particular concerning broad states, appears when interpreting the ft value as a strength parameter for a given state. The fact that the phase space function is strongly varying with energy makes the concept of one ft value for a broad β fed state quite unclear.

Extraction of matrix elements follows the procedure in [Bar88], where the decay

probability to only one level λ is defined to be

$$w_\lambda = C^2 \sum_{x=F,GT} g_{\lambda x}^2 \int_0^Q f_\beta P_c \left| \sum_\mu \gamma_{\mu c} A_{\lambda\mu} \right|^2 dE, \quad (8.17)$$

which is just Eq. 8.9, including feeding to the level λ only, and integrated from 0 energy up to the Q-value. This definition is a choice, and again it has to be emphasized that there can be an interpretation problem in the case of overlapping resonances just as introduced above when talking about the branching ratios. Though, as argued in [Bar88], this definition is as a sensible one because most of the interference is included in $|\sum_\mu \gamma_{\mu c} A_{\lambda\mu}|^2$, which follows because the diagonal elements in $A_{\lambda\mu}$ dominates. Specifying this central idea and introducing

$$J_\lambda = \sum_c \int P_c \left| \sum_\mu \gamma_{\mu c} A_{\lambda\mu} \right|^2 dE, \quad (8.18)$$

one calculates the reduced matrix elements as

$$B_{\lambda x} = C^2 g_{\lambda x}^2 \frac{B J_\lambda}{\ln(2)}, \quad (8.19)$$

where a factor of $\frac{g_V^2}{g_A^2}$ enters if $x = GT$. See [Bar88] for details.

Analysis

This chapter presents in detail the analysis of the β -delayed α -spectrum. The overall goal of the analysis is to fit the observed data with the R -matrix theory (Eq. 8.9 on page 117), and retrieve the physical parameters concerned with the α -decaying levels in ^{20}Ne . Before a sensible fit can be made a preliminary analysis must be done. The calibration procedure will only be described briefly, as it resembles the one already discussed in case of the $p + ^{11}\text{B}$ experiment (see Section 4.4.4). Next, two effects that broadens the measured α -particle peaks are discussed. These stem from the recoil motion in the β -decay and the response of the detection system. Finally the fitting procedure and the retrieval of observed parameters is described.

9.1 Energy calibration

The calibration procedure, presented in detail in [Kir11], uses the two most intense α -peaks at 2.15 MeV and 4.43 MeV, which originates from the 7.42 MeV and 10.27 MeV levels in ^{20}Ne , respectively. These levels have well defined energies and are therefore suitable. The α -particle energies were carefully corrected for energy losses in the carbon foil and the detector deadlayer. Further corrections were made because of the ADC non-linearities and non-ionizing energy loss in the active detector region which does not contribute to the measured signal. Only the uncertainty from the calibration is significant in the case of this study.

The calibration uncertainty was calculated by a simple model where the tabulated uncertainty [Til98] on the two energies was used, while no uncertainty on channel number was assumed. This resulted in a parabola for σ_E as a function of energy, giving an approximate error of 2 keV in the region of interest.

9.2 Recoil broadening

In order to compare the measured spectrum to theory, in this case to do a R -matrix fit, any kinematic or electronic effects that distort the measured spectrum has to be taken into account. First we consider the broadening effect caused by the β -recoil of the ^{20}Ne nucleus. The α -particles that are detected in this experiment are emitted from

^{20}Ne nuclei that are in motion due to the recoil from the emitted leptons. Conservation of energy and momentum implies that most of the released energy is carried away by the leptons, making the recoil energy of ^{20}Ne rather small. But the fact that the detected α -particles are emitted in motion results in a significant broadening of the measured spectrum.

In the rest frame of the β -decaying ^{20}Na nucleus, which coincides with the laboratory frame, the kinetic energy of the emitted α -particle can be expressed as

$$\begin{aligned} T &= \frac{1}{2}m_\alpha \mathbf{V}_\alpha^2 = \frac{1}{2}m_\alpha (\mathbf{v}' + \mathbf{v}_{\text{Ne}})^2 \\ &= \frac{1}{2}m_\alpha v'^2 + m_\alpha \mathbf{v}' \cdot \mathbf{v}_{\text{Ne}} + \frac{1}{2}m_\alpha v_{\text{Ne}}^2, \end{aligned} \quad (9.1)$$

where \mathbf{v}_α and \mathbf{v}' represents the velocity of an α -particle in the laboratory and recoil-reference frame, respectively, and \mathbf{v}_{Ne} is the velocity of the recoiling ^{20}Ne nucleus. The first term is the energy of the α -particle in the rest frame of the ^{20}Ne nucleus, while the two other terms are identified as kinematic shifts. The last term will be very small owing to the huge mass difference between ^{20}Ne and the β -particle. The second term on the other hand describes the main contribution to the kinematic shift. If α , β and ν are introduced as the momentum vectors for the α -particle, the β -particle and the neutrino, a quick calculation of the expected shift as function of excitation energy in ^{20}Ne (E^*) yields

$$\begin{aligned} \Delta K(E^*) &\approx m_\alpha \mathbf{v}' \cdot \mathbf{v}_{20\text{Ne}} = m_\alpha (v' \hat{\alpha}) \cdot \frac{\mathbf{p}_{\text{Ne}}}{M_{20\text{Ne}}} \\ &= - \left[\frac{2(E^* - E_{\text{thres.}}) m_\alpha (M_{20\text{Ne}} - m_\alpha)}{M_{20\text{Ne}}^3} \right]^{1/2} (\beta \hat{\alpha} \cdot \hat{\beta} + \nu \hat{\alpha} \cdot \hat{\nu}), \end{aligned} \quad (9.2)$$

where $\mathbf{p}_{20\text{Ne}} = -(\beta + \nu)$ and $v_{20\text{Ne}} = \frac{m_\alpha}{M_{20\text{Ne}}} \sqrt{\frac{2(M_{20\text{Ne}} - m_\alpha)}{m_\alpha M_{20\text{Ne}}}}$ result from momentum and energy conservation. Notice that the shift in energy of the α -particles is strongly dependent on the emission angle between the α -particle and both of the leptons. Consider for instance the situation in which both of these angles are 180° . In that case the kinematic shift will be largest, in accordance with the expectation that the α -particle will gain most energy when emitted in opposite direction to the leptons. Estimating the size of the shift for a β -decay to $E^* = 7.86 \text{ MeV}$, and assuming that the β receive all the released energy in the β -decay ($Q - E^*$), gives

$$\Delta K(7.86 \text{ MeV})_{\text{max}} \approx 39.8 \text{ keV}. \quad (9.3)$$

Aiming at determining accurate α -widths, a shift in energy of 40 keV needs to be corrected for. This will be described in the next section.

9.2.1 Recoil correction

The measured data has inevitably been subject to the recoil effect and therefore the theory must be enforced by the same effect before comparison is made. In doing so, the recoil distribution for all the energies of the α -spectrum must be known. A few issues regarding this will be discussed.

- In the measurement at hand no leptons were detected - only the α -particles. This means that the distribution of energy shifts can be determined from Eq. 5 in [Sch93], where averaging over all the lepton angles is done, or from a simulation. In this case a simulation program was used. Here the kinetic energy of the positron was chosen randomly from an uniform distribution (from 0 keV to $Q_\beta - E^*$), and the lepton angles were randomly chosen with respect to the direction of the α -particle in the recoil frame. From this, the remaining energies and momenta were calculated in a rigorously way.
- Correction was made for the shape of the β -spectrum by weighting events at a given energy with the phase space value at that energy [Kra88]¹:

$$f(E) = \sqrt{K_e^2 + 2K_e m_e c^2} (Q_\beta - K_e)^2 (K_e + m_e c^2),$$

where K_e is the kinetic energy of the electron.

- The kinematical shift depends on the directions of the α -, β - and ν -momenta as seen from (9.2). Any angular correlation between the leptons will therefore influence the shift distribution. In the case of a general β -transition the angular correlation between the leptons has the following probability distribution

$$W(\theta_{\beta\nu}) = 1 + a \frac{\beta}{E} \cos \theta_{\beta\nu}, \quad (9.4)$$

where β and E are the momentum and total energy of the positron, respectively, and a is the *angular correlation coefficient*. This coefficient probes the asymmetry of the weak force via β -decays. For a transition which is purely Fermi in nature a equals 1, and the probability distribution in Eq. 9.4 will peak at $\theta_{\beta\nu} = 0$. This behaviour is explained by the fact that Fermi transitions do not flip the quark spin, as discussed in Section 7.3.1, and consequently the lepton spin's must couple to zero demanding that they are emitted in the same direction. In the case of a pure Gamow-Teller transition $a = -\frac{1}{3}$. Fermi transitions thus favor larger kinematic shifts than to Gamow-Teller transitions.

An example of the simulated recoil broadening (Figure 9.1) shows the results from Fermi and Gamow-Teller decays to a single energy level. The simulated broadening shown in figure 9.1 for $E_\alpha = 2.5$ MeV corresponds to an excitation energy of

¹This simple form does not include Coulomb effects.

$4.730 \text{ MeV} + \frac{m_\alpha + m_{16\text{O}}}{m_{16\text{O}}} \cdot E_\alpha = 7.86 \text{ MeV}$, the same excitation energy used in Eq. 9.3 above. Estimating the maximum shift from Figure 9.1 reveals agreement between the simulation and the estimate for the largest possible shift (Eq. 9.3). The simulation generates a large matrix where each channel corresponds to an energy bin. Each matrix column describes how events in one channel are broadened. The theoretical spectrum, including the broadening effect, was obtained by folding the calculated R -matrix expression with this matrix. An example is shown in Figure 9.2 where the green curve corresponds to the recoil broadening of the calculated red curve.

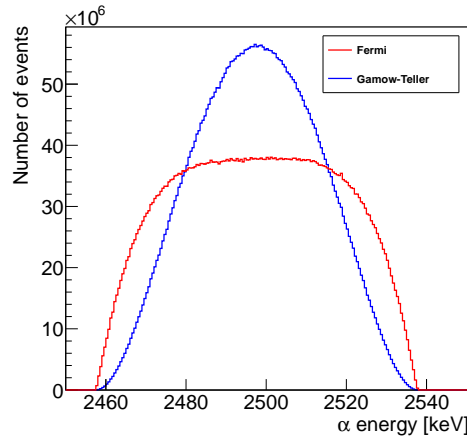


Figure 9.1: Simulation of the recoil distribution associated with Fermi (red curve) and Gamow-Teller (blue curve) β -decay. The example describes the broadening of α -particles with $E = 2.50 \text{ MeV}$ decaying from an excitation energy of $E^* = 7.86 \text{ MeV}$.

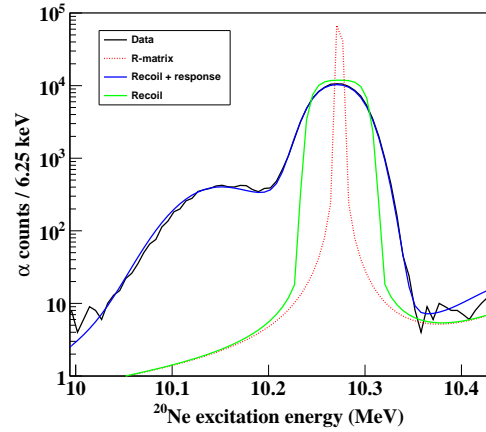


Figure 9.2: Example illustrating the implementation of recoil and response corrections. First the R -matrix expression is calculated, whereafter it is recoil (green curve) and response corrected (blue curve).

9.3 Response of the detection system

The measured spectrum is subject to response effects of the detection system, which must be dealt with carefully in order to extract precise and accurate physical parameters. In general the *response function* determines the measured energy distribution that results from a completely monoenergetic beam due to experimental effects of the detection system. How the response function is extracted from the data will be discussed below.

The response function is determined from a study of how α -decays from the IAS in ^{20}Ne are affected by the experimental conditions. The IAS is ideal for testing

experimental effects since its physical shape is well understood. This has to do with several circumstances:

- The IAS causes the second-most intense peak located at 4.434 MeV in the α spectrum, providing enough statistics for extracting a reliable response function from it.
- It has a very narrow width of $\Gamma < 0.3$ keV [Til98], which means that α -particles emitted from this level will serve as the monoenergetic beam mentioned above.
- The β -decay to the IAS is known to proceed mainly through a Fermi transition though it also has a small Gamov-Teller contribution [Cli89]. This implies that only minor interference between the IAS and nearby states will occur. This is so because contributions from states fed by Fermi and Gamow-Teller transitions do not interfere (see Eq. 8.17).
- The IAS is well separated from other states contributing to the spectrum, leaving disturbances from other levels is at a minimum.

These circumstances, and the fact that the spread in α -particle energies from the recoil motion can be understood analytically, makes the IAS the ideal choice for extracting the response function.

The broadening of α -particles energies due to recoil motion can be approximated by the following expression [Bha02]. Following the notation of [Kir11]:

$$\rho(x) = \begin{cases} \frac{5}{8\delta E_{\max}} (1 - x^4) & , -1 < x < 1 \\ 0 & , |x| > 1, \end{cases} \quad (9.5)$$

where $x = \frac{\delta E}{\delta E_{\max}}$ is the shift of the individual α -particle energies compared to the maximum shift possible,

$$\delta E_{\max} = \frac{m_e}{M_{20\text{Ne}}} \left[2Qm_\alpha c^2 (W_0^2 - 1) \frac{M_{20\text{Ne}}c^2 - m_\alpha c^2 - Q}{M_{20\text{Ne}}c^2 - Q} \right] = 29.9 \text{ keV}, \quad (9.6)$$

where m_e , m_α and $M_{20\text{Ne}}$ are the masses for the electron, the α particle and the recoiling daughter nucleus respectively. Q gives the excitation energy above the [$\alpha + {}^{16}\text{O}$] threshold energy, while $W_0 = \frac{E_0 - E^*}{m_e c^2}$, where $E_0 = 13375(7)$ keV is the maximum total energy of the emitted positron.

9.3.1 Parametrisation of response function

The response function used in this work consist of two terms, one containing a Gaussian and the other a Gaussian folded through a low energy exponential tail. The parameterization is inspired by the one used in [Bha06] and is expressed as

$$\psi(E_0, E) = \frac{A_1}{\sqrt{2\pi}\sigma} \exp\left(-\frac{(E-E_0)^2}{2\sigma^2}\right) + \frac{A_2}{2\lambda} \exp\left(-\frac{E-E_0}{\lambda} - \frac{\sigma^2}{2\lambda^2}\right) \times \operatorname{erfc}\left(\frac{E-E_0+\sigma^2/\lambda}{\sqrt{2}\sigma}\right), \quad (9.7)$$

where E is the energy variable and E_0 the observed energy of the peak. The exponential decay length of the tail is given by λ , erfc is the complementary error function and the coefficients A_1 and A_2 give the relative sizes of the two terms. The width of the Gaussian is given by σ .

The response function in the form of Eq. 9.7 needs to be modified in order to account for the satellite peaks. It cannot be assumed that the response function for ions striking the aluminum grid is the same as the one for those not striking the grid. In particular, the satellite peak is expected to have a larger width than the main peak. The full response function takes the form

$$\Psi(E_0, E) = (1-g)\psi(\sigma; E_0, E) + g\psi(\sigma_g; E_0 - E_g, E), \quad (9.8)$$

where E_g represents the mean energy loss in the aluminium, σ_g is the width of the satellite peak and g is the percentage at which the aluminium grid covers the detector area.

In order to perform a fit to the region around the IAS, the response function is folded with the recoil distribution (Eq. 9.5):

$$N(E_\alpha) = \int \Psi(E_0, E_\alpha - E) \rho(x(E_\alpha)) dE. \quad (9.9)$$

To sum up: the properties of the IAS and the ability to describe the recoil broadening of the α -particles provide sensitivity to the experimental effects via the parametrization for Ψ .

9.3.2 Response fitting

The α -particle spectrum around the IAS is fitted to Eq. 9.9. The result is shown in Figures 9.3 and 9.4 where the fit (red) is superimposed on the measured spectrum (black). In order to extract the response function as accurately as possible, the fit includes the low energy tail from the Gamow-Teller fed state at 10.587 MeV. The effect of the tail amounts to a small contribution, but noticeable. The tail contribution is added simply to Eq. 9.9 since Fermi and Gamow-Teller contributions do not interfere. Figure 9.9 shows the effects of including the Gamow-Teller tail (red) and not including it (blue), while Figure 9.4 display explicitly the main and the satellite peak components.

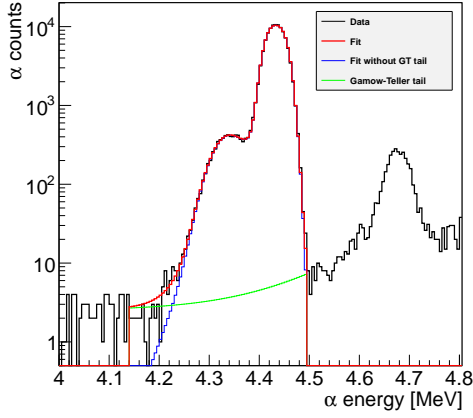


Figure 9.3: Response function fit with and without the Gamow-Teller background.

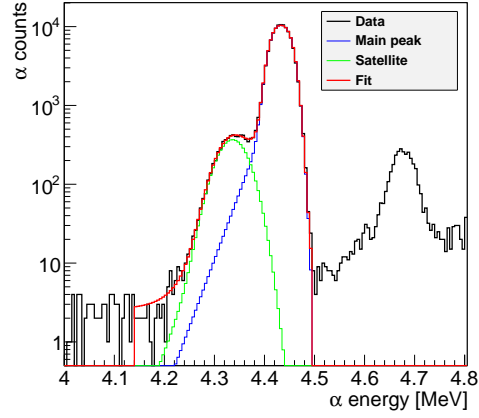


Figure 9.4: Final response function fit showing main and satellite contribution.

9.3.3 Generating response matrix

The final goal of the response analysis is the ability to broaden out the R -matrix spectrum before comparison to data is made. The result from the fit, as presented in Figures 9.3 and 9.4, determines the response of the detection system at an α -particle energy of 4.434 keV. Obtaining an expression for $\Psi(E_0, E)$, valid at any α -particle energy, some approximations are needed. We assume that the relative sizes of A_1 and A_2 in Eq. 9.7 are independent of energy. It is furthermore assumed that σ , the response width of the main peak, and λ are energy independent. The width, σ_g , of the satellite peak is scaled by a factor

$$\frac{\Delta E(E)}{\Delta E(E = 4.434 \text{ MeV})}, \quad (9.10)$$

where ΔE is the energy lost by α -particles in the Al grid. With this, Eq. 9.8 can be determined at any energy.

The satellite peak position is determined at a general α -particle energy by first converting the energy loss in the aluminum grid at 4.434 MeV to an equivalent thickness. This thickness is then used to calculate the energy loss in the grid for other α -particle energies. The thickness is determined as

$$\begin{aligned} \Delta x &= \int_0^{\Delta x} dx = - \int_{E_0}^{E_0 - \Delta E} \frac{dE}{S(E)} \\ &= \int_0^{E_0} \frac{dE}{S(E)} - \int_0^{E_0 - \Delta E} \frac{dE}{S(E)} = R(E_0) - R(E_0 - \Delta E), \end{aligned} \quad (9.11)$$

where the stopping power is defined as $\frac{dE}{dx} = -S(E)$. Here Δx and ΔE is the traversed distance and associated energy loss, respectively, of an incoming particle of energy E_0 . The ranges, $R(E)$, are evaluated by performing a spline to the range values tabulated in [Zie08].

9.4 Fitting procedure

The R -matrix fit is implemented using a C++ code originally developed for the analysis of data acquired on the decay of ${}^8\text{B}$. The recoil and response corrected R -matrix expression is fitted to the measured data in DSSSD 1 during the second ${}^{20}\text{Na}$ run using the model independent maximum likelihood estimator [Bak84]:

$$\chi_p^2 = 2 \sum_i \left(y_i - m_i + m_i \ln \left(\frac{m_i}{y_i} \right) \right), \quad (9.12)$$

where y_i is the theoretical prediction in bin i and m_i is the measured value. The sum runs over bins from 7 MeV to 12 MeV in excitation energies. The minimization is performed using the MINUIT2 package [Tea10] implemented within the ROOT framework [Bru97]. The MINOS method is used for error calculation.

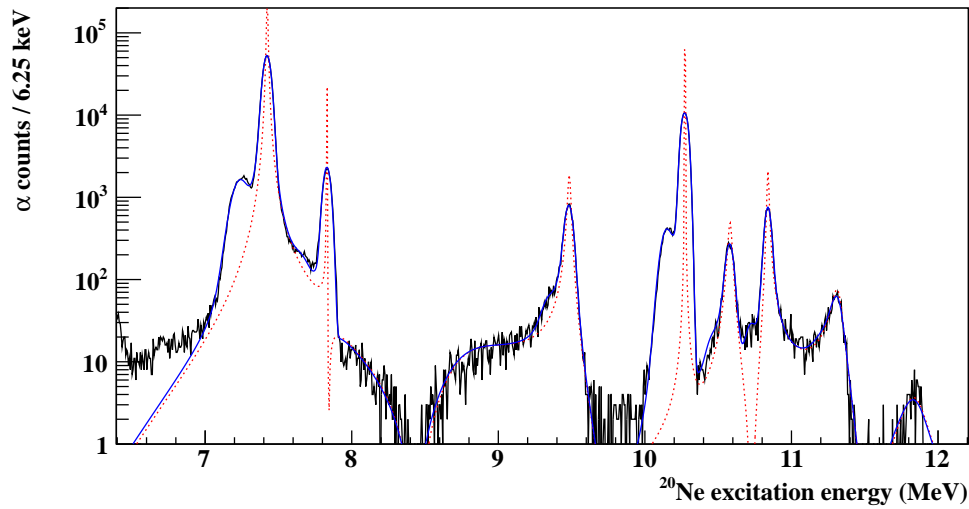


Figure 9.5: Best R -matrix fit. Black: data. Blue: fit. Red: R -matrix expression without broadening effects.

The ft values obtained in Ref. [Cli89] suggest that the transitions to the observed resonances are first forbidden or allowed, and hence the spin and parity of the observed resonances can be 1^- , 2^+ or 3^- . The observation of α decay from these states

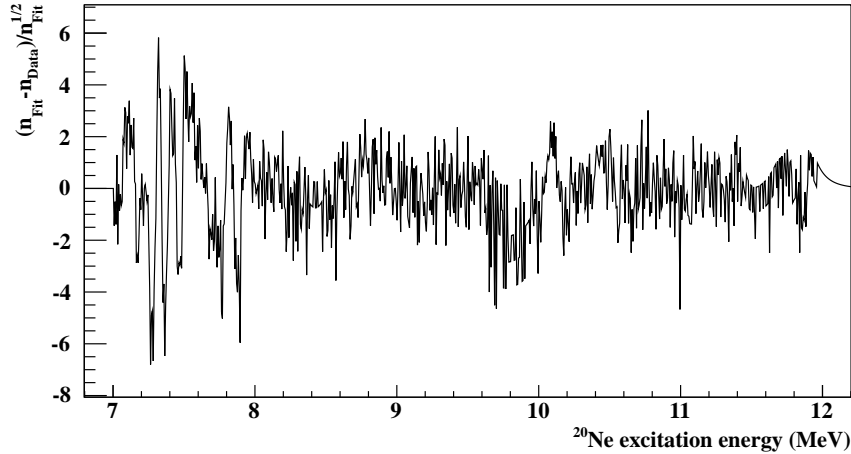


Figure 9.6: Fit residual showing the deviations between the fit and the measured data relative to the statistical error.

excludes unnatural spin and parity. The fitting procedure assumes to begin with the simplest possible fit, only including allowed transitions to resonances seen earlier in reaction experiments. All resonances are therefore assumed to have spin and parity 2^+ and interference occur naturally.

As starting point in the fitting procedure the fairly well known level energies are fixed whereas the more uncertain reduced α -widths and some β -strength parameters are left free. Eventually all parameters were varied except for the IAS reduced α -width, γ_9 , which in the literature has the upper limit $\Gamma_{\text{tot}} \leq 0.3 \text{ keV}$. Since the fitting routine is insensitive to such a small width, γ_9 was kept at $-6.09 \times 10^{-3} \sqrt{\text{MeV}}$ corresponding to $\Gamma_{\text{tot}} = 0.200 \text{ keV}$ throughout the minimization. This approach is necessary for an accurate extraction of Fermi transition matrix element, M_F .

The best fit is presented in Figure 9.5. The figure displays both the fitted R -matrix function Eq. 8.10 and the final fit curve obtained after convolution with the response function and the recoil broadening distribution. The fit residuals, presented in Figure 9.6, show a largest deviation between the data and the fit at the satellite shoulder of the most intense peak, dominating the rather high $\chi^2/\text{d.o.f.} = 2.21$. This deviation is caused by systematic errors in the propagation of the response function to other energies. The inability of the fit to describe the few events around 9.8 MeV is due to inaccurate modeling of the low-energy response tail of the IAS.

The overall quality of the fit is remarkably good in view of the complex nature of the spectrum. The fit includes 9 transitions to ^{20}Ne resonances and reproduce all significant structures. The detailed understanding of the spectrum is given in the

next chapter.

Results and discussion

In this final chapter the results obtained from the R -matrix fit (see Figure 9.5) are presented and discussed. The results can basically be divided in to two types, one type being the quantitative results for the extracted level parameters and the other being more qualitative concerning the interpretation of the measured resonance spectrum.

10.1 Results

Our observed level parameters are presented in Table 10.1. The uncertainties on the R -matrix parameters $\sigma(E_\lambda)$, $\sigma(\gamma_\lambda)$ and $\sigma(g_{\lambda,F/GT})$ were calculated by adding their individual errors in quadrature. The error originating from the response function was estimated by comparing fits using two different response functions: One that includes the low energy tail of the IAS and one that does not. The detailed error budget is as follows.

Energy parameters (E_λ): Errors on E_λ from the energy calibration range from 1.4 keV to 3.0 keV while the statistical fit errors range from 2×10^{-3} keV to 4.5 keV. The response function errors on E_λ are in general small but relatively large for levels 7 and 13.

Reduced width parameters (γ_λ): The response errors dominate since the reduced widths are highly sensitive to the detector response. The errors are around $2-4 \times 10^{-3} \sqrt{\text{keV}}$ for all levels except level 7 for which it is $2 \times 10^{-2} \sqrt{\text{keV}}$. The statistical errors are at the $10^{-3} \sqrt{\text{keV}}$ level. The uncertainty on $\Gamma_{\text{tot},\lambda}$ is found directly by combining $\sigma(\gamma_\lambda)$ and Eq. 8.14.

β -strength parameters ($g_{\lambda,G/FT}$): The statistical errors dominate giving contributions around 10^{-3} for all levels apart from levels 6, 12 and 13 where they are one order of magnitude larger. The uncertainty on $B_{F/GT}$ is obtained through propagation of errors in Eq. 8.19 where $\sigma(BR_\alpha)$ is the dominating source of uncertainty.

The two columns of measured $B_{GT/F}$ values in Table 10.1 represent two different ways of extraction. The first one (4th column) uses the method specified by Eq. 8.19. Since no internal normalization is possible in this experiment, the normalization constant in Eq. 8.19 is determined by integrating the decay probability (Eq. 8.9) over the full spectrum and equating it to the branching ratio to α -emitting states

Table 10.1: Results extracted from R-matrix fit.

No.	This work				Ref. [Til98]		Ref. [Cli89]
	E[MeV]	Γ [keV]	$B_{GT/F}^a$	$B_{GT/F}^b$	E[MeV]	Γ [keV]	$B_{GT/F}$
2	7.4227(15)	10.0(5)	0.246(4)	0.248(1)	7.4219(12)	15.1(7)	0.240(8)
3	7.8301(14)	0.18(8)	0.017(7)	0.0133(8)	7.8334(15)	2	0.0126(5)
5	8.77(2)	686(56)	0.00230(7)	0.0025(2)	9.00(18)	800	0.008(12)
6	9.4927(19)	35(3)	0.0329(8)	0.034(1)	9.483(3)	29(15)	0.032(2)
7	10.274(2)	0.200	1.95(3)	1.99(3)	10.2732(19)	≤ 0.300	1.28(7)
8	10.587(2)	34(2)	0.069(2)	0.067(3)	10.584(5)	24	0.067(5)
9	10.842(2)	16.4(5)	0.258(5)	0.250(11)	10.843(4)	13	0.224(15)
12	11.331(3)	85(6)	0.127(4)	0.149(7)	11.320(9)	40(10)	0.101(14)
13	11.89(5)	252(7)	0.11(10)	0.063(1)	11.885(7)	46	0.039(19)

^a Calculated by use of 8.19.

^b Calculated by use of 7.3.

$BR_\alpha = 20.05 \pm 0.36$. The second method (5th column) involves direct counting of events and calculation from Eq. 7.3. The $B_{GT/F}$ results in column 4 serve as the our recommended values, while those in column 5 constitute a consistency check. The $B_{GT/F}$ values from [Cli89] in column 5 are deduced from their reported ft values.

10.2 Discussion

Our values for the level parameter are now discussed and compared to literature values. Our interpretation results in a new and improved understanding of the ^{20}Ne excitation spectrum.

The energy positions of levels 2, 7, 8, 9, 12 and 13 found in this work are in agreement with the literature values within one standard deviation. Levels 3, 5 and 6 differ slightly more. This discrepancy may be due to the clear interference effects in the region from 7.5 MeV to 9.5 MeV.

The literature widths in Table 10.1 are total widths and many of them are quite uncertain in which case a quantitative comparison to our values is not possible. For levels 2, 5, 6, 8, 9 and 12 our widths are more precise than the literature ones. The width of level 2 differs significantly from the one in [Til98] but agrees well with a newer value of 9.0(13) keV [Cos10]. In the case of level 3 the value of 180(80) eV is too small to be trusted and our poor determination for level 13 is attributed to the low level of statistics in this part of the experimental spectrum.

The determined $B_{F/GT}$ agree within one standard deviation with the those derived

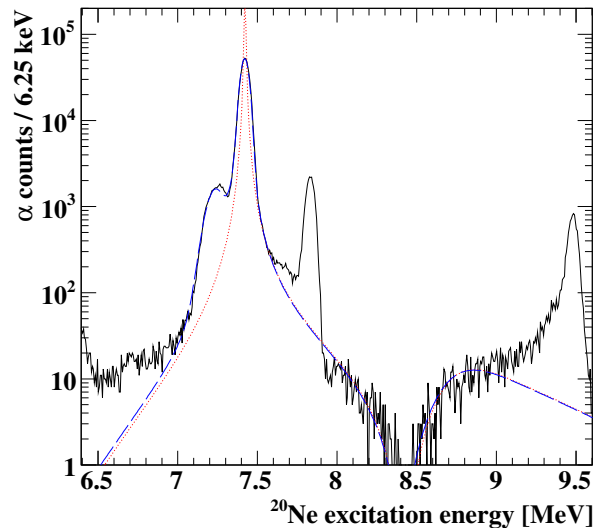


Figure 10.1: R -matrix fit including only levels 2 and 5..

from [Cli89] for levels 2, 3, 6 and 8. Level 7 nearly agrees. The large difference for level 13 is again ascribed to the few events collected in that region while the disagreement for levels 5, 7, 9 and 12 largely has to do with our reinterpretation of the α -spectrum.

The levels included in the best fit are number 2, 3, 5, 6, 7, 8, 9, 12, 13 (see figure 7.6) where the present interpretation of level number 5 is different from the one in [Cli89]. Notice that levels 10 and 11, proposed in [Cli89] and not seen in any reaction studies, does not figure in the best fit. These are in no way necessary to describe the distribution between peak 9 and 12, which instead is explained by positive interference between contributions from the levels corresponding to peak 9 and 12. This finding illustrate the importance of interference in the β -delayed spectrum, an effect that was ignored in [Cli89].

The most striking structure in the broad spectrum is broad distribution at 8-9 MeV. In [Cli89] this structure was explained by introducing two new levels at 8.058 MeV and 9.196 MeV. They mention the possibility that the interference between the 9.196 MeV level and another level could be responsible for the observed effect. The present analysis does not include a level at 8.058 MeV, but instead the characteristic structure is described as destructive interference between levels 2 and 5. This remarkable fact is illustrated in Figure 10.1, where only transitions to these two levels have been included in the R -matrix fit. The minimum at ~ 8.5 MeV is clearly caused by interference.

In [Cli89] it is briefly mentioned that the level identified by them at 9.196 MeV

could possibly be identical to a known level at 8.800 MeV. Indeed a 2^+ level at this energy has been observed in $^{16}\text{O}(\alpha, \alpha)$ [McD60] and $^{19}\text{F}(^3\text{He}, d)$ [For76] reaction experiments. Later an inelastic pion scattering experiment observed the same level at 9.0(2) MeV with $\Gamma = 0.8$ MeV identifying it as the 2^+ member of the 0_4^+ rotational band in ^{20}Ne . Our result gives the most precise observation of the 2_4^+ level and its first conclusive observation in β -decay.

As an additional note it is interesting that the R -matrix work done in [Cos10] does not include the 2_4^+ resonance. The inclusion of this resonance might influence the extrapolated S -factor for the $^{16}\text{O}(\alpha, \gamma)^{20}\text{Ne}$ reaction as its broad nature could facilitate a non-resonant contribution.

10.2.1 IAS properties

Our high statistics results give, in combination with earlier experiments, improved information of the IAS. Our results on the IAS are divided into three groups. 1. The fraction of α -particles coming from the IAS $I_\alpha^{\text{IAS}}/I_\alpha^{\text{Tot}}$. 2. Determination of $\Gamma_\alpha^{\text{IAS}}/\Gamma_{\text{Tot}}^{\text{IAS}}$ in two different ways. 3. Absolute value for the IAS α -particle width $\Gamma_\alpha^{\text{IAS}}$.

The first result, the fraction of β -delayed α -decays from the IAS, is best estimated from the single α -particle spectrum. This is done by including the intensity above 1.5 MeV and correcting for the slight variation as function of energy of the singles α -particle detection efficiency. This variation has been determined in [Kir11]. In general the systematic uncertainty dominate and has been estimated by varying the lower cut by ± 100 keV around 1.5 MeV and by varying the integration region around the IAS with ± 40 keV. Each DSSSD give an independent value for the ratio. The four values are consistent and lead to a new value of $I_\alpha^{\text{IAS}}/I_\alpha^{\text{Tot}} = 0.1391(5)$, which compared to the previous value 0.1386(33) [Cli89] is more precise.

Next, our observed value for the β strength, B_F in Table 10.1, can be used to extract the α -particle branching ratio $\Gamma_\alpha^{\text{IAS}}/\Gamma_{\text{Tot}}^{\text{IAS}}$ for the IAS. This is done by realizing that the *observed* value for B_F , called $B_{\beta-\alpha}$ from here on, is the total $\alpha - \beta$ strength, which is given as a product of $[B_F + \frac{g_A^2}{g_V^2} B_{GT}]$ (see Eq. 7.3), and the branching ratio we seek. Utilizing that the Fermi strength is $B_F = 2(1 - \delta_c)$, where δ_c is a correction factor coming from theory [Cli89], will in combination with the measured Gamow-Teller to Fermi strength give the α -particle branching ratio. The latter is quantified in terms of the triple-correlation coefficient

$$a_3 = \frac{\frac{g_V^2}{g_A^2} B_F - B_{GT}}{\frac{g_V^2}{g_A^2} B_F + B_{GT}}, \quad (10.1)$$

which is measured to 0.79(9) in [Cli89]. Using this, the branching ratio is calculated as

$$\begin{aligned}\frac{\Gamma_{\alpha}^{\text{IAS}}}{\Gamma_{\text{Tot}}^{\text{IAS}}} &= \frac{B_{\beta-\alpha}}{B_F + \frac{g_A^2}{g_V^2} B_{GT}} \\ &= \frac{B_{\beta-\alpha}}{B_F \left(1 + \frac{1-a_3}{1+a_3}\right)},\end{aligned}\quad (10.2)$$

where the denominator in the first expression gives the total decay strength to the IAS, including both Fermi and Gamow-Teller strengths (compare to Eq. 7.3). We get $\Gamma_{\alpha}^{\text{IAS}}/\Gamma_{\text{Tot}}^{\text{IAS}} = 0.92(3)$.

The α -particle branching ratio can alternatively be determined from our value for $I_{\alpha}^{\text{IAS}}/I_{\alpha}^{\text{Tot}}$ (determined above) and some experimental results on γ -decays in ^{20}Ne . Writing down the definition of $I_{\alpha}^{\text{IAS}}/I_{\alpha}^{\text{Tot}}$ and doing some manipulations give

$$\begin{aligned}\frac{\Gamma_{\alpha}^{\text{IAS}}}{\Gamma_{\text{Tot}}^{\text{IAS}}} &= \frac{I_{\alpha}^{\text{IAS}}}{I_{\alpha}^{\text{IAS}} + I_{\gamma}^{\text{IAS}}} = \frac{1}{1 + \frac{I_{\gamma}^{\text{IAS}}}{I_{\alpha}^{\text{IAS}}}} \\ &= \left[1 + \frac{I_{\gamma \rightarrow 1.63}^{\text{IAS}} \frac{\Gamma_{\gamma \rightarrow 1.63}^{\text{IAS}}}{I_{\alpha}^{\text{IAS}}}}{I_{\alpha}^{\text{IAS}}}\right]^{-1} = \left[1 + \left(\frac{I_{\gamma \rightarrow 1.63}^{\text{IAS}}}{I_{\gamma(1.63)}} \cdot \frac{I_{\gamma(1.63)}}{I_{\alpha}^{\text{Tot}}} \cdot \frac{I_{\alpha}^{\text{Tot}}}{I_{\alpha}^{\text{IAS}}}\right) \cdot \frac{\Gamma_{\gamma}^{\text{IAS}}}{\Gamma_{\gamma \rightarrow 1.63}^{\text{IAS}}}\right]^{-1},\end{aligned}$$

where $I_{\gamma \rightarrow 1.63}^{\text{IAS}}/I_{\gamma(1.63)}$ is the relative intensity of IAS transitions to the first excited state in ^{20}Ne at 1.63 MeV to the total number of 1.63 MeV γ -rays, $I_{\alpha}^{\text{Tot}}/I_{\gamma(1.63)}$ is the total number of α -particles to the number 1.63 MeV γ -rays, $I_{\alpha}^{\text{IAS}}/I_{\alpha}^{\text{Tot}}$ is the value measured in this work (see above) and $\Gamma_{\gamma \rightarrow 1.63}^{\text{IAS}}/\Gamma_{\gamma}^{\text{IAS}}$ is the γ branching ratio for IAS decay to the 1.63 MeV state. The values for these quantities are listed in Table 10.2, and finally we get $\Gamma_{\alpha}^{\text{IAS}}/\Gamma_{\text{Tot}}^{\text{IAS}} = 0.961(5)$, a value more precise than the above one. The literature value for $\Gamma_{\alpha}^{\text{IAS}}/\Gamma_{\text{Tot}}^{\text{IAS}}$, deduced from the listed $\Gamma_{\alpha}^{\text{IAS}}$ and $\Gamma_{\gamma}^{\text{IAS}}$ values [Ti98], is found to 0.965(6) in agreement with our second and most precise value.

These relative measurements is put on an absolute scale by including the measurements of the α -particle radiative capture trough the IAS to the 1.63 MeV state [Ing76, Fif77, Ste78], which give an average value of resonance strength [Ti98]:

$$\omega\gamma = (2J + 1) \frac{\Gamma_{\gamma \rightarrow 1.63}^{\text{IAS}} \Gamma_{\alpha}^{\text{IAS}}}{\Gamma_{\text{Tot}}^{\text{IAS}}} = 19.5(1.5) \text{ eV}, \quad (10.3)$$

Where $J = 2$ in the case of ^{20}Ne . The total width of the IAS can then be calculated, which after some manipulation is done as

Table 10.2: Properties for the IAS in ^{20}Ne obtained from results in the this work in combination with results from earlier studies. The bottom part of the table lists the relative quantities used for the calculations.

$I_{\alpha}^{\text{IAS}}/I_{\alpha}^{\text{Tot}}$	$\Gamma_{\alpha}^{\text{IAS}}/\Gamma_{\text{Tot}}^{\text{IAS}}$		$\Gamma_{\text{Tot}}^{\text{IAS}}$ [eV]
	Method 1	Method 2	
0.1386(33)	0.92(3)	0.961(5)	116(20)
$I_{\gamma \rightarrow 1.63}^{\text{IAS}}/I_{\gamma(1.63)}^{\text{Tot}}$ [Ing76]	$I_{\alpha}^{\text{Tot}}/I_{\gamma(1.63)}^{\text{Tot}}$ [Cli89]	$I_{\alpha}^{\text{IAS}}/I_{\alpha}^{\text{Tot}}$	$\Gamma_{\gamma \rightarrow 1.63}^{\text{IAS}}/\Gamma_{\gamma}^{\text{IAS}}$ [Fif77]
0.00126(16)	0.2497(42)	0.1391(5)	0.889(5)

$$\begin{aligned}
 \Gamma_{\text{Tot}}^{\text{IAS}} &= \Gamma_{\gamma}^{\text{IAS}} + \Gamma_{\alpha}^{\text{IAS}} \\
 &= \left[\frac{\Gamma_{\gamma \rightarrow 1.63}^{\text{IAS}}}{\Gamma_{\gamma}^{\text{IAS}}} \right]^{-1} \cdot \frac{\omega\gamma}{2J+1} \cdot \left(\frac{1}{1 - \frac{\Gamma_{\alpha}^{\text{IAS}}}{\Gamma_{\text{TOT}}^{\text{IAS}}}} + \left[\frac{\Gamma_{\alpha}^{\text{IAS}}}{\Gamma_{\text{TOT}}^{\text{IAS}}} \right]^{-1} \right). \quad (10.4)
 \end{aligned}$$

We get a value of 116(20) eV justifying the value of 200 keV used in the R -matrix fit. All the results obtained on the IAS properties are listed in Table 10.2.

10.3 Conclusion

The high level of statistics gathered in the present experiment allowed for an R -matrix analysis of the interference features seen in the β -delayed α spectrum around 3 MeV and 5 MeV. The spectrum turns out to be describable in terms of levels that all have been seen in reaction experiments. Compared to earlier β -decay studies we remove three suggested levels, but confirm conclusively β feeding to the broad state close to 9 MeV excitation energy in ^{20}Ne . The large width of this state suggests a pronounced $\alpha + ^{16}\text{O}$ cluster structure; our analysis gives improved values for its energy and width.

Solving for the collision matrix

As pointed out in Section 8.1, the physics of a given process that one wants to describe is contained in the collision matrix U . When derived, it will explicitly contain contributions from the levels λ . The derivation of U is lengthy and in this appendix a brief review will be presented with special emphasis on the key ideas. These include implementation of the boundary condition and matching between the outer and inner region.

Multiplying X_λ^* on Eq. 8.6 on page 117 and Ψ on the complex conjugate of (8.7) and subtracting these two gives

$$(E_\lambda - E) X_\lambda^* \Psi = (H X_\lambda)^* \Psi - X_\lambda^* H \Psi. \quad (\text{A.1})$$

Inserting the Hamiltonian $\frac{\hbar^2}{2\mu} \frac{d^2}{dr^2} + V$, and assuming $V^* = V$, the following expression is obtained when integrating over the volume, τ , of the inner region:

$$\begin{aligned} (E_\lambda - E) \int_\tau X_\lambda^* \Psi \, d\tau &= \int_\tau \{ (H X_\lambda)^* \Psi - X_\lambda^* H \Psi \} \, d\tau \\ &= \int_\tau \left\{ \left[\left(-\frac{\hbar^2}{2\mu} \frac{d^2}{dr^2} + V \right) X_\lambda \right]^* \Psi - X_\lambda^* \left(-\frac{\hbar^2}{2\mu} \frac{d^2}{dr^2} + V \right) \Psi \right\} \, d\tau \\ &= \frac{\hbar^2}{2\mu} \int_\tau \left\{ X_\lambda^* \frac{d^2}{dr^2} \Psi - \left(\frac{d^2}{dr^2} X_\lambda \right)^* \Psi \right\} \, d\tau. \end{aligned} \quad (\text{A.2})$$

Notice that the expansion coefficients can be written as

$$\Psi = \sum_\lambda C_\lambda X_\lambda \Rightarrow C_\lambda = \int_\tau X_\lambda^* \Psi \, d\tau, \quad (\text{A.3})$$

where the identity has been inserted. Converting the volume integral on the right hand side of (A.2) into a surface integral, by use of Greens theorem, C_λ can be rewritten as

$$C_\lambda = \frac{\hbar^2}{2\mu(E - E_\lambda)} \int_S \left\{ X_\lambda^* \frac{d}{dr} \Psi - \left(\frac{d}{dr} X_\lambda \right)^* \Psi \right\} \, dS. \quad (\text{A.4})$$

Remember the overall goal is to determine the collision matrix. We are not interested in solving Eq. 8.6 directly, because its very difficult, but rather to relate the

external and internal wave functions to each other and thereby gain nuclear information through the collision matrix. This matching is therefore central to the R -matrix theory and will be done at the surface between the internal and external region by equating the wave function Ψ , appearing in Eq. A.4, with $\Psi = \sum_c \psi_c u_c$ in the outer region:

$$C_\lambda = \frac{\hbar^2}{2\mu(E - E_\lambda)} \sum_c \int_S \left\{ X_\lambda^* \psi_c \frac{du_c}{dr} - \left(\frac{d}{dr} X_\lambda \right)^* \psi_c u_c \right\} dS. \quad (\text{A.5})$$

Acting with the boundary condition (Eq. 8.8) gives the following

$$\begin{aligned} C_\lambda &= \frac{\hbar^2}{2\mu(E - E_\lambda)} \sum_c \int_S \left\{ X_\lambda^* \psi_c \frac{du_c}{dr} - \frac{B_c}{a_c} X_\lambda^* \psi_c u_c \right\} dS. \\ &= \sum_c \frac{\hbar^2}{2\mu a_c (E - E_\lambda)} \left\{ a_c \frac{du_c}{dr} \Big|_{a_c} - B_c u_c(a_c) \right\} \int_S X_\lambda^* \psi_c dS. \\ &= \sum_c \left(\frac{\hbar^2}{2\mu a_c} \right)^{1/2} \frac{\gamma_{\lambda c}}{E_\lambda - E} \left(a_c \frac{du_c}{dr} \Big|_{a_c} - B_c u_c(a_c) \right), \end{aligned} \quad (\text{A.6})$$

where the definition of the reduced width is used. The reduced width is defined as

$$\gamma_{\lambda c} = \left(\frac{\hbar^2}{2\mu a_c} \right)^{1/2} \int_S X_\lambda^* \psi_c dS, \quad (\text{A.7})$$

and constitutes a measure of the overlap between the inner state λ and the state ψ_c in one of the outer channels, making it a key factor in determining the width of the resonances in question. Note that all quantities which are constant at the boundary surface have been dragged outside the integral in Eq. A.6.

Next "trick" is to multiply $\psi_{c'}^*$ on the expression $\Psi = \sum_c C_\lambda X_\lambda$ and integrate over the boundary

$$\int_S \psi_{c'}^* \Psi dS = \sum_\lambda C_\lambda \int_S \psi_{c'}^* X_\lambda dS. \quad (\text{A.8})$$

The prime on the channel index can be seen as representing e.g. the entrance channel while the un-primed c represents the exit channel. This equation is made out of three quantities, the C_λ 's and the two surface integrals. The expansion coefficients was worked out in Eq. A.6, which will become useful. Next, concerning the integral on the left, it can be shown by orthonormality of the channel wave functions that $\int_S \psi_{c'}^* \Psi dS = u_{c'}(a_{c'})$. It is also recognised that the integral on the right hand side is related to the reduced width $\gamma_{\lambda c'}$:

$$\int_S \psi_{c'}^* X_\lambda dS = \left(\frac{\hbar^2}{2\mu a_{c'}} \right)^{-1/2} \gamma_{\lambda c'}. \quad (\text{A.9})$$

Inserted all this to Eq. A.8 gives, after a few manipulations, the following expression for $u_{c'}(a_{c'})$:

$$\begin{aligned} \int_S \psi_{c'}^* X_\lambda dS = u_{c'}(a_{c'}) &= \sum_c \left(\frac{a_{c'}}{a_c} \right)^{1/2} R_{c'c} \left[a_c \frac{du_c}{dr} \Big|_{a_c} - B_c u_c(a_c) \right] \\ &= \sum_c \left(\frac{a_{c'}}{a_c} \right)^{1/2} R_{c'c} [u'_c - B_c u_c(a_c)], \end{aligned} \quad (\text{A.10})$$

where, as common in the R -matrix literature, the prime on u'_c denote the dimensionless derivative $r \frac{d}{dr}$. The quantity $R_{c'c}$ is called the R -matrix and is defined as

$$R_{c'c} = \sum_\lambda \frac{\gamma_{\lambda c'} \gamma_{\lambda c}}{E_\lambda - E}. \quad (\text{A.11})$$

Now to determine the collision matrix, the solution for the radial wave function Eq. 8.4 on page 116 is first inserted in terms of the outgoing and incoming waves, which after some manipulations give

$$\sum_c \frac{1}{\sqrt{\rho_c}} O_c \left[\delta_{c'c} - R_{c'c} \left(\frac{O'_c}{O_c} - B_c \right) \right] x_c = - \sum_c \frac{1}{\sqrt{\rho_c}} I_c \left[\delta_{c'c} - R_{c'c} \left(\frac{I'_c}{I_c} - B_c \right) \right] y_c, \quad (\text{A.12})$$

where $\rho_c = \frac{\mu_c v_c a_c}{\hbar}$. Comparing with Eq. 8.5 on page 116 gives the collision matrix. The collision matrix will have dimensions equal to the number of channels in the given problem and in order to calculate it, it is needed to divided by

$$\left[\delta_{c'c} - R_{c'c} \left(\frac{O'_c}{O_c} - B_c \right) \right], \quad (\text{A.13})$$

which is a channel matrix. This matrix therefore has to be inverted - one of the computational drawbacks of R -matrix theory.

In the analysis presented in this work an alternative form of the collision matrix is used, namely one where the collision matrix is given in the form of a level matrix, $A_{\lambda\mu}$, with dimensions equal to the number of levels in the given problem. It can be shown [Vog12] that it has the form

$$U_{c'c} = e^{i(\Omega_c + \Omega_{c'})} \left[\delta_{c'c} + 2i P_{c'}^{1/2} P_c^{1/2} \sum_{\lambda\mu} \gamma_{\lambda c'} \gamma_{\mu c} A_{\lambda\mu} \right], \quad (\text{A.14})$$

where Ω is the sum of the Coulomb phase shift and the hard sphere phase shift and the inverse of the level matrix, which therefore needs to be inverted, is given as

$$A_{\lambda\mu}^{-1} = \delta_{\lambda\mu} (E_\lambda - E) - \sum_c \gamma_{\lambda c} \gamma_{\mu c} (S_c - B_c + iP_c). \quad (\text{A.15})$$

S_c and P_c are the shift and penetration functions defined from the regular and irregular Coulomb functions

$$S_c = \rho_c \frac{\left[F_c \frac{dF_c}{d\rho_c} + G_c \frac{dG_c}{d\rho_c} \right]}{F_c^2 + G_c^2} \quad (\text{A.16})$$

$$P_c = \frac{\rho_c}{F_c^2 + G_c^2}. \quad (\text{A.17})$$

The collision matrix (Eq. A.14) is not directly observed, one instead calculates the cross section from $U_{c'c}$ as e.g. done in [Lan58b].

Bibliography

- [Ä01] J. Äystö, *Development and applications of the IGISOL technique*. Nuclear Physics A, **693**, 477 – 494 (2001), radioactive Nuclear Beams, URL <http://www.sciencedirect.com/science/article/pii/S037594740100923X>. 111
- [Ade77] E. G. Adelberger, R. E. Marrs, K. A. Snover and J. E. Bussolletti, *Radiative transitions and isospin mixing in ^{12}C* . Phys. Rev. C, **15**, 484–497 (1977), URL <http://link.aps.org/doi/10.1103/PhysRevC.15.484>. 42, 43, 93, 94, 99, 163, 164
- [Alc12] M. Alcorta *et al.*, *Properties of ^{12}C resonances determined from the $^{10}\text{B}(^3\text{He}, p\alpha\alpha)$ and $^{11}\text{B}(^3\text{He}, d\alpha\alpha)$ reactions studied in complete kinematics*. Phys. Rev. C, **86**, 064306 (2012), URL <http://link.aps.org/doi/10.1103/PhysRevC.86.064306>. 16, 91, 93
- [Ang99] C. Angulo *et al.*, *A compilation of charged-particle induced thermonuclear reaction rates*. Nuclear Physics A, **656**, 3 – 183 (1999), URL <http://www.sciencedirect.com/science/article/pii/S0375947499000305>. 14
- [AR08] R. Álvarez-Rodríguez, A. S. Jensen, E. Garrido, D. V. Fedorov and H. O. U. Fynbo, *Momentum distributions of α particles from decaying low-lying ^{12}C resonances*. Phys. Rev. C, **77**, 064305 (2008), URL <http://link.aps.org/doi/10.1103/PhysRevC.77.064305>. 92
- [AS90] F. Ajzenberg-Selove, *Energy levels of light nuclei $A = 11 - 12$* . Nuclear Physics A, **506**, 1–158 (1990), URL <http://www.sciencedirect.com/science/article/pii/037594749090271M>. 15, 35, 43, 93, 97, 99, 164
- [Aus99] S. M. Austin, *Nuclear physics and supernovae*. Nuclear Physics A, **649**, 279 – 287 (1999), giant Resonances, URL <http://www.sciencedirect.com/science/article/pii/S0375947499000731>. 15
- [Aus14] S. M. Austin, C. West and A. Heger, *Effective Helium Burning Rates and the Production of the Neutrino Nuclei*. Phys. Rev. Lett., **112**, 111101 (2014), URL <http://link.aps.org/doi/10.1103/PhysRevLett.112.111101>. 15
- [Bak84] S. Baker and R. D. Cousins, *Clarification of the use of CHI-square and likelihood functions in fits to histograms*. Nuclear Instruments and Methods in Physics

- Research, **221**, 437 – 442 (1984), URL <http://www.sciencedirect.com/science/article/pii/0167508784900164>. 128
- [Bal74] D. P. Balamuth, R. W. Zurmühle and S. L. Tabor, *Isospin-forbidden alpha decay of the 15.11-MeV state in ^{12}C* . Phys. Rev. C, **10**, 975–986 (1974), URL <http://link.aps.org/doi/10.1103/PhysRevC.10.975>. 19, 30
- [Bar62] F. Barker and P. Treacy, *Nuclear levels near thresholds*. Nuclear Physics, **38**, 33 – 49 (1962), URL <http://www.sciencedirect.com/science/article/pii/0029558262910143>. 17
- [Bar88] F. Barker and E. Warburton, *The beta-decay of 8He* . Nuclear Physics A, **487**, 269 – 278 (1988), URL <http://www.sciencedirect.com/science/article/pii/0375947488906136>. 117, 119, 120
- [Bet38] H. A. Bethe and C. L. Critchfield, *The Formation of Deuterons by Proton Combination*. Phys. Rev., **54**, 248–254 (1938), URL <http://link.aps.org/doi/10.1103/PhysRev.54.248>. 11
- [Bet39] H. A. Bethe, *Energy Production in Stars*. Phys. Rev., **55**, 434–456 (1939), URL <http://link.aps.org/doi/10.1103/PhysRev.55.434>. 11, 12
- [Bha02] M. Bhattacharya and E. G. Adelberger, *Reanalysis of $\alpha+\alpha$ scattering and the β -delayed α spectra from ^8Li and ^8B decays*. Phys. Rev. C, **65**, 055502 (2002), URL <http://link.aps.org/doi/10.1103/PhysRevC.65.055502>. 125
- [Bha06] M. Bhattacharya, E. G. Adelberger and H. E. Swanson, *Precise study of the final-state continua in ^8Li and ^8B decays*. Phys. Rev. C, **73**, 055802 (2006), URL <http://link.aps.org/doi/10.1103/PhysRevC.73.055802>. 125
- [Bie53] L. C. Biedenharn and M. E. Rose, *Theory of Angular Correlation of Nuclear Radiations*. Rev. Mod. Phys., **25**, 729–777 (1953), URL <http://link.aps.org/doi/10.1103/RevModPhys.25.729>. 25, 79
- [Bij00] R. Bijker and F. Iachello, *Cluster states in nuclei as representations of a $U(\nu + 1)$ group*. Phys. Rev. C, **61**, 067305 (2000), URL <http://link.aps.org/doi/10.1103/PhysRevC.61.067305>. 100
- [Boe05] A. M. Boesgaard, C. P. Deliyannis and A. Steinhauer. The Astrophysical Journal, **621**, 991 (2005). 34
- [Bra03] B. H. Bransden and C. J. Joachain, *Physics of Atoms and Molecules*. Pearson Education Limited (2003). 116

- [Bri67] D. Brink and E. Boeker, *Effective interactions for Hartree-Fock calculations*. Nuclear Physics A, **91**, 1 – 26 (1967), URL <http://www.sciencedirect.com/science/article/pii/0375947467904460>. 6, 7, 155
- [Bro65] J. Bronson, W. Simpson, W. Jackson and G. Phillips, *Three α -particle decay of C12*. Nuclear Physics, **68**, 241 – 269 (1965), URL <http://www.sciencedirect.com/science/article/pii/0029558265906437>. 30, 34
- [Bru97] R. Brun and F. Rademakers, *ROOT - An Object Oriented Data Analysis Framework*. Nucl. Inst. & Meth. in Phys. Res. A, **389**, 81–86 (1997). 59, 80, 128
- [Bru03] C. Brune, *An alternative parameterization of R-matrix theory*. Nuclear Physics A, **718**, 472 – 474 (2003), URL <http://www.sciencedirect.com/science/article/pii/S0375947403008601>. 119
- [Buc95] B. Buck, J. C. Johnston, A. C. Merchant and S. M. Perez, *Unified treatment of scattering and cluster structure in α -closed shell nuclei: ^{20}Ne and ^{44}Ti* . Phys. Rev. C, **52**, 1840–1844 (1995), URL <http://link.aps.org/doi/10.1103/PhysRevC.52.1840>. 105, 106, 160
- [Bur89] M. Burlein *et al.*, *Pion inelastic scattering to the low-lying broad 2^+ in ^{20}Ne* . Phys. Rev. C, **40**, 785–789 (1989), URL <http://link.aps.org/doi/10.1103/PhysRevC.40.785>. 113
- [Byc73] E. Byckling and K. Kajantie, *Particle Kinematics*. Wiley-Interscience, England (1973). 29
- [Che07] M. Chernykh, H. Feldmeier, T. Neff, P. von Neumann-Cosel and A. Richter, *Structure of the Hoyle State in ^{12}C* . Phys. Rev. Lett., **98**, 032501 (2007), URL <http://link.aps.org/doi/10.1103/PhysRevLett.98.032501>. 9
- [Che10] M. Chernykh, H. Feldmeier, T. Neff, P. von Neumann-Cosel and A. Richter, *Pair Decay Width of the Hoyle State and its Role for Stellar Carbon Production*. Phys. Rev. Lett., **105**, 022501 (2010), URL <http://link.aps.org/doi/10.1103/PhysRevLett.105.022501>. 14
- [Cli89] E. Clifford *et al.*, *The decay of ^{20}Na : Measurements of isospin mixing and the weak vector coupling constant as well as other new decay data*. Nuclear Physics A, **493**, 293 – 322 (1989), URL <http://www.sciencedirect.com/science/article/pii/0375947489903990>. 110, 111, 112, 113, 125, 128, 132, 133, 134, 136, 160

- [Coc32a] J. Cockcroft and E. Walton. Proc. Roy. Soc. London A, **136**, 619 (1932). 4, 33
- [Coc32b] J. Cockcroft and E. Walton. Proc. Roy. Soc. London A, **137**, 229 (1932). 4
- [Coc33] J. Cockcroft and E. Walton. Nature, **131**, 23 (1933). 33
- [Coh65] S. Cohen and D. Kurath, *Effective interactions for the 1p shell*. Nuclear Physics, **73**, 1 – 24 (1965), URL <http://www.sciencedirect.com/science/article/pii/0029558265901483>. 8
- [Coo57] C. W. Cook, W. A. Fowler, C. C. Lauritsen and T. Lauritsen, B¹². Phys. Rev., **107**, 508–515 (1957), URL <http://link.aps.org/doi/10.1103/PhysRev.107.508>. 14
- [Cos10] H. Costantini *et al.*, ¹⁶O. Phys. Rev. C, **82**, 035802 (2010), URL <http://link.aps.org/doi/10.1103/PhysRevC.82.035802>. 107, 108, 132, 134
- [Cyb10] R. H. Cyburt *et al.*, *The JINA REACLIB Database: Its Recent Updates and Impact on Type-I X-ray Bursts*. The Astrophysical Journal Supplement Series, **189**, 240 (2010), URL <http://stacks.iop.org/0067-0049/189/i=1/a=240>. 14
- [Dal53] R. H. Dalitz, *On the Analysis of τ -Meson Data and the Nature of the τ -Meson*. The Philosophical Magazine, **44**, 1068–1080 (1953). 26
- [Dav79] J. Davidson, H. Berg, M. Lowry, M. Dwarakanath, A. Sierk and P. Batay-Csorba, *Low energy cross sections for $^{11}\text{B}(p, 3\text{CE}\pm)$* . Nuclear Physics A, **315**, 253 – 268 (1979), URL <http://www.sciencedirect.com/science/article/pii/037594747990647X>. 34, 43, 163
- [Dee36] P. Dee and C. Gilbert. Proc. Roy. Soc. London A, **154**, 279–296 (1936). 33, 34, 156
- [Deh65] D. Dehnhard, *Direct Three-Body Decay*. Rev. Mod. Phys., **37**, 450–452 (1965), URL <http://link.aps.org/doi/10.1103/RevModPhys.37.450>. 35, 92
- [Des87] P. Descouvemont and D. Baye, *Microscopic theory of the $^8\text{Be}(\alpha, \gamma)^{12}\text{C}$ reaction in a three-cluster model*. Phys. Rev. C, **36**, 54–59 (1987), URL <http://link.aps.org/doi/10.1103/PhysRevC.36.54>. 8
- [Dig05] C. Diget *et al.*, *Properties of the ^{12}C 10 MeV state determined through α -decay*. Nuclear Physics A, **760**, 3 – 18 (2005), URL <http://www.sciencedirect.com/science/article/pii/S0375947405008602>. 17

- [Dig06] C. A. Diget, *Beta-delayed particle emission - probing the triple alpha continuum*. Ph.D. thesis, Aarhus University (2006). 119
- [Dun53] D. N. F. Dunbar, R. E. Pixley, W. A. Wenzel and W. Whaling, *The 7.68-Mev State in ^{12}C* . *Phys. Rev.*, **92**, 649–650 (1953), URL <http://link.aps.org/doi/10.1103/PhysRev.92.649>. 14
- [Fed96] D. Fedorov and A. Jensen, *The three-body continuum Coulomb problem and the $3\text{-}\alpha$ structure of ^{12}C* . *Physics Letters B*, **389**, 631 – 636 (1996), URL <http://www.sciencedirect.com/science/article/pii/S0370269396800013>. 8
- [Fif77] L. Fifield *et al.*, *Measurements of the radiative widths of the first $T = 1, 2+$ state of ^{20}Ne and their relationship to analog α -decays*. *Nuclear Physics A*, **288**, 57 – 81 (1977), URL <http://www.sciencedirect.com/science/article/pii/0375947477900811>. 135, 136
- [For76] H. Fortune, R. Betts and R. Middleton, *Mixing of $2+$ states in ^{20}Ne* . *Physics Letters B*, **62**, 287 – 288 (1976), URL <http://www.sciencedirect.com/science/article/pii/0370269376900769>. 134
- [Fre07] M. Freer, *The clustered nucleus α cluster structures in stable and unstable nuclei*. *Reports on Progress in Physics*, **70**, 2149 (2007), URL <http://stacks.iop.org/0034-4885/70/i=12/a=R03>. 105
- [Fre09] M. Freer *et al.*, 2^+ . *Phys. Rev. C*, **80**, 041303 (2009), URL <http://link.aps.org/doi/10.1103/PhysRevC.80.041303>. 16, 42
- [Fre12a] M. Freer, *Nuclear physics: Nucleons come together*. *Nature*, **487**, 309–310 (2012), URL <http://dx.doi.org/10.1038/487309a>. 15
- [Fre12b] M. Freer *et al.*, *Consistent analysis of the 2^+ excitation of the ^{12}C Hoyle state populated in proton and α -particle inelastic scattering*. *Phys. Rev. C*, **86**, 034320 (2012), URL <http://link.aps.org/doi/10.1103/PhysRevC.86.034320>. 16, 100
- [Fun03] Y. Funaki, A. Tohsaki, H. Horiuchi, P. Schuck and G. Röpke, *Analysis of previous microscopic calculations for the second 0^+ state in ^{12}C in terms of $3 - \alpha$ particle Bose-condensed state*. *Phys. Rev. C*, **67**, 051306 (2003), URL <http://link.aps.org/doi/10.1103/PhysRevC.67.051306>. 9
- [Fun06] Y. Funaki, Tohsaki, A., Horiuchi, H., Schuck, P. and Röpke, G., *Inelastic form factors to alpha-particle condensate states in ^{12}C and ^{16}O : What can we learn?* *Eur. Phys. J. A*, **28**, 259–263 (2006), URL <http://dx.doi.org/10.1140/epja/i2006-10061-5>. 8

- [Fyn02] H. O. U. Fynbo *et al.*, *Correlated emission of three α -particles in the β -decay of ^{12}N* . *Eur. Phys. J. A*, **15**, 135–138 (2002), URL <http://dx.doi.org/10.1140/epja/i2001-10241-9>. 17
- [Fyn03] H. O. U. Fynbo *et al.*, *Clarification of the Three-Body Decay of ^{12}C (12.71 MeV)*. *Phys. Rev. Lett.*, **91**, 082502 (2003), URL <http://link.aps.org/doi/10.1103/PhysRevLett.91.082502>. 20, 30, 95
- [Fyn05] H. O. U. Fynbo *et al.*, *Revised rates for the stellar triple- α process from measurement of ^{12}C nuclear resonances*. *Nature*, **433**, 136–139 (2005), URL <http://dx.doi.org/10.1038/nature03219>. 14, 17, 155
- [Fyn09] H. O. U. Fynbo, R. Álvarez-Rodríguez, R. Iguéz, A. S. Jensen, O. S. Kirsebom, D. V. Fedorov and E. Garrido, *Three-body decays and R-matrix analyses*. *Phys. Rev. C*, **79**, 054009 (2009), URL <http://link.aps.org/doi/10.1103/PhysRevC.79.054009>. 26
- [Fyn11] H. O. U. Fynbo and M. Freer, *Rotations of the Hoyle State in Carbon-12*. *Physics*, **4**, 94 (2011), URL <http://link.aps.org/doi/10.1103/Physics.4.94>. 15, 16
- [Gou71] G. Goulard, *Etat excité du ^{12}C á 16.11 MeV*. *Lettere al nuovo cimento*, **2**, 397–401 (1971). 35
- [Gra14] L. Grassi *et al.*, *Study of the inter-strip gap effects on the response of Double Sided Silicon Strip Detectors using proton micro-beams*. *Nuclear Instruments and Methods in Physics Research Section A: Accelerators, Spectrometers, Detectors and Associated Equipment*, **767**, 99 – 111 (2014), URL <http://www.sciencedirect.com/science/article/pii/S0168900214009292>. 71
- [Haf38] L. R. Hafstad and E. Teller, *The Alpha-Particle Model of the Nucleus*. *Phys. Rev.*, **54**, 681–692 (1938), URL <http://link.aps.org/doi/10.1103/PhysRev.54.681>. 5, 6, 155
- [Hag11] U. Hager *et al.*, *Direct total cross section measurement of the $^{16}\text{O}(\alpha, \gamma)^{20}\text{Ne}$ reaction at $E_{\text{c.m.}} = 2.26 \text{ MeV}$* . *Phys. Rev. C*, **84**, 022801 (2011), URL <http://link.aps.org/doi/10.1103/PhysRevC.84.022801>. 107
- [Har05] J. C. Hardy and I. S. Towner, *Superallowed $0^+ \rightarrow 0^+$ nuclear β decays: A critical survey with tests of the conserved vector current hypothesis and the standard model*. *Phys. Rev. C*, **71**, 055501 (2005), URL <http://link.aps.org/doi/10.1103/PhysRevC.71.055501>. 110

- [Hax49] O. Haxel, J. H. D. Jensen and H. E. Suess, *On Closed Shells in Nuclei. II.* Phys. Rev., **75**, 1766–1766 (1949), URL <http://link.aps.org/doi/10.1103/PhysRev.75.1766.2>. 5
- [HB87] H. T. H.W. Becker, C. Rolfs, *Low energy cross sections for $^{11}\text{B}(p, 3\text{CE}\pm)$.* Z. Phys. A - Atomic Nuclei, **327** (1987). 34, 35
- [Hin83] M. M. Hindi, J. Thomas, D. Radford and P. Parker. Phys. Rev. C, **27**, 2902 (1983). 105
- [Hoy53] F. Hoyle, D. N. F. Dunbar, W. A. Wenzel and W. Whaling, *1953 in Minutes of the New Mexico Meeting Held at Alberquerque, September 2, 3, 4 and 5.* Phys. Rev., **92** (1953). 13
- [Hoy54] F. Hoyle, *On Nuclear Reactions Occuring in Very Hot Stars. I. The Synthesis of Elements from Carbon to Nickel.* Astrophys. J. Suppl. Ser., **1** (1954). 13
- [Hud72] J. Hudomalj, B. Antolković, K. Schäfer and V. Valković, *Interference effects in the $^{11}\text{B}(p, 3\alpha)$ reaction at $E_p = 163$ keV.* Nuclear Physics A, **186**, 200 – 208 (1972), URL <http://www.sciencedirect.com/science/article/pii/0375947472901352>. 35, 93
- [Hyl10a] S. Hyldegaard, *Beta-decay studies of ^8Be and ^{12}C .* Ph.D. thesis, Aarhus University (2010). 115
- [Hyl10b] S. Hyldegaard *et al.*, R. Phys. Rev. C, **81**, 024303 (2010), URL <http://link.aps.org/doi/10.1103/PhysRevC.81.024303>. 17, 42
- [Ike68] K. Ikeda, N. Takigawa and H. Horiuchi, *The Systematic Structure-Change into the Molecule-like Structures in the Self-Conjugate $4n$ Nuclei.* Progress of Theoretical Physics Supplement, **E68**, 464–475 (1968), <http://ptps.oxfordjournals.org/content/E68/464.full.pdf+html>, URL <http://ptps.oxfordjournals.org/content/E68/464.abstract>. 6
- [Ing76] P. Ingalls, *The radiative width of the lowest $T = 1$ state of ^{20}Ne and fundamental α -decay studies.* Nuclear Physics A, **265**, 93 – 100 (1976), URL <http://www.sciencedirect.com/science/article/pii/0375947476901172>. 135, 136
- [Ito04] M. Itoh *et al.*, *Study of the cluster state at $E_x=10.3$ MeV in ^{12}C .* Nuclear Physics A, **738**, 268 – 272 (2004), proceedings of the 8th International Conference on Clustering Aspects of Nuclear Structure and Dynamics, URL <http://www.sciencedirect.com/science/article/pii/S0375947404005834>. 16

- [Ito11] M. Itoh *et al.*, *Candidate for the 2^+ excited Hoyle state at $E_x \sim 10$ MeV in ^{12}C* . Phys. Rev. C, **84**, 054308 (2011), URL <http://link.aps.org/doi/10.1103/PhysRevC.84.054308>. 16, 42
- [Ito14] M. Itoh *et al.*, *Further Improvement of the Upper Limit on the Direct 3α Decay from the Hoyle State in ^{12}C* . Phys. Rev. Lett., **113**, 102501 (2014), URL <http://link.aps.org/doi/10.1103/PhysRevLett.113.102501>. 20
- [Kam81] M. Kamimura. Nuclear Physics A, **351**, 456 – 480 (1981), URL <http://www.sciencedirect.com/science/article/pii/S0375947481901822>. 8
- [Kim04] M. Kimura, *Deformed-basis antisymmetrized molecular dynamics and its application to ^{20}Ne* . Phys. Rev. C, **69**, 044319 (2004), URL <http://link.aps.org/doi/10.1103/PhysRevC.69.044319>. 105, 113
- [Kir09] O. Kirsebom *et al.*, *Observation of γ -delayed 3α breakup of the 15.11 and 12.71 MeV states in ^{12}C* . Physics Letters B, **680**, 44 – 49 (2009), URL <http://www.sciencedirect.com/science/article/pii/S0370269309009836>. 17, 41
- [Kir10] O. S. Kirsebom *et al.*, *Breakup of ^{12}C resonances into three α particles*. Phys. Rev. C, **81**, 064313 (2010), URL <http://link.aps.org/doi/10.1103/PhysRevC.81.064313>. 26, 92
- [Kir11] O. S. Kirsebom *et al.*, *Precise and accurate determination of the ^8B decay spectrum*. Phys. Rev. C, **83**, 065802 (2011), URL <http://link.aps.org/doi/10.1103/PhysRevC.83.065802>. 111, 112, 121, 125, 134
- [Kir12] O. S. Kirsebom *et al.*, *Improved Limit on Direct α Decay of the Hoyle State*. Phys. Rev. Lett., **108**, 202501 (2012), URL <http://link.aps.org/doi/10.1103/PhysRevLett.108.202501>. 20
- [Kok13] T. Kokalova *et al.*, *Precision measurement of the 9.641 MeV, 3^- state in ^{12}C* . Phys. Rev. C, **87**, 057307 (2013), URL <http://link.aps.org/doi/10.1103/PhysRevC.87.057307>. 93
- [Kor90] A. Korshennikov. Yad. Fiz., **52**, 1304 (1990). 19
- [Kra88] K. S. Krane, *Introductory nuclear physics*. John Wiley & Sons, Inc. (1988). 123
- [Lab13] C. Labaune *et al.*, *Fusion reactions initiated by laser-accelerated particle beams in a laser-produced plasma*. Nat Commun, **4** (2013), URL <http://dx.doi.org/10.1038/ncomms3506>. 34

- [Lan58a] A. M. Lane and R. G. Thomas, *R-Matrix Theory of Nuclear Reactions*. Rev. Mod. Phys., **30**, 257–353 (1958), URL <http://link.aps.org/doi/10.1103/RevModPhys.30.257>. 29
- [Lan58b] A. M. Lane and R. G. Thomas, *R-Matrix Theory of Nuclear Reactions*. Rev. Mod. Phys., **30**, 257–353 (1958), URL <http://link.aps.org/doi/10.1103/RevModPhys.30.257>. 115, 140
- [Lau13] K. L. Laursen *et al.*, *High-statistics measurement of the β -delayed α spectrum of ^{20}Na* . Eur. Phys. J. A, **49**, 79 (2013), URL <http://dx.doi.org/10.1140/epja/i2013-13079-6>. 112
- [Len86] W. Lennard, H. Geissel, K. Winterbon, D. Phillips, T. Alexander and J. Forster, *Nonlinear response of Si detectors for low-Z ions*. Nuclear Instruments and Methods in Physics Research Section A: Accelerators, Spectrometers, Detectors and Associated Equipment, **248**, 454 – 460 (1986), URL <http://www.sciencedirect.com/science/article/pii/0168900286910338>. 57, 58, 157
- [Lin77] J. Lind, G. Garvey and R. Tribble, *Isospin mixing in ^{12}C* . Nuclear Physics A, **276**, 25–60 (1977), URL <http://www.sciencedirect.com/science/article/pii/0375947477901579>. 35
- [Mac80] J. D. MacArthur, H. C. Evans, J. R. Leslie and H. B. Mak, *First two members of the $K^\pi = 0^-$ band in ^{20}Ne* . Phys. Rev. C, **22**, 356–361 (1980), URL <http://link.aps.org/doi/10.1103/PhysRevC.22.356>. 106
- [May49] M. G. Mayer, *On Closed Shells in Nuclei. II*. Phys. Rev., **75**, 1969–1970 (1949), URL <http://link.aps.org/doi/10.1103/PhysRev.75.1969>. 5
- [McD60] L. C. McDermott, K. W. Jones, H. Smotrich and R. E. Benenson, *Elastic Scattering of Alpha Particles by O^{16}* . Phys. Rev., **118**, 175–181 (1960), URL <http://link.aps.org/doi/10.1103/PhysRev.118.175>. 113, 134
- [Mer92] A. Merchant and W. Rae, *Systematics of alpha-chain states in $4N$ -nuclei*. Nuclear Physics A, **549**, 431 – 438 (1992), URL <http://www.sciencedirect.com/science/article/pii/0375947492900893>. 9
- [mic] *MICRON semiconductor, Lancing, Sussex, UK.*, URL <http://www.micronsemiconductor.co.uk/>. 46
- [Mic87] F. Michel, G. Reidemeister and S. Ohkubo, *Last members of the $K^\pi = 0_4^+$ α -cluster rotational band in ^{20}Ne* . Phys. Rev. C, **35**, 1961–1963 (1987), URL <http://link.aps.org/doi/10.1103/PhysRevC.35.1961>. 105

- [ML14] D. J. Marín-Lámbbari *et al.*, *Evidence for Triangular D_{3h} Symmetry in ^{12}C* . *Phys. Rev. Lett.*, **113**, 012502 (2014), URL <http://link.aps.org/doi/10.1103/PhysRevLett.113.012502>. 100
- [Mor56] H. Morinaga, *Interpretation of Some of the Excited States of $4n$ Self-Conjugate Nuclei*. *Phys. Rev.*, **101**, 254–258 (1956), URL <http://link.aps.org/doi/10.1103/PhysRev.101.254>. 9, 15
- [Nav00] P. Navrátil, J. P. Vary and B. R. Barrett, *Properties of ^{12}C in the Ab Initio Nuclear Shell Model*. *Phys. Rev. Lett.*, **84**, 5728–5731 (2000), URL <http://link.aps.org/doi/10.1103/PhysRevLett.84.5728>. 8
- [Ö51] E. Öpik. *R. Ir. Acad.*, **54**, 49 (1951). 12
- [Og13] A. Ogloblin, T. Belyaeva, A. Danilov, A. Demyanova and S. Goncharov, *Radius of ^{12}C in the excited 2_2^+ Hoyle state*. *The European Physical Journal A*, **49**, 46 (2013), URL <http://dx.doi.org/10.1140/epja/i2013-13046-3>. 8
- [Oli33] M. Oliphant and L. Rutherford. *Proc. Roy. Soc. London A*, **141**, 259 (1933). 33
- [Opp38] J. R. Oppenheimer and R. Serber, *Note on Boron Plus Proton Reactions*. *Phys. Rev.*, **53**, 636–638 (1938), URL <http://link.aps.org/doi/10.1103/PhysRev.53.636>. 35
- [Que69] J. Quebert and L. Marquez. *Nuclear Physics A*, **126**, 646 – 670 (1969), URL <http://www.sciencedirect.com/science/article/pii/0375947469908549>. 35, 93
- [Ran13] T. K. Rana *et al.*, *Estimation of direct components of the decay of the Hoyle state*. *Phys. Rev. C*, **88**, 021601 (2013), URL <http://link.aps.org/doi/10.1103/PhysRevC.88.021601>. 20
- [Rey71] G. M. Reynolds, D. E. Rundquist and R. M. Pochar, *Study of C^{12} States Using the $\text{B}^{11}(\text{He}^3, d)\text{C}^{12}$ Reaction*. *Phys. Rev. C*, **3**, 442–447 (1971), URL <http://link.aps.org/doi/10.1103/PhysRevC.3.442>. 16
- [Ric84] H. T. Richards, *Rotational bands in ^{20}Ne* . *Phys. Rev. C*, **29**, 276–283 (1984), URL <http://link.aps.org/doi/10.1103/PhysRevC.29.276>. 105
- [Ros03] N. Rostoker, A. Qerushi and M. Binderbauer, *Colliding Beam Fusion Reactors*. *Journal of Fusion Energy*, **22**, 83–92 (2003), URL <http://dx.doi.org/10.1023/B3AJOFE.0000036407.10861.bc>. 34

- [Rut11] E. Rutherford, *The scattering of α and β particles by matter and the structure of the atom*. Philosophical Magazine, **21**, 669 (1911). 3
- [Sch93] D. Schardt and K. Riisager, *Beta-neutrino recoil broadening in β -delayed proton emission ^{32}Ar and ^{33}Ar* . Zeitschrift für Physik A Hadrons and Nuclei, **345**, 265–271 (1993), 10.1007/BF01280833, URL <http://dx.doi.org/10.1007/BF01280833>. 123
- [Seg61] R. E. Segel and M. J. Bina, *Partial Widths of the 16.11-Mev State in C^{12}* . Phys. Rev., **124**, 814–817 (1961), URL <http://link.aps.org/doi/10.1103/PhysRev.124.814>. 43, 163
- [Sie87] P. J. Siemens and A. S. Jensen, *Elements of Nuclei*. Allan Wylde (1987). 37
- [Sim] URL <https://sites.google.com/site/ausalib/tools/simx/documentation>. 78, 80
- [Smi12] F. D. Smit *et al.*, *No evidence of an 11.16 MeV 2^+ state in ^{12}C* . Phys. Rev. C, **86**, 037301 (2012), URL <http://link.aps.org/doi/10.1103/PhysRevC.86.037301>. 16
- [Spr12] M. Spraker *et al.* Journal of Fusion Energy, **31**, 357–367 (2012), URL <http://dx.doi.org/10.1007/s10894-011-9473-5>. 34
- [Sta11] S. Stave *et al.*, *Understanding the reaction at the 0.675 MeV resonance*. Physics Letters B, **696**, 26 – 29 (2011), URL <http://www.sciencedirect.com/science/article/pii/S0370269310013626>. 34
- [Ste78] D. J. Steck, *Isospin forbidden and allowed reactions $^{16}\text{O}(\alpha, \alpha_0)^{16}\text{O}$ and $^{16}\text{O}(\alpha, \gamma)^{20}\text{Ne}$* . Phys. Rev. C, **17**, 1034–1050 (1978), URL <http://link.aps.org/doi/10.1103/PhysRevC.17.1034>. 135
- [Tea10] R. M. L. Team, [<http://seal.web.cern.ch/seal/MathLibs/Minuit2/html/index.html>] (2010), URL <http://seal.web.cern.ch/seal/MathLibs/Minuit2/html/index.html>. 128
- [Ten04] O. Tengblad, U. Bergmann, L. Fraile, H. Fynbo and S. Walsh, *Novel thin window design for a large-area silicon strip detector*. Nuclear Instruments and Methods in Physics Research Section A: Accelerators, Spectrometers, Detectors and Associated Equipment, **525**, 458 – 464 (2004), URL <http://www.sciencedirect.com/science/article/pii/S0168900204002414>. 46, 71

- [The98] L.-S. The, D. D. Clayton, L. Jin and B. S. Meyer, *Nuclear Reactions Governing the Nucleosynthesis of ^{44}Ti* . *The Astrophysical Journal*, **504**, 500 (1998), URL <http://stacks.iop.org/0004-637X/504/i=1/a=500>. 15
- [Til98] D. Tilley, C. Cheves, J. Kelley, S. Raman and H. Weller, *Energy levels of light nuclei, $A = 20$* . *Nuclear Physics A*, **636**, 249 – 364 (1998), URL <http://www.sciencedirect.com/science/article/pii/S0375947498001298>. 113, 121, 125, 132, 135
- [Tre72] P. Treado, J. Lambert, V. Alessi and R. Kane, *Angular correlation and reaction mechanism for*. *Nuclear Physics A*, **198**, 21–32 (1972), URL <http://www.sciencedirect.com/science/article/pii/0375947472907695>. 35
- [Tur10] C. Tur, A. Heger and S. M. Austin, *Production of ^{26}Al , ^{44}Ti , and ^{60}Fe in Core-collapse Supernovae: Sensitivity to the Rates of the Triple Alpha and $^{12}\text{C}(\alpha, \alpha)^{16}\text{O}$ Reactions*. *The Astrophysical Journal*, **718**, 357 (2010), URL <http://stacks.iop.org/0004-637X/718/i=1/a=357>. 15
- [Vog12] (2012), URL <http://www.jinaweb.org/events/matrix/05-R-matrix.pdf>. 139
- [Wei35] C. Weizsäcker, *Zur Theorie der Kernmassen*. *Zeitschrift für Physik*, **96**, 431–458 (1935), URL <http://dx.doi.org/10.1007/BF01337700>. 5
- [Yao06] W.-M. Yao, *Review of Particle Physics*. *Journal of Physics G: Nuclear and Particle Physics*, **33**, 1 (2006), URL <http://stacks.iop.org/0954-3899/33/i=1/a=001>. 110
- [Zem64] C. Zemach, *Three-Pion Decays of Unstable Particles*. *Phys. Rev.*, **133**, B1201–B1220 (1964), URL <http://link.aps.org/doi/10.1103/PhysRev.133.B1201>. 26
- [Zie08] J. F. Ziegler, J. P. Biersack and M. D. Ziegler, *SRIM - The Stopping and Range of Ions in Matter*. SRIM Co., United States of America (2008). 56, 128
- [Zim11] W. R. Zimmerman, N. E. Destefano, M. Freer, M. Gai and F. D. Smit, *Further evidence for the broad 2_2^+ state at 9.6 MeV in ^{12}C* . *Phys. Rev. C*, **84**, 027304 (2011), URL <http://link.aps.org/doi/10.1103/PhysRevC.84.027304>. 16
- [Zim13a] W. R. Zimmerman, *Direct Observation of the Second 2^+ State in ^{12}C* . Ph.D. thesis, University of Connecticut (2013). 17

- [Zim13b] W. R. Zimmerman *et al.*, *Unambiguous Identification of the Second 2^+ State in ^{12}C and the Structure of the Hoyle State*. *Phys. Rev. Lett.*, **110**, 152502 (2013), URL <http://link.aps.org/doi/10.1103/PhysRevLett.110.152502>. 17, 40, 100

List of Figures

1.1	Binding energy plotted against the number of α - α bonds in light even-even nuclei. The number of bonds is counted as done by Hafstad and Teller [Haf38].	5
1.2	Geometric arrangement of light even-even nuclei predicted by D. M. Brink [Bri67]. The number of possible α - α bonds as predicted in [Haf38] is reflected in the arrangements.	6
1.3	Simple shell model picture of ^{12}C . An example is shown where a neutron is excited from the $1p_{3/2}$ orbital to the $1d_{5/2}$ orbital, resulting in a state with spin and parity of 1^- , 2^- , 3^- or 4^-	8
1.4	Level scheme of ^{12}C including known states up to 16 MeV.	9
1.5	Figures showing the Maxwell-Boltzmann factor ($e^{-E/k_B T}$) and the Gamow factor ($e^{-2\pi\eta}$) for a temperature of 0.2 GK in case of the $^4\text{He} + ^4\text{He}$ reaction (a) and the $^4\text{He} + ^8\text{Be}$ reaction (b) . Both these factors enter the integrand in Eq. 1.8 and their product, the red solid line, determines the energies at which thermonuclear processes occur. The arrow in (a) indicates the position of the ^8Be ground state while in (b) it indicates the position of the Hoyle state. The ordinate is in arbitrary units.	13
1.6	$3\text{-}\alpha$ reaction rate from [Fyn05] relative to the NACRE rate (logarithmic ratio on the ordinate). The Fynbo result is also shown when only including the Hoyle state in the rate calculations.	14
2.1	Schematic diagram of the ^{12}C decay scheme.	20
2.2	The $3\text{-}\alpha$ break-up. θ' is the angle between the secondary α -particle and the first emitted α -particle as seen from the ^8Be frame. $\theta_{2,3}$ is the angle between the secondary emitted α -particles seen from the ^{12}C frame.	22
2.3	Plots showing the variation in secondary α -particle energy (a) and break-up angle between the secondary α -particles (b) as function of break-up angle in the ^8Be system. The initial ^{12}C energy is 16.1058 MeV and $\theta_{\alpha,^8\text{Be}}$ is chosen to 0°	23
2.4	Plots showing the dependence both on θ' and $\theta_{\alpha,^8\text{Be}}$ for the break-up angle between the secondary α -particles (panels a and b) and the energy for one of the secondary α -particles (panels c and d). Both quantities are measured in the laboratory reference frame. Panels a and c refer to break-up's proceeding through $^8\text{Be}(\text{gs})$ while Panels b and d refer to the excited state channel.	24

2.5	Definition of the Dalitz plot. The triangle defines the phase space region allowed by energy conservation while the circle illustrates the region allowed by momentum conservation for a fully non-relativistic case.	26
2.6	Dalitz plots for the break-up of the 16.11 MeV state. Clear structures appear as a consequence of the sequential decay through the ^8Be ground state (b) and first excited state (a) . The plots are constructed only by considering the kinematics in the break-up and assuming a symmetric level profile for the first excited state with $\Gamma = 1.5$ MeV. The color scale, most easily seen in (a) , shows how the break-up angle θ' depends on the position in the Dalitz plot.	27
2.7	Geometrical visualization of the projected coordinates ρ , ξ and η in the Dalitz plot.	28
3.1	Spectrum from [Dee36]. 79 values for the $3\text{-}\alpha$ sum energy measured from the $p + ^{11}\text{B}$ reaction. The sum energy was obtained from a pair of α -particle energies, deducing the third energy from conservation of momentum.	34
3.2	Spectrum from [Dee36] showing the measured α -particle energy spectrum from the $p + ^{11}\text{B}$ reaction. The dashed line represents a calculation of the expected distribution assuming break-up via $^8\text{Be}(1.\text{exc.})$	34
3.3	Scheme picturing $p + ^{11}\text{B}$ populating the 16.11 MeV state and the subsequent γ -delayed $3\text{-}\alpha$ break up.	40
4.1	Coarse overview of the beamline showing the accelerator tank and the detection chamber.	46
4.2	Photograph of the detection chamber.	47
4.3	Photograph of the two DSSSDs that were used.	47
4.4	Scheme showing the electronics of the acquisition setup.	48
4.5	Top parts in both a and b show the raw energy spectrum. Raw refers to the fact that no cuts have been applied to the data and the energy is the deposited energy in the detectors. The red colored parts show signals that mostly are due to noise. The bottom parts display the trigger efficiency.	50
4.6	Decay sequence for ^{228}Th . Shown in keV are the energies that are used in the calibration procedure.	51
4.7	Definition of the laboratory coordinate axes (\hat{x} , \hat{y} and \hat{z}) and the local detector axes (\hat{x}' and \hat{y}').	52
4.8	The detection setup viewed from above with definition of the angles θ_D and θ_V	52

4.9	Energy scan of the 16.11 MeV resonance. The number of α_0 -particles and 3- α break-ups divided by the collected beam charge are shown.	55
4.10	Hitpattern in detector 1 when measuring on the α -source. The contour plot is the result of a fit to the solid angles across the pixels on the detector.	56
4.11	Center-of-mass curves showing the α_0 -energies when measuring on the $^{11}\text{B}(p,3\alpha)$ reaction.	56
4.12	The range of α -particles in silicon. The stars are the values from SRIM and the line represents the spline made to them. The arrows are for guidance in the explanation of the energy loss calculation procedure (see the text).	57
4.13	Non-ionizing energy loss of α -particles in silicon. The stars show the values from [Len86] while the line shows the parametrization used for calculating non-ionizing energy losses at arbitrary energies.	57
4.14	Illustration of the source and detector. The left side is drawn to scale. On the right side the source and the front of the detector are zoom in on. The yellow layer illustrates the layer on top of the source and the brown layer represent the non-active layer on the detector front side. The calibration procedure takes into account energy losses of the α particles in these layers.	59
4.15	^{228}Th calibration spectrum in a detector strip. The arrows point at the peaks used for calibration and the inset is a close up look at one of the peaks.	60
4.16	Final linear fit from which the calibration coefficients are obtained. These relate ionizing energy with ADC channel.	60
4.17	Visualization of the angles involved in the source thickness calculation	61
4.18	Looking in the $-\hat{y}$ direction.	61
4.19	Measured differences in positions for the calibration peak of lowest energy. The results for strips 1-8 are with $\theta_s = -60^\circ$ while for strips 9-15 $\theta_s = +60^\circ$. The red curve displays the second factor in 4.6 (called the <i>angle factor</i>) which gives the expected variation in the path length difference across the detector.	62
4.20	Measured source thicknesses determined by use of front strip 8 and 9. Top part is for $\theta_s = -60^\circ$ while the bottom part is for $\theta_s = +60^\circ$	62
4.21	Deviation from expected 3 α sum energy versus run number. The vertical lines indicate positions where discontinuities in the sum energy trend are apparent. The numbers in each division gives the run series number in accordance with the definition in Section 4.3.	63

4.22	The number of $3\text{-}\alpha$ events per beam charge measured from the $(2^+, 1)$ resonance.	64
5.1	Summed TDC spectra for front side strips for a single data file with the number of counts on the ordinate. The dotted lines indicate the acceptance region. (a) Detector 1. (b) Detector 2.	68
5.2	Summed ADC spectra for front side strips on detector 1 for a single data file with the number of counts on the ordinate. In (a) the spectrum is plotted without applying TDC cuts, while in (b) the TDC cuts are applied.	69
5.3	Back and front strip energies for detector 1 using the ^{228}Th source.	71
5.4	Difference between front and back energies in detector 1 using $p + ^{11}\text{B}$ data. The red lines indicate the applied tolerance level.	71
5.5	Plots showing the front-back matched energy spectrum measured in detector 2. The total spectrum is divided into three spectra depending on the front-back matching method: events lying on the front vs. back diagonal, sharing events and summing events. (a) Front side sharing and summing. (b) Back side sharing and summing.	72
5.6	In blue: distributions for the total momentum (a) and the x -component of the total momentum (b) for all detections that survive the TDC cut. Red hatched histograms: additional requirements on the sum-angle and $\theta_{1,23}$	74
5.7	In blue: distributions for $\theta_{1,2} + \theta_{2,3} + \theta_{3,1}$ (a) and $\theta_{1,23}$ (b) for all detections that survive the TDC cut. Red hatched histograms: additional requirements on the total momentum and its components.	75
5.8	Total momentum plotted against the reconstructed excitation energy (panel B). Panel A shows the projection onto the energy axis when momentum and angle cuts are applied, while Panel C is the projection without these cuts. (a) No TDC cuts applied. (b) : TDC cuts applied. The plots are based on a small subset of the acquired data.	76
5.9	Relative energies (^8Be energies) for the three combinations of α -particle pairs. The spectra for multiplicity-two (red dashed line) and three (blue dotted line) data together with the cut-levels applied to identify the decay channel are shown.	78
6.1	α -particle energy spectrum measured in detector 1 for data set number 9. The filled spectrum is the total coincidence spectrum. The red spectrum is obtained by requiring exactly one detection in each detector, while the black spectrum has been obtained when requiring at least three detections.	82

- 6.2 Reconstructed excitation energy spectrum for multiplicity-three events for data set number 9. All cuts have been applied in this plot. The dotted red line illustrates the known excitation energy of the 2^+ resonance. 82
- 6.3 Dalitz plot distribution for data set 9. In **(a)** the distribution is plotted for multiplicity-two events and in **(b)** it is plotted for multiplicity-three events. 84
- 6.4 Dalitz plot distributions for a pure phase space simulation of the $3\text{-}\alpha$ break-up. The unmodified distribution, i.e. without taking experimental effects into account, is shown in **(b)**. In **(a)** the phase space distribution resulting from a multiplicity-two analysis is shown, while **(c)** shows the corresponding distribution resulting from a multiplicity-three analysis. The non-vanishing regions in **(a)** and **(c)** marks the regions of the $3\text{-}\alpha$ phase space that the detection setup provides sensitivity in. 85
- 6.5 Coincidence single α -particle energy spectrum measured in detector 2 (grey filled histogram). Simulated spectra: model 1 (blue solid line), model 2 (green solid line), model 3 (red solid line) and model 5 (red dashed line). The ${}^8\text{Be}(\text{gs})$ channel is represented by the long dashed black line and is added to the ${}^8\text{Be}(\text{exc})$ spectra. 87
- 6.6 Coincidence single α -particle energy spectrum measured in detector 2 (grey filled histogram). Simulated spectra: model 4 (black dotted-dashed line), model 5 (red dashed line) and model 6 (blue dotted line). The ${}^8\text{Be}(\text{gs})$ channel is represented by the long dashed black line and is added to the ${}^8\text{Be}(\text{exc})$ spectra. 87
- 6.7 Triple coincidence single α -particle energy spectrum measured in detector 2 (grey filled histogram). Simulated spectra: model 1 (blue solid line), model 2 (green solid line), model 3 (red solid line) and model 5 (red dashed line). The ${}^8\text{Be}(\text{gs})$ channel is represented by the long dashed black line and is added to the ${}^8\text{Be}(\text{exc})$ spectra. 88
- 6.8 Triple coincidence single α -particle energy spectrum measured in detector 2 (grey filled histogram). Simulated spectra: model 4 (black dotted-dashed line), model 5 (red dashed line) and model 6 (blue dotted line). The ${}^8\text{Be}(\text{gs})$ channel is represented by the long dashed black line and is added to the ${}^8\text{Be}(\text{exc})$ spectra. 88
- 6.9 Simulated Dalitz plot distributions for the ${}^8\text{Be}(\text{exc})$ channel. The simulations are based on model 1 **(a)**, model 2 **(b)**, model 4 **(c)** and model 5 **(d)**. 89

- 6.10 Dalitz plot projections as defined in Section 2.1.3. The projected coordinates are 3ρ (a), $2\sqrt{3}\xi$ (b) and $2\sqrt{3}\eta$ (c). The grey filled histograms are the measured distributions. The simulated data is based on model 2 (green solid line), model 3 (black solid line), model 4 (blue solid line) and model 5 (red dotted line). 90
- 6.11 Lower plot: excitation energy spectrum for all coincidence three data. The blue hatched histogram represents $3\text{-}\alpha$ decays proceeding through the ground state in ${}^8\text{Be}$, while the red histogram represents those going via the first excited state in ${}^8\text{Be}$. Top plot: for each $3\text{-}\alpha$ decay event the energies of all three α -particles are plotted. The diagonal structure represents ${}^8\text{Be}$ ground state decays. 94
- 6.12 Ordinate: Laboratory energy of an α -particle emitted from ${}^8\text{Be}$ after decay of the 3^- , 1^- and 1^+ levels. Abscissa: Relative ${}^8\text{Be}$ break-up angle relative to the first emitted α -particle. 96
- 6.13 Bottom part shows simulated deposited energies of the three α -particles emitted from the 3^- level. Energy losses are taken into account. The two top plots show the trigger efficiency (summed over all strips) variation as a function of deposited energy in the detectors. 96
- 7.1 Comparison of the experimental energy spectrum in the two lowest rotational bands in ${}^{20}\text{Ne}$ with predictions from the simple $\alpha + {}^{16}\text{O}$ core model in [Buc95]. The band heads are the ground 0^+ state and the excited 1^- state. Illustration from [Buc95]. 106
- 7.2 Level scheme for ${}^{20}\text{Ne}$ showing states relevant for a astrophysical discussion (near the $\alpha + {}^{16}\text{O}$ threshold) and above threshold states from which β -delayed α -particles are measured in the present work. 107
- 7.3 Figure showing the Maxwell-Boltzmann factor ($e^{-E/k_B T}$) and the Gamow factor ($e^{-2\pi\eta}$) for a temperature of 0.2 GK in case of the ${}^4\text{He} + {}^{16}\text{O}$ reaction. Both these factors enter the integrand in Eq. 1.8 (Section 1.4) and their product, the red solid line, determines the energies at which thermonuclear processes occur. The arrows indicate the positions of the ${}^{20}\text{Ne}$ resonances closest to the Gamow window. The ordinate is in arbitrary units. 108
- 7.4 Section of the nuclear chart. Arrow pointing from upper left indicates β^+ -decay while the other signifies the possible α -emission. 109
- 7.5 Detector setup in the Jyvaskylä experiment. 112
- 7.6 Events recorded in DSSSD 1 in the 2nd run. Numbering reflects the interpretation of [Cli89]. Asterisks indicate the position of satellite peaks. 113

9.1	Simulation of the recoil distribution associated with Fermi (red curve) and Gamow-Teller (blue curve) β -decay. The example describes the broadening of α -particles with $E = 2.50$ MeV decaying from an excitation energy of $E^* = 7.86$ MeV.	124
9.2	Example illustrating the implementation of recoil and response corrections. First the R -matrix expression is calculated, whereafter it is recoil (green curve) and response corrected (blue curve).	124
9.3	Response function fit with and without the Gamow-Teller background.	127
9.4	Final response function fit showing main and satellite contribution.	127
9.5	Best R -matrix fit. Black: data. Blue: fit. Red: R -matrix expression without broadening effects.	128
9.6	Fit residual showing the deviations between the fit and the measured data relative to the statistical error.	129
10.1	R -matrix fit including only levels 2 and 5.	133

List of Tables

3.1	Weisskopf estimates for $\Gamma_W(E/ML)$. The γ energies E_λ are in units of MeV. A is the nucleon number for the decaying nucleus.	39
3.2	Possible spin and parities for states to be reached by E1, M1, E2 and M2 transitions from a 2^+ state. Also shown is the Weisskopf estimates Γ_W for decays to excitation energies of 10 and 13 MeV.	42
3.3	Here, the branching ratios are given for the four γ -branches observed in the most recent study of γ -decays from the 16.11 MeV level. The third column gives the radiative widths as they appear in [Ade77] where a value of 6.7 keV [Seg61] was used for the total width. In the fourth column revised widths are given as the updated value $\Gamma = 5.3$ keV is used [Dav79].	43
4.1	Overview of the run groups that the data are divided into.	54
6.1	Definition of the models that are compared to data. See the text for definitions of the listed quantities.	86
6.2	Branching ratios for the $^8\text{Be}(\text{gs})$ break-up channel as measured on basis of multiplicity-two and three data. Efficiencies for detecting $^8\text{Be}(\text{gs})$ and $^8\text{Be}(\text{exc})$ break-up's are listed for both multiplicities. For the branching ratios the first parenthesis gives the statistical error while the second parenthesis gives the systematic error. The error on the efficiencies are the total error.	91
6.3	The five different groups that simulation are carried out for. Group 4 is divided into 6 intervals, 250 keV wide each. The simulations in groups 4 and 5 are divided into two sub-groups assuming M1 and E1 decays to 2^+ and 3^- states, respectively. Individual simulations are performed for all the 10 data sets.	95
6.4	Results obtained for each data set on the γ -decays to the 1^+ (12.71 MeV) and 1^- (10.85 MeV) levels. The second column in each table gives the number of observed γ -decays. The third column gives the obtained detection efficiency. The final column presents the γ -width in units of eV.	98
6.5	Results obtained for each data set on the γ -decays to the 3^- (9.64 MeV) level. The second column gives the number of observed γ -decays. The third column gives the obtained detection efficiency. The final column presents the γ -width in units of eV.	99

6.6	Average values for the measured γ -widths to the 1^+ , 1^- and 3^- levels. The corresponding literature values are the adjusted values from from [Ade77] as listed in [AS90]. Reduced matrix elements are calculated assuming the lowest possible multipolarity possible.	99
6.7	Results obtained averaging over all data sets on the γ -decay to the natural parity distribution at 10.0 MeV and at 15.5-13.0 MeV. The second column gives the number of observed γ -decays. Columns 3 and 5 give the γ -widths for the 2^+ and 3^- cases, respectively, while columns 4 and 6 present the corresponding reduced matrix elements.	100
10.1	Results extracted from R-matrix fit.	132
10.2	Properties for the IAS in ^{20}Ne obtained from results in the this work in combination with results from earlier studies. The bottom part of the table lists the relative quantities used for the calculations.	136